Doctoral Dissertation

Identification of Small Molecules with Reactivities against Multiple Pathogenic Elements of Alzheimer's Disease

Geewoo Nam

Department of Chemistry

Graduate School of UNIST

2020

Identification of Small Molecules with Reactivities against Multiple Pathogenic Elements of Alzheimer's Disease

Geewoo Nam

Department of Chemistry

Graduate School of UNIST

Identification of Small Molecules with Reactivities against Multiple Pathogenic Elements of Alzheimer's Disease

A dissertation submitted to the Graduate School of UNIST
in partial fulfillment of the requirements
for the degree of Doctor of Philosophy of Science

Geewoo Nam

June 15, 2020

Approved by

_____

Advisor

Associate Professor Tae-Hyuk Kwon

III

Identification of Small Molecules with Reactivities against Multiple Pathogenic Elements of Alzheimer's Disease

Geewoo Nam

This certifies that the dissertation of Geewoo Nam is approved.

June 15, 2020

_____

Advisor: Associate Professor Tae-Hyuk Kwon

_____

Professor Mi Hee Lim

_____

Associate Professor Oh-Hoon Kwon

_____

Assistant Professor Jung-Min Kee

_____

Assistant Professor Hyuck Jin Lee

Abstract

Alzheimer's disease (AD) remains a formidable threat against mankind since its introduction in 1906. As a progressive neurodegenerative disease responsible for the majority of dementia cases, AD remains cureless. Along with the lack of an effective cure, the aging world population depicts an imminent epidemic and pessimistic outlook regarding the disease. Research endeavors dedicated to understanding the etiopathology of AD and developing therapeutics have led to significant progress in our comprehension of AD. However, attempts of formulating treatments with the ability to stop AD progression have proven futile. More specifically, various pathological factors have been identified and implicated as sources of neurodegeneration leading to AD. These include amyloid-β (Aβ), metal ions, acetylcholinesterase (AChE), and reactive oxygen species (ROS) indicated in the various hypotheses attempting to elucidate the main cause of AD: amyloid cascade, metal ion, cholinergic, and oxidative stress, respectively. Therapeutic approaches targeting these individual pathogenic features have yet to result in clinically effective treatment strategies. Such failures have led to a shift in paradigm to understand the interconnections between these pathological factors to account for AD's complexity. Intricacies of the pathogenic elements of AD present experimental challenges in investigating their inter-relationships. Multifunctional molecules capable of targeting multiple pathogenic factors of AD could, therefore, be beneficial in our attempt to understand AD. In this thesis, we first aim to identify molecular frameworks conferring multifunctionality against multiple pathogenic factors of AD [*i.e.*, Aβ, metal-bound Aβ (metal–Aβ), AChE, and ROS] from the structures of both natural products and synthetic molecules. Such chemical entities will be helpful in furthering our understanding of the relationships among the different pathological factors and assist the development of physiologically viable chemical tools with suitable bioapplicability. We hope that these findings contribute towards an improved capacity for experimentally examining the complex network of AD pathology and a closer understanding of its inner workings.

In Chapter 1, we briefly introduce the multifaceted pathology of AD and discuss the various pathogenic elements implicated in driving the development and progression of the disease. In Chapter 2, a naturally occurring isoflavone, **orobol**, is presented as a multifunctional molecule with modulative reactivity against four specific pathical factors of AD: metal-free Aβ, metal–Aβ, ROS, and AChE. In chapter 3, the molecular structures of 12 flavonoids, selected based on three multifunctional flavonoids (*i.e.*, **quercetin**, **luteolin**, and **orobol**) were examined with respect to their reactivities against metal-free Aβ, metal–Aβ, ROS, and AChE. This study aimed to identify the molecular features responsible for instilling these flavonoids with the ability to modulate the aforementioned targets. Four major structural attributes were identified to contribute to such versatility of select flavonoids. In chapter 4, pre-approved anti-depressant molecules were explored as candidates of drug repurposing to discover

new multifunctional molecules against AD and increase our database of structural moieties associated with multifunctionality. The versatile reactivity of three synthetic compounds were demonstrated against Cu(II)–Aβ, free radicals, and AChE.

Overall, we present a number of multifunctional chemicals capable of targeting several major pathogenic elements of AD. We believe that these molecules will contribute significantly towards our efforts to better comprehend the multifaceted etiopathology of AD by serving as chemical tools that allow us to directly perform experiments regarding the pathogenic connections between metal-free Aβ, metal–Aβ, ROS, and AChE at *in vitro* and possibly clinical stages. Moreover, identification of the structural features instilling multifunctionality could facilitate the design and development of biocompatible therapeutics capable of simultaneously targeting multiple pathologies of AD and their connections. Our approaches will provide the foundation for developing effective and efficient methods of elucidating fundamental connections among the pathological factors of AD at the molecular level and identifying efficacious therapeutics against AD capable of controlling the progression of neurodegeneration.

Table of Contents

Chapter 1. Multifaceted Pathology of Alzheimer's disease

Chapter 2. Orobol: An Isoflavone Exhibiting Regulatory Multifunctionality against Four Pathological Features of Alzheimer's Disease

Chapter 3. Multiple Reactivities of Flavonoids towards Pathological Elements in Alzheimer's Disease: Structure-Activity Relationship

Chapter 4. Drug Repurposing: Multifunctional Molecules against Cu(II)–Amyloid-β, Reactive Oxygen Species, and Acetylcholinesterase

List of Figures

Figure 1.1. The production, aggregation, and amino acid sequence of Aβ. (a) Non-amyloidogenic and amyloidogenic processing of the amyloid precursor protein (APP). (b) Aggregation pathways of Aβ. (c) Amino acid sequence of $A\beta_{40}$ and $A\beta_{42}$; (blue) self-recognition site of Aβ; (red) two additional hydrophobic amino acid residues at the *C*-terminus for $A\beta_{42}$.

Figure 1.2. Six isoforms of tau and their structural characterizations based on amino acid domains. N1 and N2: *N*-terminal projection domains; R1, R2, R3, and R4: Microtubule binding repeat domains.

Figure 1.3. Feasibility of the presence of Aβ and metal ions [*e.g.*, Cu(II) and Zn(II)] at the synaptic cleft upon neurotransmission.

Figure 1.4. Proposed metal coordination to Aβ. Binding modes of (a) Cu(II)–Aβ (component I and II) and (b) Zn(II)–Aβ.

Figure 1.5. Schematic representation of the multifaceted pathology of neurodegenerative diseases. (a) Proteopathy of wild-type (wt) or mutant intra- or extracellular unfolded proteins/peptides. Unfolded monomers partially fold and aggregate into oligomers and fibrils. Oligomers may interact with various organelles (*e.g.*, mitochondria) or cell membrane disrupting Ca(II) homeostasis and signaling. (b) Dyshomeostasis of metal ions that, depending on the disease, can bind to misfolded proteins/peptides affecting their aggregation or accumulate in the brain or spinal cord. (c) Elevated oxidative stress resulting from redox-active metal ions (*i.e.*, Cu and Fe) *via* Fenton-like reactions or ROS escaping from damaged mitochondria. ROS can attack cellular proteins, nucleic acids, and lipids causing oxidative damage. (d) Mitochondrial dysfunction and defects in energy metabolism that can occur as a consequence of protein/peptide aggregates. (e) Aberrant axonal transport from hyperphosphorylated microtubule binding proteins, mutant tubulin proteins, or mutant motor proteins. (f) Pervasive, sustained chronic inflammation with reactive microglia and astrocytes as well as altered inflammatory signaling pathways.

Figure 2.1. Rational identification of **orobol** as a multifunctional small molecule for regulating four pathological factors implicated in AD (*i.e.*, metal-free Aβ, metal–Aβ, free radicals, and AChE).

Figure 2.2. Influence of **orobol** on the formation of metal-free and metal-induced $A\beta_{42}$ aggregates. (a) Scheme of the inhibition experiment. (b) Analysis of the MW distribution of the resultant $A\beta_{42}$ species by gel/Western blot using an anti-Aβ antibody (6E10). (c) TEM images of the samples from (b). Conditions: $[A\beta_{42}] = 25$ μM; $[CuCl_2$ or $ZnCl_2] = 25$ μM; $[\textbf{orobol}] = 50$ μM; 20 mM HEPES, pH 7.4 [for metal-free and Zn(II)-containing samples] or pH 6.6 [for Cu(II)-added samples], 150 mM NaCl; 37 °C; 24 h incubation; constant agitation.

Figure 2.3. Influence of **orobol** on the disassembly and/or aggregation of preformed metal-free and metal-associated $A\beta_{42}$ aggregates. (a) Scheme of the disaggregation experiment. (b) Analysis of the molecular weight distribution of the resultant $A\beta_{42}$ species by gel/Western blot with an anti- Aβ antibody (6E10). (c) TEM images of the samples from (b). Conditions: $[A\beta_{42}] = 25$ μM; $[CuCl_2$ or $ZnCl_2] = 25$ μM; $[\textbf{orobol}] = 50$ μM; 20 mM HEPES, pH 7.4 [for metal-free and Zn(II)-containing samples] or pH

6.6 [for Cu(II)-added samples], 150 mM NaCl; 37 °C; 24 h incubation; constant agitation.

Figure 2.4. Interactions of **Oro** with metal-free Aβ$_{42}$. (a) Interaction of **Oro** with soluble metal-free Aβ$_{42}$, monitored by ESI-MS. Inset: Zoom-in spectrum from 1860 to 1880 *m/z* (indication of [2Aβ$_{42}$ + **Oro**]$^{5+}$ at 1863 *m/z*). (b) Analysis of the IM-MS spectra of [2Aβ$_{42}$]$^{5+}$ (black) and [2Aβ$_{42}$ + **Oro**]$^{5+}$ (purple). Conditions: [Aβ$_{42}$] = 20 μM; [**Oro**] = 100 μM; 100 mM ammonium acetate, pH 7.4; 3 h incubation; no agitation.

Figure 2.5. Interactions of **Oro** with Cu(II) and Cu(II)−Aβ$_{42}$. (a) Cu(II) binding of **Oro** in a buffered solution. UV−Vis spectra of **Oro** (black) with up to 5 equiv of Cu(II) (blue). Conditions: [**Oro**] = 25 μM; [CuCl$_2$] = 0, 12.5, 25, 50, and 125 μM; pH 7.4; room temperature. Interaction of **Oro** with soluble Cu(II)−Aβ$_{42}$, monitored by (b) ESI-MS and (c) IM-MS. (d) Tandem mass spectrometric analysis in conjunction with CID of the singly oxidized Aβ$_{42}$ (1511 *m/z*). Conditions: [Aβ$_{42}$] = 20 μM; [CuCl$_2$] = 20 μM; [**Oro**] = 100 μM; 100 mM ammonium acetate, pH 7.4; 3 h incubation; no agitation.

Figure 3.1. Rational selection of 12 flavonoids. The presented library of flavonoids was chosen based on structural variations, including the number and position of hydroxyl groups and the location of the B ring, to identify the structural features responsible for reactivities against multiple pathological factors found in AD [*i.e.*, metal-free Aβ, metal–Aβ, free radicals, and AChE].

Figure 3.2. Interaction of the flavonoids with Cu(II) monitored by UV–Vis spectroscopy. Conditions: [flavonoid] = 25 μM; [CuCl$_2$] = 0, 12.5, 25, 50, and 125 μM; 20 mM HEPES, pH 6.6, 150 mM NaCl or EtOH (for **Chr** and **HF**).

Figure 3.3. Influence of the flavonoids on the aggregation of metal-free and metal-treated Aβ$_{42}$. (a) Scheme of the inhibition experiment. (b) Analysis of the MW distribution of the resultant Aβ$_{42}$ species by gel/Western blot with an anti-Aβ antibody (6E10). (c) TEM images of the samples from (b). Conditions: [Aβ$_{42}$] = 25 μM; [CuCl$_2$ or ZnCl$_2$] = 25 μM; [flavonoid] = 50 μM; 20 mM HEPES, pH 7.4 [for metal-free and Zn(II)-containing samples] or pH 6.6 [for Cu(II)-added samples], 150 mM NaCl; 37 °C; 24 h incubation; constant agitation.

Figure 3.4. Impact of the flavonoids on the disassembly and aggregation of preformed metal-free and metal-added Aβ$_{42}$ aggregates. (a) Scheme of the disaggregation experiment. (b) Analysis of the MW distribution of the resultant Aβ$_{42}$ species by gel/Western blot with an anti-Aβ$_{42}$ antibody (6E10). (c) TEM images of the samples from (b). Conditions: [Aβ$_{42}$] = 25 μM; [CuCl$_2$ or ZnCl$_2$] = 25 μM; [flavonoid] = 50 μM; 20 mM HEPES, pH 7.4 [for metal-free and Zn(II)-containing samples] or pH 6.6 [for Cu(II)-added samples], 150 mM NaCl; 37 °C; 24 h incubation; constant agitation.

Figure 3.5. Scavenging activity of the flavonoids against free organic radicals determined by the TEAC assay and their computed redox potentials. (a) Summary of the TEAC values for the flavonoids and their computed redox potentials (E^0 *vs.* SHE). Conditions: EtOH; 25 °C; λ$_{abs}$ = 734 nm. ^{a}This value was obtained from reference 29. ^{b}n.d., not determined. The TEAC values of **Api**, **Chr**, and **HF** could not be obtained due to limited solubility or marginal antioxidant activity levels undetected under our

experimental conditions. (b) Isosurface plots (isodensity value = 0.03 a.u.) of the HOMO energy for **Que**, **Lut**, and **Oro** and their dihedral angles between two planes calculated from carbon coordinates of the A/C rings and the B ring, respectively.

Figure 3.6. Inhibitory activity of the flavonoids against AChE. (a) Summary of the IC_{50} values of the flavonoids against *ee*AChE determined by a fluorometric assay. (b) Intermolecular interactions between the flavonoids and AChE (PDB 1C2O) observed by aMD simulations. (c) Visualization of the flavonoid–AChE interactions modeled through aMD simulations. N, O, and H (from hydroxyl groups) atoms in the flavonoid ligand are depicted in blue, red, and white, respectively. ^{a}n.d., not determined. Inhibitory activity of **Api**, **Chr**, **HF**, and **HIF** against AChE was too low to be detected under our experimental conditions and, thus, an accurate IC_{50} value could not be determined.

Figure 3.7. Alternative binding modes of **Que**, **Lut**, and **Oro** against AChE (PDB 1C2O) modeled through aMD simulations and their % populations (# of snapshots for each cluster / # of snapshots in the total simulation × 100).

Figure 3.8. Computational parameters of the interactions between the selected flavonoids and AChE (PDB 1C2O). (a) Closest distance between hydroxyl groups in the flavonoids and the heteroatom (X = O or N) in the binding pocket. ^{a}n.a., not available. Error bars represent the standard deviation. (b) Calculated mean values for the selected binding determinants: the minimum distance from S203, the number of hydrogen bonding, the SASA of the hydrophobic residues in the binding pocket, and the number of water molecules in the binding pocket.

Figure 3.9. Possible binding modes of **DHF** and **HF** against AChE (PDB 1C2O) generated by aMD simulations and their % populations (# of snapshots for each cluster / # of snapshots in the total simulation × 100).

Figure 3.10. Evaluation of flavonoid-binding determinants against AChE (PDB 1C2O). (a) Closest distance between the flavonoid and S203 of the catalytic triad. (b) Box plot of the number of hydrogen bonding between the flavonoid and AChE. The box extends to the top 25% and bottom 75% of the clustered data. The black line represents the mean value of each computed case. (c) SASA distribution of the hydrophobic residues in the active site. (d) Average count of water molecules in the binding pocket for the apo and holo cases. Error bars represent the standard deviation.

Figure 4.1. Chemical structures of the selected drug repurposing candidates.

Figure 4.2. Effects of the repurposing candidates on the formation of $A\beta_{40}$ and $A\beta_{42}$ aggregates in the absence and presence of metal ions [*i.e.*, Zn(II) and Cu(II)]. (a) Scheme of the inhibition experiments. (b) Analysis of the MW distribution of the resultant Aβ species by gel/Western blot using an anti-Aβ antibody (6E10). Conditions: [$A\beta_{40}$ or $A\beta_{42}$] = 25 μM; [$CuCl_2$ or $ZnCl_2$] = 25 μM; [compound] = 50 μM; 20 mM HEPES, pH 7.4 [for metal-free and Zn(II)-containing samples] or pH 6.6 [for Cu(II)-added samples], 150 mM NaCl; 37 °C; 24 h incubation; constant agitation.

Figure 4.3. Impact of the repurposing candidates on preformed metal-free and metal-treated $A\beta_{40}$ and $A\beta_{42}$ aggregates. (a) Scheme of the disaggregation experiment. (b) Analysis of the molecular weight distribution of the resultant $A\beta_{42}$ species by gel/Western blot with an anti-Aβ antibody (6E10).

Conditions: [Aβ$_{40}$ or Aβ$_{42}$] = 25 μM; [CuCl$_2$ or ZnCl$_2$] = 25 μM; [compound] = 50 μM; 20 mM HEPES, pH 7.4 [for metal-free and Zn(II)-containing samples] or pH 6.6 [for Cu(II)-added samples], 150 mM NaCl; 37 °C; 24 h incubation; constant agitation.

Figure 4.4. UV–Vis spectra monitoring the interactions between the repurposing candidates and Cu(II) in solution. Conditions: [Compounds] = 50 μM; [CuCl$_2$] = 0, 25, 50, 100, and 250 μM; 20 mM HEPES, pH 7.4, 150 mM NaCl; room temperature.

Figure 4.5. Mass spectrometric analyses of the interactions between the repositioning candidates and metal-free and Cu(II)-bound Aβ. (a) ESI-MS data of the Cu(II)–Aβ$_{40}$ samples. (b) ESI-MS data of the Cu(II)–Aβ$_{42}$ samples. Conditions: [Aβ] = 100 μM; [CuCl$_2$] = 100 μM; [Compounds] = 200 μM; 20 mM ammonium acetate, pH 7.4; 37 C; 3 h incubation; no agitation.

Figure 4.6. Mass spectrometric analyses of the interactions between the repositioning candidates and metal-free Aβ. (a) ESI-MS data of the metal-free Aβ$_{40}$ samples. (b) ESI-MS data of the metal-free Aβ$_{42}$ samples. Conditions: [Aβ] = 100 μM; [Compounds] = 200 μM; 20 mM ammonium acetate, pH 7.4; 37 C; 3 h incubation; no agitation.

List of Tables

List of Schemes

List of Abbreviations

AD	Alzheimer's disease
AChE	Acetylcholinesterase
NMDAR	N-methyl-D-aspartate receptor
$A\beta$	Amyloid-β
Metal–$A\beta$	Metal-bound $A\beta$
ACh	Acetylcholine
APP	Amyloid precursor protein
mGluR	Metabotropic glutamate receptor
NFTs	Neurofibrillary tangles
MTBR	Microtubule-binding repeat
MAPs	Microtubule-associated proteins
NMR	Nuclear magnetic resonance
PHFs	Paired helical filaments
SFs	Straight filaments
LLPS	Liquid-liquid phase separation
BBB	Blood-brain barrier
Cu/Zn-SOD	Cu/Zn-superoxide dismutase
CNS	Central nervous system
ROS	Reactive oxygen species
$O_2^{\bullet-}$	Superoxide anion radical
$\bullet$OH	Hydroxyl radical
H_2O_2	Hydrogen peroxide
$\bullet O_2H$	Hydroperoxyl radical
$^1O_2$	Singlet oxygen
O_2^{2-}	Peroxide
^-OH	Hydroxide ion
K_d	Binding affinity
Wt	Wild-type
Oro	Orobol
MW	Molecular weight
TEM	Transmission electron microscopy
ESI-MS	Electrospray ionization mass spectrometry
ESI-MS^2	Tandem ESI-MS

UV–Vis	Ultraviolet-visible spectroscopy
IM-MS	Ion mobility-mass spectrometry
CID	Collision-induced dissociation
TEAC	Trolox equivalent antioxidant capacity
ddH$_2$O	Double-distilled H$_2$O
HEPES	4-(2-Hydroxyethyl)-1-piperazineethanesulfonic acid
TBS	Tris-buffered saline
TBS-T	Tris-buffered saline containing 0.1% Tween-20
*ee*AChE	*Electrophorus electricus* acetylcholinesterase
CAS	Catalytic active site
PAS	Peripheral anionic site
HIF	5-hydroxyisoflavone
Que	Quercetin
Lut	Luteolin
Chr	Chrysin
HF	5-Hydroxyflavone
Kae	Kaempferol
Api	Apigenin
Gen	Genistein
Gal	Galangin
DHIF	5,7-Dihydroxyisoflavone
DHF	3,5-Dihydroxyflavone
HOMO	Highest occupied molecular orbital
aMD	Accelerated molecular dynamics
SASA	Solvent accessible surface area
DFT	Density functional theory
SCRF	Self-consistent reaction field
MD	Molecular dynamics
GAFF	Generalized Amber force field
ISNZ	Isoniazid
IPNZ	Iproniazid
BMX	Benmoxin
QTP	Quetiapine
MAO	Monoamine oxidase

Chapter 1

Multifaceted Pathology of Alzheimer's disease
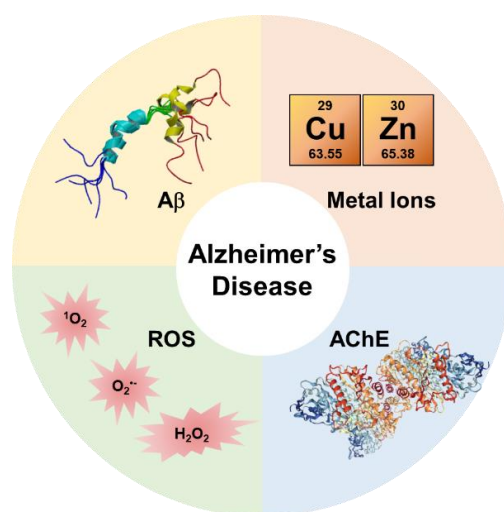
This chapter was adapted from the publications [Savelieff M. G.;[†] Nam, G.;[†] Kang, J.;[†] Lee, H. J.; Lee, M.; Lim, M. H. *Chem. Rev.* **2019**, *119*, 1221–1322 ([†]equal contribution); Nam, G.; Lim, M. H. *Chem. Lett.* **2019**, *48*, 951–960; Nam, G.; Lin, Y.; Lim, M. H.; Lee, Y. H. **2020**, *Submitted for Publication*. I wrote these manuscripts under the direction of Professor Mi Hee Lim.

1.1. Introduction

In recent decades, we have experienced technological advancements at a pace unmatched in history. In the field of Chemical Biology, significant strides have been made with our ability to treat various types of diseases, previously considered terminal. As a result, global mortality rates have declined significantly. This turn of events is evidence of our scientific capabilities in combatting disease through diverse approaches including those surrounding Chemical Biology. In face of such success, a more formidable challenge has surfaced behind the aging population of the world. As a byproduct of our technological advancement, increased life expectancy has led to a general transition of our population with a skewed demographic towards older generations. This phenomenon was accompanied by the increased prevalence of a more insidious disorder with a greater societal and emotional cost: Alzheimer's disease (AD). In this thesis, we first describe our current understanding of AD and the shortcomings in our comprehension and capacity to treat the disease. Thereafter, our multidisciplinary research in search of multifunctional compounds capable of simultaneously targeting multiple pathogenic elements of the disease is presented.

1.2. Alzheimer's disease (AD)

AD is a progressive neurodegenerative disease, predominantly responsible for dementia.[1] Symptoms of AD manifest memory loss and deterioration of cognitive function. An anticipated in AD incidents premised on the aging world population and absence of effective treatments depict the potential detriment of the disease against society.[1] Currently available therapeutics for AD are comprised of acetylcholinesterase (AChE) inhibitors and N-methyl-D-aspartate receptor (NMDAR) antagonists offering temporary relief against the symptoms and progression of the disease.[1,2] These therapeutic approaches utilizing focus on renormalizing the levels of cerebral neurotransmission (*i.e.*, cholinergic and glutamatergic); however, they are unable to arrest the progressive neurodegeneration.[1] Therefore, researchers have been attempting to pinpoint the fundamental cause of the disease. The shear possibility of connected interactions among various factors depicts an incredible network of AD's pathology. Recent efforts to solve the mystery behind what is driving neurodegeneration in AD has led to substantial progress in our understanding of the implicated pathogenic factors. The network among them, however, are only beginning to be explored. For instance, two major factors of AD, amyloid-β (Aβ) and metal ions, have been vigorously investigated for their contribution towards AD, revealing oligomeric Aβ species, gain-of-toxicity of metal ions, and loss-of-function in biological components through metal ion miscompartmentalization as plausible principal causes of AD. In the following sections, four major aspects of AD will be discussed and explored: cholinergic deficit, proteopathy (Aβ and tau), metal ion dyshomeostasis, oxidative stress, and metal-bound Aβ (metal–Aβ).

1.2.1. Cholinergic deficit

Substantial degradation of the hippocampus and cerebral cortex present a physiological hallmark of AD associated with progressive memory loss. More specifically, hippocampal impairments are strongly connected to a retrograde disruption of episodic memories. The hippocampal cholinergic system is subject to notable alterations throughout the various stages of the sleep-wake cycle, critical in memory formation, consolidation, and recall.[3] Acetylcholine (ACh) is the acting neurotransmitter of the cholinergic system released into the synapse upon depolarization to bind to post-synaptic receptors for signal propagation. Implicated as a major neural factor in learning and memory, ACh is also reported to set the dynamics of cortical networks.[4] Thereafter, ACh is released from the receptor and is subject to rapid hydrolysis catalyzed by AChE. AChE exhibits remarkable efficiency in breaking down ACh at the synaptic cleft to rapidly terminate signaling. With this understanding of the cholinergic nervous system, its role in memory, and the observation of decreased ACh levels in the brains of AD patients, researchers have explored the potential pathological role of AChE. Testing this notion further, AChE inhibition was evaluated as a potential therapeutic strategy against AD. Clinical studies revealed that inhibiting the activity of AChE led to an increase in the ACh concentration and temporarily improved cognitive function and memory in AD patients.[5] Utilization of AChE inhibitors as symptomatic remedies followed the introduction of the cholinergic hypothesis pinpointing the deficit of ACh in the brains of AD patients as the main culprit behind the observed neurodegeneration and memory loss.[6]

Despite such progress in our comprehension regarding the cholinergic pathology of AD, pharmaceutical efforts targeting this pathway have proven unsuccessful in stopping the progression of AD-associated neurodegeneration. These failures have led researchers to re-evaluate the cholinergic hypothesis in two schools of thought:[7,8] (i) the cholinergic deficit may be a consequence of the development of the detrimental AD pathology that directly results in the symptomatic memory loss and cognitive deterioration and (ii) the AD pathology manifests a much more complex network of interconnected causative factors (*vide infra*).[1]

1.2.2. Proteopathy

The proteopathic implications of AD represents a major portion of the research efforts allocated to understand its pathogenesis. Although a number of proteins have been proposed to be involved in initiating the pathological development of AD, two main proteins are at the center of the proteopathic facet the disease: Aβ and tau. In this section, we will briefly discuss the pathogenic role of these two proteins with particular respect to their aggregation.

1.2.2.1. Aβ

As the main consistent of senile plaques, Aβ is a proteolytic product of the amyloid precursor protein (APP).[9] Various aspects of Aβ have been investigated in relation to AD: (i) production, (ii) aggregation

and accumulation, (iii) interactions with biological and chemical components (*e.g.*, metal ions and AChE), and (iv) neurotoxic pathways.[1,10,11] Generation of Aβ involves a sequential cleavage of APP *via* β- and γ-secretases producing multiple Aβ isoforms, among which Aβ$_{40}$ and Aβ$_{42}$ are known to be predominant (Figure 1.1).[12,13] Changes in the cleavage site catalyzed by γ-secretase elicit the deviation in length of different Aβ isoforms.[14] The direct participation of secretases in Aβ production has led to attempts in regulating their activities to control the cerebral levels of Aβ.[15,16] Such endeavors, however, have presented a lack of clinical efficacy and unforeseen consequences: for instance, γ-secretase inhibitors negatively affect notch signaling and invoke critical cognitive decline.[17]
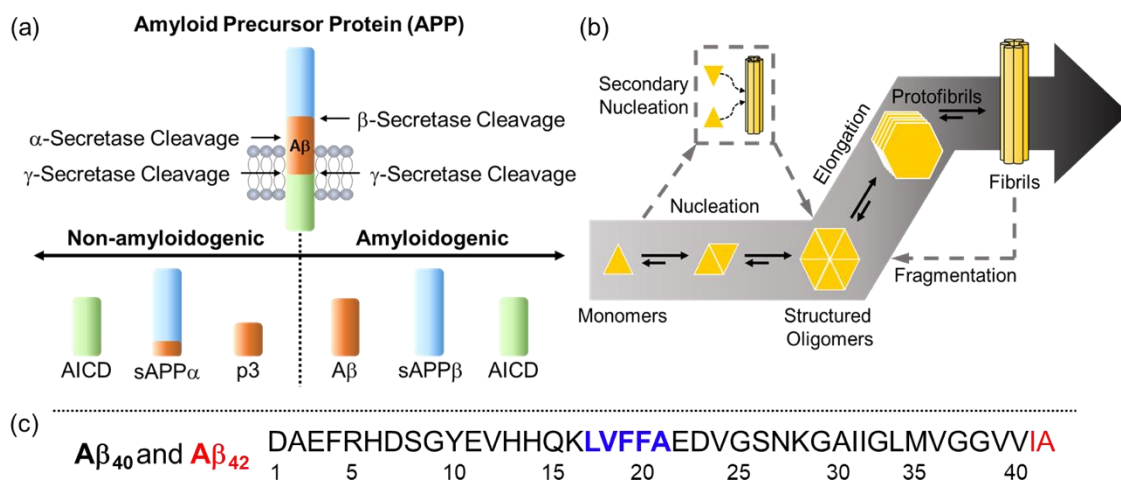
Figure 1.1. The production, aggregation, and amino acid sequence of Aβ. (a) Non-amyloidogenic and amyloidogenic processing of the amyloid precursor protein (APP). (b) Aggregation pathways of Aβ. (c) Amino acid sequence of Aβ$_{40}$ and Aβ$_{42}$; (blue) self-recognition site of Aβ; (red) two additional hydrophobic amino acid residues at the *C*-terminus for Aβ$_{42}$.

Aβ can be found in the kidney, lung, and brain with the brain exhibiting higher concentrations.[18] Extracellular amyloid plaques represent a large portion of the Aβ load in the brain; however, Aβ can also be found intracellularly.[19] Although the innate biological role of Aβ has not been clearly established, research suggests its involvement in lipid homeostasis,[20] memory regulation,[21] and metal transport.[22] The heterogeneity of Aβ stemming from its intrinsically disordered structure presents experimental obstacles in the form of heterogeneity.[23] To facilitate the efforts in elucidating the sectional functions of Aβ, researchers have utilized fragments of full-length Aβ peptides (*i.e.*, Aβ$_{40}$ and Aβ$_{42}$). Recent fragmental analyses of Aβ have reported the structural significance of specific Aβ segments: (i) Aβ$_{1-16}$ is involved in metal coordination (*vide infra*);[24-26] (ii) Aβ$_{17-21}$ is the self-recognition site responsible for driving self-induced aggregation through hydrophobic interactions;[27,28] (iii) Aβ$_{25-35}$ is indicated as the neurotoxic fragment contributing towards aggregation.[29,30]

Aggregation is a key characteristic of Aβ with numerous pathogenic implications. Different Aβ

conformers (*i.e.*, monomers, dimers, oligomers, protofibrils, and fibrils; Figure 1.1b) exist throughout its aggregation pathways.[11,13,31] Research regarding Aβ aggregation and its mechanistic details indicate a complex process contrary to the classical homogeneous primary nucleation.[32] *In vitro* Aβ aggregation can be categorized into three distinct phases: (i) nucleation or lag, (ii) elongation or growth, and (iii) plateau or saturation.[11,13,33-35] Under physiological conditions, Aβ is present at *ca.* nM levels in the brain;[36,37] however, regional increases in Aβ concentration to μM levels through membrane association, macromolecular crowding, or accumulation in organelles can initiate the aggregation cascade of Aβ through a two-step nucleation mechanism.[38] The first step involves seed formation induced by initial hydrophobic interactions between the self-recognition sites of monomeric Aβ entailing a β-sheet transition.[38-40] The second step of nucleation manifests a first-order conformational rearrangement to produce larger oligomers exhibiting amyloidogenic features and toxicity.[38] Such oligomeric species of Aβ subsequently undergo rapid elongation to construct protofibrils and fibrils. Fragmentation of fibrils and secondary nucleation further drive Aβ aggregation during the elongation and plateau phases.[11,32,41,42] An important feature of Aβ accumulation to consider is the transmissibility of Aβ seeds, which could significantly foster the propagation of Aβ aggregation at regions far removed from the site of initial nucleation.[11,43]

The two major isoforms of Aβ, Aβ$_{40}$ and Aβ$_{42}$ (Figure 1.1c), exhibit distinct aggregation pathways.[44] Two additional hydrophobic amino acid residues at the *C*-terminal domain of Aβ$_{42}$ (*i.e.*, I41 and A42) appear to be responsible for the thermodynamic and kinetic differences in their aggregation.[45,46] Research indicate Aβ$_{42}$'s superior propensity for aggregation, relative to that of Aβ$_{40}$, through multiple experimental techniques (*e.g.*, fluorescence assay and electron microscopy).[44,47] A computational study reported in 2017 comparatively analyzed the free energy landscapes of Aβ$_{40}$ and Aβ$_{42}$ aggregation and demonstrated a more downhill free energy profile of the latter isoform.[45] Such notions are further supported by the fact that amyloid plaques can often be found in the AD-affected brains to mainly contain Aβ$_{42}$, despite the presence of Aβ$_{40}$ at greater levels.[47,48] Based on the dominant role of its aggregation, Aβ$_{42}$ is presumed to initiate the amyloidogenic pathology in AD by triggering the nucleation process at critical aggregation concentrations (*ca.* 90 nM).[49-51] Both Aβ$_{40}$ and Aβ$_{42}$ can exist as stable structured oligomers (*e.g.*, trimers and tetramers) at concentrations as low as *ca.* 13 μM, with Aβ$_{42}$ oligomers exhibiting greater stability.[45,52-54] Bitan *et al*. reported an isoform-dependent predisposition for early oligomer conformations (trimer and tetramers for Aβ$_{40}$ and pentamer and hexamer for Aβ$_{42}$), suggesting distinct oligomerization pathways.[55] Furthermore, clinical studies have identified a connection between the cerebral Aβ$_{42}$/Aβ$_{40}$ ratio and cognitive deterioration in AD.[56-58] These observations signify the isoform-dependent association of Aβ with AD.

Aβ oligomers have been increasingly viewed as neurotoxic species responsible for inducing AD-associated neurodegeneration.[11] The heterogeneity of Aβ oligomers and their indefinite identity and

structure, however, present major obstacles in elucidating their conformation-dependent role in AD pathology. Nanomolar concentrations of soluble Aβ oligomers reportedly deteriorate synaptic plasticity, hinder long-term potentiation, invoke spine retraction from pyramidal cells, and impair spatial memory.[59] The molecular mechanisms of Aβ oligomer-induced neuronal detriments include (i) receptor-mediated pathways involving cellular prion protein, APP, NMDAR, α-amino-3-hydroxy-5-methyl-4-isoxazolepropionic acid receptor, metabotropic glutamate receptor (mGluR), α7 nicotinic acetylcholine receptor, and insulin receptor; (ii) β-barrel pore or channel formation leading to ion dyshomeostasis and Ca(II) overload; (iii) membrane permeabilization.[11,60,61] Intracellular Aβ oligomers can also disrupt neuronal homeostasis by inducing endoplasmic reticulum (ER) stress, calcium ion dyshomeostasis, mitochondrial dysfunction, and, ultimately, apoptosis.[11] The physiological significance and specific conformational details of oligomeric Aβ species remain inconclusive and require research regarding oligomer-specific influences towards AD.

The precedence of Aβ pathology to the onset of other pathological features implicated to disrupt neuronal homeostasis is supported by growing evidence indicating that intraneuronal Aβ accumulation occurs during the initial stages of AD.[32] Interrelationships between Aβ and other pathogenic factors (*e.g.*, AChE, metal ions, and ROS) place Aβ at the center of an intricate network eliciting AD-associated neuronal degradation.[1] Ratification of these notions, however, requires a substantial amount of multidisciplinary research ranging from molecular-level to clinical endeavors. Such is the challenge in understanding the multi-faceted pathology of AD. Early accumulation and deposition of various Aβ species (*e.g.*, soluble oligomers and insoluble fibrils) is often considered an initiator for the cascade of AD pathogenesis.[62] Therefore, approaches to regulate Aβ formation, aggregation, degradation, and clearance are currently viewed as potential preventative measures against neurodegeneration in AD.[63] These prevention tactics, however, face the challenge of identifying and diagnosing preclinical AD cases, for which the clinical criteria are yet to be established.[64] The amyloid cascade hypothesis, presently under scrutiny regarding its therapeutic significance, should not be disregarded based on its connection to AD.

1.2.2.2. Tau

Tau is the main component of neurofibrillary tangles (NFTs), another histopathological hallmark of AD. Unlike its proteopathic counterpart Aβ, tau exhibits essential neurobiological function linked to neuronal homeostasis. Tau's contribution in regulating microtubule assembly and stability are critical in neuronal growth and function.[65] Recent studies indicate additional tau functions: modulation of axonal transport and maintaining genomic DNA integrity.[1] Besides its functional roles, tau's connection to the fatal pathology of AD has gathered a great deal of attention.

The six isoforms of tau range from 352 to 441 amino acid residues in human brains manifesting different combinations of structural domains (Figure 1.2). Tau can be divided into four major domains:
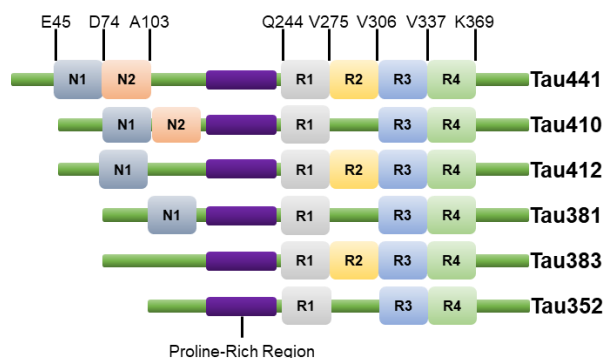
6

Figure 1.2. Six isoforms of tau and their structural characterizations based on amino acid domains. N1 and N2: *N*-terminal projection domains; R1, R2, R3, and R4: Microtubule binding repeat domains.

projection (N1 and N2), proline-rich, microtubule-binding repeat (MTBR), and *C*-terminal. The MTBRs represent three to four imperfectly repeated sequences (R1-R4) (Figure 1.2). Numerous biophysical methods such as nuclear magnetic resonance (NMR), circular dichroism, and Fourier transform infrared spectroscopies have determined that full-length tau is an intrinsically disordered protein without a unique 3D structure.[66] This finding is rationalized by two main physicochemical properties: (i) excess in the number of charged residues (*ca*. 30%) and (ii) relatively small number of hydrophobic residues in the primary sequence of tau (*ca*. 45%).[67] Furthermore, the proline-rich domain further contributes to the disordered structure of tau as proline serves as a secondary structure breaker.

The self-assembly process of tau into paired helical filaments (PHFs) is accompanied by drastic conformational transitions from natively disordered structures to highly ordered β-structures, referred to as amyloidogenesis.[68] Like Aβ, amyloid generation of tau can be fundamentally depicted *via* a two-phase mechanism: (i) the rate-limiting nucleation phase responsible for the observed lag time prior to notable aggregate formation and (ii) the subsequent rapid elongation phase during which the formation and growth of fibrils take place. Two aggregation-prone hexapeptide segments, PHF6 (VQIVYK) and PHF6* (VQIINK), located in the MTBRs are essential for productive nucleation.[69] Interestingly, in addition to PHFs, tau was also observed to form straight filaments (SFs). A recent cryo-EM study revealed important polymorphic aspects of tau amyloid formation. The atomic models of PHFs and SFs derived from the brain of AD patient demonstrated that the structural polymorphism between PHFs and SFs results from the differences in packing between two protofilaments. The two protofilaments of PHFs form identical structures with helical symmetry; however, in SFs, the two protofilaments pack asymmetrically.

It is worth noting that, in addition to amyloid fibrils, tau is capable of forming various types of aggregates such as amorphous aggregates, oligomers, and protofibrils in a condition dependent manner.[70-72] Ostwald ripening describes the kinetic and thermodynamic control of aggregation behavior: soluble tau undergo oligomerization or liquid phase separation prior to fibrillation. Among the different types of tau assemblies, oligomers are implicated as the toxic species possibly responsible for directly

disrupting neuronal homeostasis.[70] The aggregation of amyloidogenic proteins is strongly influenced by various environmental factors and the interactions with other molecules including proteins. Different types of aggregates can be generated as a result of altered ambient conditions such as pH, temperature, and ionic strength.[72-74]

Interestingly, recent studies suggest that ambient conditions were also of critical importance for the liquid-liquid phase separation (LLPS) of a variety of pathological proteins.[75] LLPS is a physical separation of a liquid into two divisible phases. Soluble proteins in solution can undergo phase separation by means of forming liquid droplets. Soluble tau has been reported for its ability to form liquid droplets both *in vitro* and *in vivo*, which denotes significant implications in tau's biological functions and abnormal aggregation. With the clinical failures of Aβ-centric therapeutic approaches, a surge in tau-related AD research has been observed likely due to the direct sptial and temporal connections between tauopathy and neurodegeneration followed by the manifestation of notable AD symptoms such as memory loss. Much more research regarding the exact nature of tau's neurobiological function and pathogenesis with respect to post-translational modifications, aggregation, and microtubule stabilization is required to complete our comprehension. Moreover, numerous reports suggest a connection between Aβ and tau further complicating the matter by including tau in the complex network of AD pathologies.

1.2.3. Metal ion dyshomeostasis

The pertinence of metal ions in neurobiology is manifested by the elevated concentrations of metal ions in the brain, relative to other parts of the body.[1,76-78] Cerebral distributions of metal ions exhibit substantial heterogeneity with a large variance in compartmental metal ion concentrations.[77] The brain presents a dynamic system with immeasurable intricacy with numerous pathways maintaining homeostasis, such as the blood-brain barrier (BBB).[79] Therefore, the brain-specific function, regulation, transport, and metabolism of transition metal ions are not yet fully understood.[76] As redox-active components of enzymes and structural anchors stabilizing a myriad of proteins, metal ions are involved in a wide range of biological roles.[1,76] Synaptic release of transition metal ions upon signal transduction indicate their regulatory roles in neurotransmission.[78] In contrast, neurotoxicity of metal ions through the overproduction of ROS *via* Fenton-like reactions and impediment of vital cellular pathways under pathological conditions present their potential to contribute towards neurodegeneration.[1,76,80-82] For these reasons, strict control of metal ion levels balancing its functionality and toxicity is crucial in proper neuronal function. Disruption of this balance leading to metal ion dyshomeostasis and miscompartmentalization are a key characteristic of AD.[1,82-84] Among transition metal ions, Cu(II) and Zn(II) have been receiving attention as key contributors to AD-associated neurodegeneration.

Challenges in selectively monitoring the levels of metal ions in the brains of live patients make it difficult to directly evaluate the region-specific effects of metal ion dyshomeostasis in a

physiologically relevant manner. Therefore, novel diagnostic tools allowing the selective real-time assessment of cerebral metal ion concentrations could prove useful in investigating how metal ion dysregulation affects neuronal homeostasis and degradation in a healthy brain. Distinguishing the cerebral regions heavily impacted in different stages of AD could also offer the ability to develop personalized therapeutic approaches to re-establish metal ion homeostasis.

Metal ion homeostasis presents an intricate biochemical balance critical for cell survival between their functionality and toxicity. Neurons exhibit greater susceptibility to pathological changes in their environment (*e.g.*, oxidative stress and accumulation neurotoxins) brought upon by the disruption of metal ion homeostasis.[85-89] Based on such notions, chelation therapy is considered a viable option for preventing neuronal deterioration and cognitive decline. Clinical studies evaluating the therapeutic efficacy of metal chelators against AD, however, have yet to result in the development of a drug capable of stopping disease progression.[84] Such outcomes substantiate the complexity of AD pathogeny portraying an interconnected network of multiple pathologies synergistically intertwined to aid in each other's exacerbation and direct neurodegeneration. Among them, the relationship between Aβ and metal ions has been suggested as a plausible contributor in AD, as discussed in Section 1.2.5.

1.2.3.1. Cu(I/II)

Copper is a redox-active transition metal essential for vital enzymes [*e.g.*, cytochrome c oxidase and Cu/Zn-superoxide dismutase (SOD)].[90,91] The highest concentrations of Cu(I/II) can be found in the locus ceruleus at 110–400 μM and substantia nigra at 80–120 μM, at which Cu(I/II) is localized to nerve terminals and secretory vesicles.[92,93] Ca(II)-dependent synaptic secretion of Cu(I/II) plays a regulatory role in the central nervous system (CNS): peptidergic neurons release Cu(I/II) upon depolarization at concentrations up to 15 μM to alter the permeability of granule membranes.[93,94] Cu(I/II) neurotoxicity stems from its proclivity to engage in redox reactions to produce ROS (*e.g.*, hydroxyl radicals) and oxidatively damage critical biological components, such as nucleic acids, proteins, and lipids.[95,96] Cu(I/II) can also induce toxicity by erroneously binding to metal ligands and disrupting their function. For instance, elevated levels of Cu(I/II) can inhibit the activity of lysosomal and cytoplasmic proteases in the cerebral cortex leading to compromised proteolytic degradation mechanisms in neurons, resulting in Aβ accumulation and disruption of neuronal homeostasis.[97] Through the various channels mentioned above, copper is considered a potential triggering agent in AD.[1,98]

1.2.3.2. Zn(II)

Zinc is a redox-inactive transition metal involved in the function of more than 200 proteins.[93] With an ionic radius of 0.74 Å and borderline hardness, Zn(II) preferably binds to nitrogen and sulfur donor atoms.[99] The neocortex and hippocampus exhibit the greatest concentrations of Zn(II). Reports have indicated neocortical Zn(II) concentrations of *ca*. 150–200 μM.[93,100] The vesicles of mossy fibers of the

terminal boutons found in the hippocampus, a region critical for memory, manifest Zn(II) concentrations of 220-300 μM.[101] The synaptic release of Zn(II) takes place during neurotransmission in a Ca(II)-dependent manner from the mossy fiber terminals,[102] reaching concentrations as high as *ca.* 300 μM.[103] Although the physiological role of synaptic Zn(II) remain unclear, researchers have suggested its involvement in controlling normal synaptic transmission, memory formation, and long-term potentiation.[100,104,105] Toxic mechanisms of Zn(II) is comprised of interactions with receptors, transport proteins, and respiratory enzymes, in which Zn(II) can induce excitotoxicity, Ca(II) and Cu(II) dyshomeostasis, and cellular respiratory failure, respectively.[106,107]

1.2.4. Oxidative stress

O_2 chemistry is an essential component of cellular homeostasis providing energy in the form of ATP. As byproducts of cellular respiration which 90% of takes place in mitochondria, reactive oxygen species (ROS) are generated from the inefficiency of the electron transport chain. Oxidative stress is defined as the imbalance between the levels of ROS and antioxidants in a system. Biologically relevant ROS include superoxide anion radical ($O_2^{\bullet-}$), hydroxyl radical ($\bullet OH$), hydrogen peroxide (H_2O_2), hydroperoxyl radical ($\bullet O_2H$), singlet oxygen ($^1O_2$), peroxide (O_2^{2-}), and hydroxide ion (OH^-). Despite their capacity for cellular damage, ROS are critical for a variety of cellular functions such as receptor-mediated signaling pathways, transcriptional activation, apoptosis regulation.[1] A major source of cellular ROS, in the form of $O_2^{\bullet-}$, is a membrane-bound enzyme, nicotinamide adenine dinucleotide phosphate oxidase located in mitochondria and ER.[108]

As an overencompassing pathogenic concept ubiquitous in a wide spectrum of diseases, oxidative stress often presents itself as a bridging factor between distinct pathological pathways. Oxidative stress is a prevailing component in the manifestation of multiple pathological factors (*e.g.*, Aβ, metal ions, and metal−Aβ, *vide infra*) as well as their toxic mechanisms. Elevated levels of ROS can activate the c-Jun *N*-terminal kinase pathway, modulating the expression of β-secretase and Aβ production as a result. In return, Aβ, metal ions, and metal−Aβ are capable of producing ROS under pathological conditions further exacerbating oxidative stress.

1.2.5. Metal–Aβ

Pathological associations between Aβ and metal ions in AD, supported by the detection and characterization of the corresponding complexes, have led to the introduction of a new hybrid concept: metal–Aβ.[109-114] Metal–Aβ bridges the pathogenic principles of the amyloid cascade and metal ion hypotheses, in which their intertwined pathologies are presumed to foster the development and progression of AD. The potential relationship between Aβ and metal ions has been suspected since the discovery of their colocalization in senile plaques.[113] The extracellular presence of various Aβ species and synaptic release of metal ions [*e.g.*, Cu(I/II) and Zn(II)] at micromolar concentrations implicate the
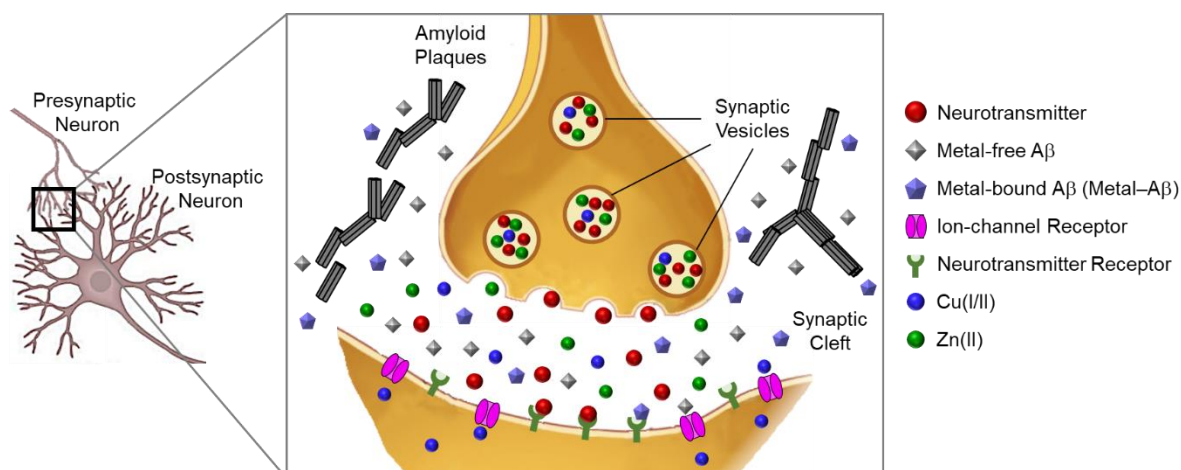
Figure 1.3. Feasibility of the presence of Aβ and metal ions [*e.g.*, Cu(II) and Zn(II)] at the synaptic cleft upon neurotransmission.

biochemical feasibility of their interaction and subsequent formation of metal–Aβ complexes (Figure 1.3).[110,114] Research efforts are illuminating the different facets of the connection between Aβ and metal ions, including metal–Aβ complexation, aggregation, and their toxic mechanisms.

Aβ and metal ions manifest a bilateral relationship in AD. Levels of Aβ are influenced by Cu(II) and Zn(II) through their impact on APP processing, Aβ clearance, and cellular proteolytic capacity; consequently, elevated concentrations of Aβ can alter the cerebral metal ion distribution leading to deficiencies in normally metal-enriched regions of the brain (loss-of-function) and accumulation in amyloid plaques resulting in oxidative damage (gain-of-toxicity).[115,116] Although Aβ pathology is often believed to precede metal ion dyshomeotasis, an in-depth evaluation of the physiological changes during the early preclinical stages of AD is needed to validate this notion.

The flexible structure of Aβ presents dynamic metal–Aβ interactions with numerous proposed binding modes.[117] Coordination modes of Cu(II)–Aβ assume two pH-dependent components: (i) component I at pH 6.5 with 3N1O coordination; (ii) component II at pH > 8 with 3N1O, 4N, and 5N1O coordinations (Figure 1.4a).[1] Zn(II) coordination of Aβ depicts binding sites with various combinations involving 4–6 ligands: *N*-terminal NH$_2$, D1, E3, H6, D7, Y10, E11, H13, and H14 (Figure 1.4b). The feasible Zn(II) coordination mode of Aβ primarily includes histidine residues (*i.e.*, H6, H13, and H14). Y10's participation in Zn(II) binding is facilitated by a metal-induced conformational rearrangement under membrane mimicking conditions.[118] Binding affinities (K_d) of Cu(II)–Aβ and Zn(II)–Aβ range from 10^{-11} to 10^{-7} and 10^{-9} to 10^{-6} M, respectively. A review published in 2019 provides a comprehensive list of the binding modes and binding affinities of metal–Aβ species reported thus far.[1]

Stored in the synaptic vesicles, Cu(II) and Zn(II) are reportedly released into the synaptic cleft upon depolarization reaching micromolar concentrations. Recent evidence suggest that these synaptic metal ions may contribute in controlling neurotransmission through their modulatory effects on the
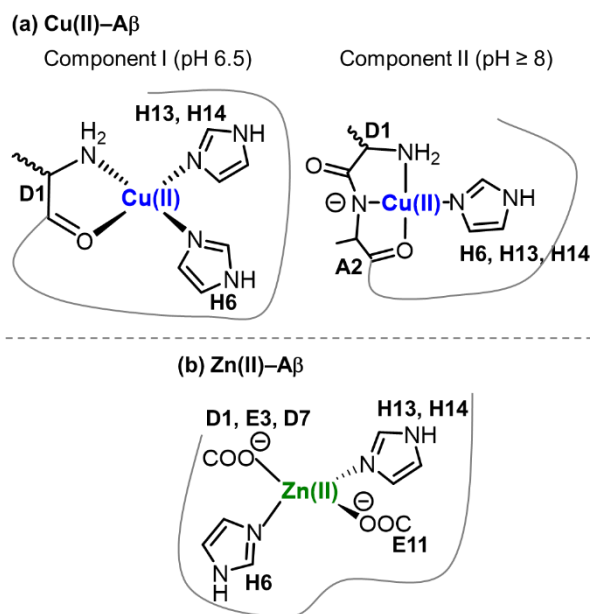
11

Figure 1.4. Proposed metal coordination to Aβ. Binding modes of (a) Cu(II)–Aβ (component I and II) and (b) Zn(II)–Aβ.

postsynaptic receptors. Considering (i) the notable release of metal ions under the dynamic environment presented at the synaptic cleft undergoing rapid changes upon signal transmission, (ii) presence of Aβ in the extracellular matrix in the brains of AD patients and (iii) the strong binding affinity of metal–Aβ, interactions between metal ions and Aβ.

Metal–Aβ interaction has been recognized to affect the aggregation pathways of Aβ.[119] The conditional and conformational dependence of Aβ's metal interaction and aggregation hamper efforts to elucidate the influence of metal ions on Aβ aggregation. Such challenges are manifested by the controversial results from different research groups. Rana *et al.* provide an account of the studies regarding the contradictory effects of Cu(I/II) and Zn(II) on Aβ aggregation.[120] To summarize, Cu(I/II) was observed to hinder the formation of β-sheet-rich fibrillary Aβ aggregates in a stoichiometry-dependent manner.[121-128] Equimolar and greater concentrations of Cu(I/II) promote the generation of non-fibrillary assemblies by accelerating nucleation through the stabilization of Aβ dimers.[39,123,129] Several studies demonstrate Cu(I/II)'s ability to (i) stabilize Aβ oligomers, (ii) disassemble mature Aβ fibrils by abolishing its β-sheet secondary structure, and (iii) subsequently increase Aβ toxicity.[126,128,130-133] Zn(II) was reported to destabilize the intermediate Aβ conformations by accelerating its aggregation kinetics in several studies.[95,101,102] Contradicting data, however, denote that the presence of Zn(II) resulted in the slow aggregation of Aβ leading to amorphous assemblies.[131,134] In short, Cu(I/II) and Zn(II) affect the both aggregation kinetics and pathways of Aβ in a stoichiometry-dependent way modifying the toxicity of the resultant aggregates. Moreover, a report in 2017 by Branch *et al.*, comparing the binding kinetics of Cu(I/II)–Aβ and Zn(II)–Aβ under physiological conditions, proposed

that Cu(I/II)–Aβ complexes are likely responsible for the initial synaptic aggregation of Aβ.[135]

Redox chemistry of Cu(I/II)–Aβ is considered a major toxic mechanism eliciting neurodegeneration in AD. Cu(II)–Aβ coordination results in a rapid reduction to produce Cu(I) and H_2O_2 in the presence of a reducing agent, like ascorbate.[133] The products, Cu(I) and H_2O_2, can further react to form hydroxyl radicals capable of oxidatively damaging vital cellular organelles, including mitochondria.[136,137] The most recent estimate of Cu(II)–Aβ's half potential (0.18 V *vs.* NHE) indicates the possibility of ascorbate-mediated redox cycling of Cu(I/II)–Aβ through Fenton-like reactions.[138-141] Despite these findings, the physiological relevance of such redox chemistry remains questionable due the dynamic nature of the Cu(I/II)–Aβ interaction and its conformation, concentration, target engagement, and electron transfer rate dependence.[129] Therefore, additional studies inquiring the

Figure 1.5. Schematic representation of the multi-faceted pathology of neurodegenerative diseases. (a) Proteopathy of wild-type (wt) or mutant intra- or extracellular unfolded proteins/peptides. Unfolded monomers partially fold and aggregate into oligomers and fibrils. Oligomers may interact with various organelles (*e.g.*, mitochondria) or cell membrane disrupting Ca(II) homeostasis and signaling. (b) Dyshomeostasis of metal ions that, depending on the disease, can bind to misfolded proteins/peptides affecting their aggregation or accumulate in the brain or spinal cord. (c) Elevated oxidative stress resulting from redox-active metal ions (*i.e.*, Cu and Fe) *via* Fenton-like reactions or ROS escaping from damaged mitochondria. ROS can attack cellular proteins, nucleic acids, and lipids causing oxidative damage. (d) Mitochondrial dysfunction and defects in energy metabolism that can occur as a consequence of protein/peptide aggregates. (e) Aberrant axonal transport from hyperphosphorylated microtubule binding proteins, mutant tubulin proteins, or mutant motor proteins. (f) Pervasive, sustained chronic inflammation with reactive microglia and astrocytes as well as altered inflammatory signaling pathways.

conditions observed in AD are needed to ascertain the effects of Cu(I/II)–Aβ-driven redox chemistry in AD pathology.

The abovementioned relationship between Aβ and metal ions in AD indicates the pathogenic relevance and synaptic presence of metal–Aβ. Further research, however, is required to discover the neuropathologically relevant metal–Aβ complexes and conformations, evaluate the toxicity of the relevant metal–Aβ complexes to identify the species responsible for critical neurotoxicity, compare its cerebral localization to the regions of neurodegeneration in the AD-affected brain, and finally resolve its toxic mechanisms in disrupting neuronal homeostasis. Thereby, the roles of metal–Aβ in AD may be precisely understood. Such information would be especially helpful to develop diagnostic and preventative strategies against the disease.

1.3. Conclusions

Increasing evidence regarding the complexity of AD pathology and the failures of numerous clinical trials utilizing therapeutic strategies singly targeting the individual pathogenic elements of AD have fostered the shift in paradigm regarding our understanding of the disease. Recent notions regarding AD etiopathology consider the pathological connections between the various pathological factors of AD. To explain, although research on the individual pathological factors have revealed numerous pathways through which neurodenegeration can be induced, methods of targeting such aspects have proven ineffective. Therefore, researchers have been investigating how these different pathogenic pathways could be intertwined to further contribute towards neurodegeneration. The concept of metal–Aβ serves as an example of such ideas. We believe that this is the beginning of the establishment of the complete picture that is AD pathology. Research indicate connections between Aβ and AChE, Aβ and ROS, AChE and ROS, and Aβ and tau. Experimentally assessing these pathogenic relationships, however, present major challenges due to the complex nature of these individual components of AD and such complications are only augmented when combining multiple concepts together. Major conceptions of AD include proteopathy, metal ion dyshomeostasis, oxidative stress, mitochondrial dysfunction, aberrant axonal transport, and neuroinflammation (Figure 1.5).

1.4. Acknowledgments

1.5. References

1.   Savelieff, M. G.; Nam, G.; Kang, J.; Lee, H. J.; Lee, M.; Lim, M. H., Development of Multifunctional Molecules as Potential Therapeutic Candidates for Alzheimer's Disease,

Parkinson's Disease, and Amyotrophic Lateral Sclerosis in the Last Decade. *Chem. Rev.* **2019**, *119*, 1221-1322.

2. Hashimoto, G.; Kazui, H.; Matsumoto, K.; Nakano, Y.; Yasuda, M.; Mori, E., Does Donepezil Treatment Slow the Progression of Hippocampal Atrophy in Patients With Alzheimer's Disease? *Am. J. Psych.* **2005**, *162*, 676-682.

3. Hasselmo, M. E., Neuromodulation: Acetylcholine and Memory Consolidation. *Trends Cogn. Sci.* **1999**, *3*, 351-359.

4. Hasselmo, M. E.; Bower, J. M., Acetylcholine and Memory. *Trends Neurosci.* **1993**, *16*, 218-222.

5. Zemek, F.; Drtinova, L.; Nepovimova, E.; Sepsova, V.; Korabecny, J.; Klimes, J.; Kuca, K., Outcomes of Alzheimer's Disease Therapy with Acetylcholinesterase Inhibitors and Memantine. *Expert Opin. Drug Safety* **2014**, *13*, 759-774.

6. Hardy, J. A.; Mann, D.; Wester, P.; Winblad, B., An Integrative Hypothesis Concerning the Pathogenesis and Progression of Alzheimer's Disease. *Neurobiol. Aging* **1986**, *7*, 489-502.

7. Craig, L. A.; Hong, N. S.; McDonald, R. J., Revisiting the Cholinergic Hypothesis in the Development of Alzheimer's Disease. *Neurosci. Biobehav. Rev.* **2011**, *35*, 1397-1409.

8. Cummings, J. L.; Kaufer, D., Neuropsychiatric Aspects of Alzheimer's Disease. The Cholinergic Hypothesis Revisited. *Neurology* **1996**, *47*, 876-883.

9. Vassar, R.; Bennett, B. D.; Babu-Khan, S.; Kahn, S.; Mendiaz, E. A.; Denis, P.; Teplow, D. B.; Ross, S.; Amarante, P.; Loeloff, R.; Luo, Y.; Fisher, S.; Fuller, J.; Edenson, S.; Lile, J.; Jarosinski, M. A.; Biere, A. L.; Curran, E.; Burgess, T.; Louis, J.-C.; Collins, F.; Treanor, J.; Rogers, G.; Citron, M., β-Secretase Cleavage of Alzheimer's Amyloid Precursor Protein by the Transmembrane Aspartic Protease BACE. *Science* **1999**, *286*, 735-741.

10. Kepp, K. P., Bioinorganic chemistry of Alzheimer's disease. *Chem. Rev.* **2012**, *112*, 5193-5239.

11. Lee, S. J. C.; Nam, E.; Lee, H. J.; Savelieff, M. G.; Lim, M. H., Towards an Understanding of Amyloid-β Oligomers: Characterization, Toxicity Mechanisms, and Inhibitors. *Chem. Soc. Rev.* **2017**, *46*, 310-323.

12. DeToma, A. S.; Salamekh, S.; Ramamoorthy, A.; Lim, M. H., Misfolded Proteins in Alzheimer's Disease and Type II Diabetes. *Chem. Soc. Rev.* **2012**, *41*, 608-621.

13. Savelieff, M. G.; Lee, S.; Liu, Y.; Lim, M. H., Untangling Amyloid-β, Tau, and Metals in Alzheimer's Disease. *ACS Chem. Biol.* **2013**, *8*, 856-865.

14. Thathiah, A.; Horré, K.; Snellinx, A.; Vandewyer, E.; Huang, Y.; Ciesielska, M.; De Kloe, G.; Munck, S.; De Strooper, B., β-arrestin 2 Regulates Aβ Generation and γ-secretase Activity in Alzheimer's Disease. *Nat. Med.* **2013**, *19*, 43-49.

15. Ding, Y.; Ko, M. H.; Pehar, M.; Kotch, F.; Peters, N. R.; Luo, Y.; Salamat, S. M.; Puglielli, L., Biochemical Inhibition of the Acetyltransferases ATase1 and ATase2 Reduces β-Secretase (BACE1) Levels and Aβ Generation. *J. Biol. Chem.* **2012**, *287*, 8424-8433.

16. Ghosh, A. K.; Brindisi, M.; Tang, J., Developing β-secretase Inhibitors for Treatment of Alzheimer's Disease. *J. Neurochem.* **2012**, *120*, 71-83.

17. De Strooper, B.; Annaert, W.; Cupers, P.; Saftig, P., A Presenilin-1-dependent Gamma-secretase-like Protease Mediates Release of Notch Intracellular Domain. *Nature* **1999**, *398*, 518-522.

18. Skodras, G.; Peng, J. H.; Parker, J. C., Jr.; Kragel, P. J., Immunohistochemical Localization of Amyloid beta-protein Deposits in Extracerebral Tissues of Patients with Alzheimer's Disease. *Ann. Clin. Lab. Sci.* **1993**, *23*, 275-280.

19. Leuner, K.; Müller, W. E.; Reichert, A. S., From Mitochondrial Dysfunction to Amyloid Beta Formation: Novel Insights into the Pathogenesis of Alzheimer's Disease. *Mol. Neurobiol.* **2012**, *46*, 186-193.

20. Grösgen, S.; Grimm, M. O. W.; Frieß, P.; Hartmann, T., Role of Amyloid Beta in Lipid Homeostasis. *Biochim. Biophys. Acta* **2010**, *1801*, 966-974.

21. Morley, J. E.; Farr, S. A., The Role of Amyloid-beta in the Regulation of Memory. *Biochem. Pharmacol.* **2014**, *88*, 479-485.

22. Maynard, C. J.; Bush, A. I.; Masters, C. L.; Cappai, R.; Li, Q.-X., Metals and Amyloid-β in Alzheimer's Disease. *Int. J. Exp. Pathol.* **2005**, *86*, 147-159.

23. Meng, F.; Bellaiche, M. M. J.; Kim, J.-Y.; Zerze, G. H.; Best, R. B.; Chung, H. S., Highly Disordered Amyloid-β Monomer Probed by Single-Molecule FRET and MD Simulation. *Biophys. J.* **2018**, *114*, 870-884.

24. Lanza, V.; Bellia, F.; Rizzarelli, E., An Inorganic Overview of Natural Aβ Fragments: Copper(II) and Zinc(II)-mediated Pathways. *Coord. Chem. Rev.* **2018**, *369*, 1-14.

25. Dorlet, P.; Gambarelli, S.; Faller, P.; Hureau, C., Pulse EPR Spectroscopy Reveals the Coordination Sphere of Copper(II) Ions in the 1–16 Amyloid-β Peptide: A Key Role of the First Two *N*-Terminus Residues. *Angew. Chem. Int. Ed.* **2009**, *48*, 9273-9276.

26. Danielsson, J.; Pierattelli, R.; Banci, L.; Gräslund, A., High-resolution NMR Studies of the Zinc-binding Site of the Alzheimer's Amyloid β-peptide. *FEBS J.* **2007**, *274*, 46-59.

27. Tjernberg, L. O.; Naslund, J.; Lindqvist, F.; Johansson, J.; Karlstrom, A. R.; Thyberg, J.; Terenius, L.; Nordstedt, C., Arrest of β-amyloid Fibril Formation by a Pentapeptide Ligand. .*J. Biol. Chem.* **1996**, *271*, 8545-8548.

28. Takahashi, T.; Mihara, H., Peptide and Protein Mimetics Inhibiting Amyloid β-Peptide Aggregation. *Acc. Chem. Res.* **2008**, *41*, 1309-1318.

29. Fan, S.; Zhang, B.; Luan, P.; Gu, B.; Wan, Q.; Huang, X.; Liao, W.; Liu, J., PI3K/AKT/mTOR/p70S6K Pathway is Involved in Aβ25-35-induced Autophagy. *Biomed. Res. Int.* **2015**, *2015*, 161020.

30. Ramírez, E.; Mendieta, L.; Flores, G.; Limón, I. D., Neurogenesis and Morphological-neural Alterations Closely Related to Amyloid β-peptide (25–35)-induced Memory Impairment in Male Rats. *Neuropeptides* **2018**, *67*, 9-19.

31. Rijal Upadhaya, A.; Kosterin, I.; Kumar, S.; von Arnim, C. A. F.; Yamaguchi, H.; Fändrich, M.; Walter, J.; Thal, D. R., Biochemical Stages of Amyloid-β Peptide Aggregation and Accumulation in the Human Brain and their Association with Symptomatic and Pathologically Preclinical Alzheimer's Disease. *Brain* **2014**, *137*, 887-903.

32. Cohen, S. I. A.; Linse, S.; Luheshi, L. M.; Hellstrand, E.; White, D. A.; Rajah, L.; Otzen, D. E.; Vendruscolo, M.; Dobson, C. M.; Knowles, T. P. J., Proliferation of Amyloid-β42 Aggregates Occurs through a Secondary Nucleation Mechanism. *Proc. Natl. Acad. Sci. U.S.A.* **2013**, *110*, 9758-9763.

33. Stroo, E.; Koopman, M.; Nollen, E. A. A.; Mata-Cabana, A., Cellular Regulation of Amyloid Formation in Aging and Disease. *Front. Neurosci.* **2017**, *11*, 64.

34. Iannuzzi, C.; Irace, G.; Sirangelo, I., Differential Effects of Glycation on Protein Aggregation and Amyloid Formation. *Front. Mol. Biosci.* **2014**, *1*, 9.

35. Wallin, C.; Sholts, S. B.; Österlund, N.; Luo, J.; Jarvet, J.; Roos, P. M.; Ilag, L.; Gräslund, A.; Wärmländer, S. K. T. S., Alzheimer's Disease and Cigarette Smoke Components: Effects of Nicotine, PAHs, and Cd(II), Cr(III), Pb(II), Pb(IV) Ions on Amyloid-β Peptide Aggregation. *Sci. Rep.* **2017**, *7*, 14423.

36. Walsh, D. M.; Klyubin, I.; Fadeeva, J. V.; Cullen, W. K.; Anwyl, R.; Wolfe, M. S.; Rowan, M. J.; Selkoe, D. J., Naturally Secreted Oligomers of Amyloid β Protein Potently Inhibit Hippocampal Long-term Potentiation In Vivo. *Nature* **2002**, *416*, 535-539.

37. Andreasen, N.; Hesse, C.; Davidsson, P.; Minthon, L.; Wallin, A.; Winblad, B.; Vanderstichele, H.; Vanmechelen, E.; Blennow, K., Cerebrospinal Fluid β-Amyloid(1-42) in Alzheimer Disease: Differences Between Early- and Late-Onset Alzheimer Disease and Stability During the Course of Disease. *Arch. Neurol.* **1999**, *56*, 673-680.

38. Castello, F.; Paredes, J. M.; Ruedas-Rama, M. J.; Martin, M.; Roldan, M.; Casares, S.; Orte, A., Two-Step Amyloid Aggregation: Sequential Lag Phase Intermediates. *Sci. Rep.* **2017**, *7*, 40065.

39. Hane, F.; Tran, G.; Attwood, S. J.; Leonenko, Z., Cu^{2+} Affects Amyloid-β (1–42) Aggregation by Increasing Peptide-Peptide Binding Forces. *PloS One* **2013**, *8*, e59005.

40. Bleiholder, C.; Dupuis, N. F.; Wyttenbach, T.; Bowers, M. T., Ion Mobility–Mass Spectrometry Reveals a Conformational Conversion from Random Assembly to β-sheet in Amyloid Fibril Formation. *Nat. Chem.* **2010**, *3*, 172-177.

41. Hellewell, A. L.; Hewitt, E. W.; Radford, S. E., Fibril Fragmentation in Amyloid Assembly and Cytotoxicity. *Prion* **2010**, *4*, 20-25.

42.   Jeong, J. S.; Ansaloni, A.; Mezzenga, R.; Lashuel, H. A.; Dietler, G., Novel Mechanistic Insight into the Molecular Basis of Amyloid Polymorphism and Secondary Nucleation during Amyloid Formation. *J. Mol. Biol.* **2013**, *425*, 1765-1781.

43.   Nath, S.; Agholme, L.; Kurudenkandy, F. R.; Granseth, B.; Marcusson, J.; Hallbeck, M., Spreading of Neurodegenerative Pathology via Neuron-to-Neuron Transmission of β-Amyloid. *J. Neurosci.* **2012**, *32*, 8767-8777.

44.   Qiu, T.; Liu, Q.; Chen, Y.-X.; Zhao, Y.-F.; Li, Y.-M., Aβ42 and Aβ40: Similarities and Differences. *J. Pept. Sci.* **2015**, *21*, 522-529.

45.   Zheng, W.; Tsai, M.-Y.; Wolynes, P. G., Comparing the Aggregation Free Energy Landscapes of Amyloid Beta(1–42) and Amyloid Beta(1–40). *J. Am. Chem. Soc.* **2017**, *139*, 16666-16676.

46.   Jarrett, J. T.; Berger, E. P.; Lansbury, P. T., The Carboxy Terminus of the beta Amyloid Protein is Critical for the Seeding of Amyloid Formation: Implications for the Pathogenesis of Alzheimer's Disease. *Biochemistry* **1993**, *32*, 4693-4697.

47.   Vandersteen, A.; Hubin, E.; Sarroukh, R.; De Baets, G.; Schymkowitz, J.; Rousseau, F.; Subramaniam, V.; Raussens, V.; Wenschuh, H.; Wildemann, D.; Broersen, K., A Comparative Analysis of the Aggregation Behavior of Amyloid-β Peptide Variants. *FEBS Lett.* **2012**, *586*, 4088-4093.

48.   Gu, L.; Guo, Z., Alzheimer's Aβ42 and Aβ40 Peptides Form Interlaced Amyloid Fibrils. *J. Neurochem.* **2013**, *126*, 305-311.

49.   Iwatsubo, T.; Odaka, A.; Suzuki, N.; Mizusawa, H.; Nukina, N.; Ihara, Y., Visualization of Aβ42(43) and Aβ40 in Senile Plaques with End-specific Aβ Monoclonals: Evidence that an Initially Deposited Species is Aβ42(43). *Neuron* **1994**, *13*, 45-53.

50.   Xiao, Y.; Ma, B.; McElheny, D.; Parthasarathy, S.; Long, F.; Hoshi, M.; Nussinov, R.; Ishii, Y., Aβ(1–42) Fibril Structure Illuminates Self-recognition and Replication of Amyloid in Alzheimer's disease. *Nat. Struct. Mol. Biol.* **2015**, *22*, 499-505.

51.   Novo, M.; Freire, S.; Al-Soufi, W., Critical Aggregation Concentration for the Formation of Early Amyloid-β (1–42) Oligomers. *Sci. Rep.* **2018**, *8*, 1783.

52.   Chen, Y.-R.; Glabe, C. G., Distinct Early Folding and Aggregation Properties of Alzheimer Amyloid-β Peptides Aβ40 and Aβ42: Stable Trimer or Tetramer Formation by Aβ42. *J. Biol. Chem.* **2006**, *281*, 24414-24422.

53.   Breydo, L.; Kurouski, D.; Rasool, S.; Milton, S.; Wu, J. W.; Uversky, V. N.; Lednev, I. K.; Glabe, C. G., Structural Differences between Amyloid Beta Oligomers. *Biochem. Biophys. Res. Commun.* **2016**, *477*, 700-705.

54.   Pauwels, K.; Williams, T. L.; Morris, K. L.; Jonckheere, W.; Vandersteen, A.; Kelly, G.; Schymkowitz, J.; Rousseau, F.; Pastore, A.; Serpell, L. C.; Broersen, K., Structural Basis for Increased Toxicity of Pathological Aβ42:Aβ40 Ratios in Alzheimer Disease. *J. Biol. Chem.* **2012**, *287*, 5650-5660.

55.   Bitan, G.; Kirkitadze, M. D.; Lomakin, A.; Vollers, S. S.; Benedek, G. B.; Teplow, D. B., Amyloid β-protein (Aβ) Assembly: Aβ40 and Aβ42 Oligomerize through Distinct Pathways. *Proc. Natl. Acad. Sci. U.S.A.* **2003**, *100*, 330-335.

56.   Murray, P. S.; Kirkwood, C. M.; Gray, M. C.; Ikonomovic, M. D.; Paljug, W. R.; Abrahamson, E. E.; Henteleff, R. A.; Hamilton, R. L.; Kofler, J. K.; Klunk, W. E.; Lopez, O. L.; Penzes, P.; Sweet, R. A., beta-Amyloid 42/40 Ratio and Kalirin Expression in Alzheimer Disease with Psychosis. *Neurobiol. Aging* **2012**, *33*, 2807-2816.

57.   Wiltfang, J.; Esselmann, H.; Bibl, M.; Hull, M.; Hampel, H.; Kessler, H.; Frolich, L.; Schroder, J.; Peters, O.; Jessen, F.; Luckhaus, C.; Perneczky, R.; Jahn, H.; Fiszer, M.; Maler, J. M.; Zimmermann, R.; Bruckmoser, R.; Kornhuber, J.; Lewczuk, P., Amyloid beta Peptide Ratio 42/40 but not A beta 42 Correlates with Phospho-Tau in Patients with Low- and High-CSF A beta 40 Load. *J. Neurochem.* **2007**, *101*, 1053-1059.

58.   Waragai, M.; Yoshida, M.; Mizoi, M.; Saiki, R.; Kashiwagi, K.; Takagi, K.; Arai, H.; Tashiro, J.; Hashimoto, M.; Iwai, N.; Uemura, K.; Igarashi, K., Increased Protein-conjugated Acrolein and Amyloid-beta40/42 Ratio in Plasma of Patients with Mild Cognitive Impairment and Alzheimer's Disease. *J. Alzheimers Dis.* **2012**, *32*, 33-41.

59. Lauren, J.; Gimbel, D. A.; Nygaard, H. B.; Gilbert, J. W.; Strittmatter, S. M., Cellular Prion Protein Mediates Impairment of Synaptic Plasticity by Amyloid-beta Oligomers. *Nature* **2009**, *457*, 1128-1132.

60. Benilova, I.; Karran, E.; De Strooper, B., The Toxic Aβ Oligomer and Alzheimer's Disease: an Emperor in Need of Clothes. *Nat. Neurosci.* **2012**, *15*, 349-357.

61. Serra-Batiste, M.; Tolchard, J.; Giusti, F.; Zoonens, M.; Carulla, N., Stabilization of a Membrane-Associated Amyloid-β Oligomer for Its Validation in Alzheimer's Disease. *Front. Mol. Biosci.* **2018**, *5*, 38.

62. Ingelsson, M.; Fukumoto, H.; Newell, K. L.; Growdon, J. H.; Hedley–Whyte, E. T.; Frosch, M. P.; Albert, M. S.; Hyman, B. T.; Irizarry, M. C., Early Aβ accumulation and progressive synaptic loss, gliosis, and tangle formation in AD brain. *Neurology* **2004**, *62*, 925-931.

63. Brubaker, G. R.; Johnson, D. W., Molecular Mechanics Calculations in Coordination Chemistry. *Coord. Chem. Rev.* **1984,** *53*, 1-36.

64. Sperling, R. A.; Aisen, P. S.; Beckett, L. A.; Bennett, D. A.; Craft, S.; Fagan, A. M.; Iwatsubo, T.; Jack, C. R.; Kaye, J.; Montine, T. J.; Park, D. C.; Reiman, E. M.; Rowe, C. C.; Siemers, E.; Stern, Y.; Yaffe, K.; Carrillo, M. C.; Thies, B.; Morrison-Bogorad, M.; Wagster, M. V.; Phelps, C. H., Toward defining the preclinical stages of Alzheimer's disease: Recommendations from the National Institute on Aging-Alzheimer's Association Workgroups on Diagnostic Guidelines for Alzheimer's disease. *Alzheimers Dement.* **2011**, *7*, 280-292.

65. Savelieff, M. G.; Lee, S.; Liu, Y.; Lim, M. H., Untangling Amyloid-beta, Tau, and Metals in Alzheimer's Disease. *ACS Chem. Biol.* **2013**, *8*, 856-865.

66. Zhao, J.; Huvent, I.; Lippens, G.; Eliezer, D.; Zhang, A.; Li, Q.; Tessier, P.; Linhardt, R. J.; Zhang, F.; Wang, C., Glycan Determinants of Heparin-Tau Interaction. *Biophys. J.* **2017**, *112*, 921-932.

67. Zhu, H.-L.; Fernández, C.; Fan, J.-B.; Shewmaker, F.; Chen, J.; Minton, A. P.; Liang, Y., Quantitative Characterization of Heparin Binding to Tau Protein: Implication for Inducer-Mediated Tau Filament Formation. *J. Biol. Chem.* **2010**, *285*, 3592-3599.

68. Goedert, M.; Wischik, C. M.; Crowther, R. A.; Walker, J. E.; Klug, A., Cloning and Sequencing of the cDNA Encoding a Core Protein of the Paired Helical Filament of Alzheimer Disease: Identification as the Microtubule-Associated Protein Tau. *Proc. Natl. Acad. Sci. U.S.A.* **1988**, *85*, 4051-4055.

69. Ramachandran, G.; Udgaonkar, J. B., Understanding the Kinetic Roles of the Inducer Heparin and of Rod-like Protofibrils during Amyloid Fibril Formation by Tau Protein. *J. Biol. Chem.* **2011**, *286*, 38948-38959.

70. Despres, C.; Di, J.; Cantrelle, F.-X.; Li, Z.; Huvent, I.; Chambraud, B.; Zhao, J.; Chen, J.; Chen, S.; Lippens, G.; Zhang, F.; Linhardt, R.; Wang, C.; Klärner, F.-G.; Schrader, T.; Landrieu, I.; Bitan, G.; Smet-Nocca, C., Major Differences between the Self-Assembly and Seeding Behavior of Heparin-Induced and In Vitro Phosphorylated Tau and Their Modulation by Potential Inhibitors. *ACS Chem. Biol.* **2019**, *14*, 1363-1379.

71. Fitzpatrick, A. W. P.; Falcon, B.; He, S.; Murzin, A. G.; Murshudov, G.; Garringer, H. J.; Crowther, R. A.; Ghetti, B.; Goedert, M.; Scheres, S. H. W., Cryo-EM structures of tau filaments from Alzheimer's disease. *Nature* **2017**, *547*, 185-190.

72. Arrasate, M.; Pérez, M.; Valpuesta, J. M.; Avila, J., Role of Glycosaminoglycans in Determining the Helicity of Paired Helical Filaments. *Am. J. Pathol.* **1997**, *151*, 1115-1122.

73. Lin, Y.; Sahoo, B. R.; Ozawa, D.; Kinoshita, M.; Kang, J.; Lim, M. H.; Okumura, M.; Huh, Y. H.; Moon, E.; Jang, J. H.; Lee, H. J.; Ryu, K. Y.; Ham, S.; Won, H. S.; Ryu, K. S.; Sugiki, T.; Bang, J. K.; Hoe, H. S.; Fujiwara, T.; Ramamoorthy, A.; Lee, Y. H., Diverse Structural Conversion and Aggregation Pathways of Alzheimer's Amyloid-beta (1-40). *ACS Nano* **2019**, *13*, 8766-8783.

74. Goedert, M.; Jakes, R.; Spillantini, M. G.; Hasegawa, M.; Smith, M. J.; Crowther, R. A., Assembly of Microtubule-associated Protein Tau into Alzheimer-like Filaments Induced by Sulphated Glycosaminoglycans. *Nature* **1996**, *383*, 550-553.

75. Shin, Y.; Brangwynne, C. P., Liquid Phase Condensation in Cell Physiology and Disease. *Science* **2017**, *357*, 1253.

76. Que, E. L.; Domaille, D. W.; Chang, C. J., Metals in Neurobiology: Probing their Chemistry and Biology with Molecular Imaging. *Chem. Rev.* **2008**, *108*, 1517-1549.

77. Popescu, B. F. G.; Nichol, H., Mapping Brain Metals to Evaluate Therapies for Neurodegenerative Disease. *CNS Neurosci. Therap.* **2011**, *17*, 256-268.

78. Chang, C. J., Bioinorganic Life and Neural Activity: Toward a Chemistry of Consciousness? *Acc. Chem. Res.* **2017**, *50*, 535-538.

79. Zheng, W.; Aschner, M.; Ghersi-Egea, J.-F., Brain Barrier Systems: a New Frontier in Metal Neurotoxicological Research. *Toxicol. Appl. Pharmacol.* **2003**, *192*, 1-11.

80. Pham, A. N.; Xing, G.; Miller, C. J.; Waite, T. D., Fenton-like Copper Redox Chemistry Revisited: Hydrogen Peroxide and Superoxide Mediation of Copper-catalyzed Oxidant Production. *J. Catal.* **2013**, *301*, 54-64.

81. Kehrer, J. P., The Haber–Weiss Reaction and Mechanisms of Toxicity. *Toxicology* **2000**, *149*, 43-50.

82. Bush, A. I., The Metallobiology of Alzheimer's Disease. *Trends Neurosci.* **2003**, *26*, 207-214.

83. Lee, H. J.; Korshavn, K. J.; Kochi, A.; Derrick, J. S.; Lim, M. H., Cholesterol and Metal Ions in Alzheimer's Disease. *Chem. Soc. Rev.* **2014**, *43*, 6672-6682.

84. Bush, A. I.; Tanzi, R. E., Therapeutics for Alzheimer's Disease based on the Metal Hypothesis. *Neurotherapeutics* **2008**, *5*, 421-432.

85. Cobley, J. N.; Fiorello, M. L.; Bailey, D. M., 13 Reasons Why the Brain is Susceptible to Oxidative Stress. *Redox Biol.* **2018**, *15*, 490-503.

86. Bell, K. F. S., Insight into a Neuron's Preferential Susceptibility to Oxidative Stress. *Biochem. Soc. Trans.* **2013**, *41*, 1541-1545.

87. Geddes, D. M.; LaPlaca, M. C.; Cargill, R. S., Susceptibility of Hippocampal Neurons to Mechanically Induced Injury. *Exp. Neurol.* **2003**, *184*, 420-427.

88. Haddad, D.; Nakamura, K., Understanding the Susceptibility of Dopamine Neurons to Mitochondrial Stressors in Parkinson's Disease. *FEBS Lett.* **2015**, *589*, 3702-3713.

89. Mitchell, I.; Griffiths, M., The Differential Susceptibility of Specific Neuronal Populations: Insights from Huntington's Disease. *IUBMB Life* **2003**, *55*, 293-298.

90. Iwata, S.; Ostermeier, C.; Ludwig, B.; Michel, H., Structure at 2.8 Å Resolution of Cytochrome C Cxidase from Paracoccus Denitrificans. *Nature* **1995**, *376*, 660-669.

91. Richardson, J.; Thomas, K. A.; Rubin, B. H.; Richardson, D. C., Crystal Structure of Bovine Cu,Zn Superoxide Dismutase at 3 A Resolution: Chain Tracing and Metal Ligands. *Proc. Natl. Acad. Sci. U.S.A.* **1975**, *72*, 1349-1353.

92. Bogdan, F. G. P.; Martin, J. G.; Uwe, B.; Alex, V. G.; Michael, E. K.; Richard, P. E. M.; Katharina, L.; Richard, M. D.; Graham, N. G.; Akela, D. H.; Sheri, M. H.; Chapman, L. D.; Ingrid, J. P.; Helen, N., Mapping Metals in Parkinson's and Normal Brain using Rapid-scanning X-ray Fluorescence. *Phys. Med. Biol.* **2009**, *54*, 651-663.

93. Sigel, A.; Sigle, H., *Metal Ions in Biological Systems: Interrelations between Free Radicals and Metal Ions in Life Processes*; Routledge: New York, **2017**; Volume 36.

94. Vassallo, N.; Herms, J., Cellular Prion Protein Function in Copper Homeostasis and Redox Signalling at the Synapse. *J. Neurochem.* **2003**, *86*, 538-544.

95. Lan, A.-p.; Xiong, X.-j.; Chen, J.; Wang, X.; Chai, Z.-f.; Hu, Y., AMPK Inhibition Enhances the Neurotoxicity of Cu(II) in SH-SY5Y Cells. *Neurotox. Res.* **2016**, *30*, 499-509.

96. Barnham, K. J.; Bush, A. I., Biological Metals and Metal-targeting Compounds in Major Neurodegenerative Diseases. *Chem. Soc. Rev.* **2014**, *43*, 6727-6749.

97. Falkous, G.; Harris, J. B.; Mantle, D., Effect of Neurotoxic Metal Ions In Vitro on Proteolytic Enzyme Activities in Human Cerebral Cortex. *Clin. Chim. Acta* **1995**, *238*, 125-135.

98. Brewer, G. J., Divalent Copper as a Major Triggering Agent in Alzheimer's Disease. *J. Alzheimers Dis.* **2015**, *46*, 593-604.

99. Wells, A. F., *Structural Inorganic Chemistry*. Oxford University Press: Oxford, **2012**; 5th Ed.

100. Sensi, S. L.; Paoletti, P.; Bush, A. I.; Sekler, I., Zinc in the Physiology and Pathology of the CNS. *Nat. Rev. Neurosci.* **2009,** *10*, 780-791.

101. Cuajungco, M. P.; Lees, G. J.; Kydd, R. R.; Tanzi, R. E.; Bush, A. I., Zinc and Alzheimer's Disease: An Update. *Nutr. Neurosci.* **1999**, *2*, 191-208.

102. Ketterman, J. K.; Li, Y. V., Presynaptic Evidence for Zinc Release at the Mossy Fiber Synapse of Rat Hippocampus. *J. Neurosci. Res.* **2008**, *86*, 422-434.

103. Paoletti, P.; Vergnano, A. M.; Barbour, B.; Casado, M., Zinc at Glutamatergic Synapses. *Neuroscience* **2009**, *158*, 126-136.

104. Sullivan, J. A.; Zhang, X.-l.; Sullivan, A. P.; Vose, L. R.; Moghadam, A. A.; Fried, V. A.; Stanton, P. K., Zinc Enhances Hippocampal Long-term Potentiation at CA1 Synapses through NR2B containing NMDA Receptors. *PloS One* **2018**, *13*, e0205907.

105. Takeda, A.; Tamano, H., The Impact of Synaptic Zn^{2+} Dynamics on Cognition and Its Decline. *Int. J. Mol. Sci.* **2017**, *18*, 2411.

106. Kiselyov, K.; Muallem, S., ROS and Intracellular Ion Channels. *Cell Calcium* **2016**, *60*, 108-114.

107. Dineley, K. E.; Votyakova, T. V.; Reynolds, I. J., Zinc Inhibition of Cellular Energy Production: Implications for Mitochondria and Neurodegeneration. *J. Neurochem.* **2003**, *85*, 563-570.

108. Finkel, T.; Holbrook, N. J., Oxidants, Oxidative Stress and the Biology of Aging. *Nature* **2000**, *408*, 239-247.

109. Asandei, A.; Iftemi, S.; Mereuta, L.; Schiopu, I.; Luchian, T., Probing of Various Physiologically Relevant Metals-amyloid-beta Peptide Interactions with a Lipid Membrane-immobilized Protein Nanopore. *J Membr. Biol.* **2014**, *247*, 523-530.

110. Pithadia, A. S.; Lim, M. H., Metal-associated amyloid-β species in Alzheimer's disease. *Curr. Opin. Chem. Biol.* **2012**, *16*, 67-73.

111. Savelieff, M. G.; DeToma, A. S.; Derrick, J. S.; Lim, M. H., The Ongoing Search for Small Molecules to Study Metal-Associated Amyloid-β Species in Alzheimer's Disease. *Acc. Chem. Res.* **2014**, *47*, 2475-2482.

112. Lee, H. J.; Lee, Y. G.; Kang, J.; Yang, S. H.; Kim, J. H.; Ghisaidoobe, A. B. T.; Kang, H. J.; Lee, S.-R.; Lim, M. H.; Chung, S. J., Monitoring Metal–amyloid-β Complexation by a FRET-based Probe: Design, Detection, and Inhibitor Screening. *Chem. Sci.* **2019**, *10*, 1000-1007.

113. Granzotto, A.; Zatta, P., Metal Ions and Beta Amyloid: Conformational Modifications and Biological Aspects. In *Metal Ions in Neurological Systems*, Springer: Vienna, **2012**; Volume 142, pp 77-83.

114. Barnham, K. J.; Bush, A. I., Metals in Alzheimer's and Parkinson's Diseases. *Curr. Opin. Chem. Biol.* **2008**, *12*, 222-228.

115. Gerber, H.; Wu, F.; Dimitrov, M.; Garcia Osuna, G. M.; Fraering, P. C., Zinc and Copper Differentially Modulate Amyloid Precursor Protein Processing by γ-Secretase and Amyloid-β Peptide Production. *J. Biol. Chem.* **2017**, *292*, 3751-3767.

116. Singh, I.; Sagare, A. P.; Coma, M.; Perlmutter, D.; Gelein, R.; Bell, R. D.; Deane, R. J.; Zhong, E.; Parisi, M.; Ciszewski, J.; Kasper, R. T.; Deane, R., Low Levels of Copper Disrupt Brain Amyloid-β Homeostasis by Altering its Production and Clearance. *Proc. Natl. Acad. Sci. U.S.A.* **2013**, *110*, 14771-14776.

117. Faller, P.; Hureau, C.; La Penna, G., Metal Ions and Intrinsically Disordered Proteins and Peptides: From Cu/Zn Amyloid-β to General Principles. *Acc. Chem. Res.* **2014**, *47*, 2252-2259.

118. Gaggelli, E.; Janicka-Klos, A.; Jankowska, E.; Kozlowski, H.; Migliorini, C.; Molteni, E.; Valensin, D.; Valensin, G.; Wieczerzak, E., NMR Studies of the Zn^{2+} Interactions with Rat and Human β-Amyloid (1−28) Peptides in Water-Micelle Environment. *J. Phys. Chem. B* **2008**, *112*, 100-109.

119. Faller, P.; Hureau, C.; Berthoumieu, O., Role of Metal Ions in the Self-assembly of the Alzheimer's Amyloid-β Peptide. *Inorg. Chem.* **2013**, *52*, 12193-12206.

120. Rana, M.; Sharma, A. K., Cu and Zn Interactions with Aβ peptides: Consequence of Coordination on Aggregation and Formation of Neurotoxic Soluble Aβ Oligomers. *Metallomics* **2019**, *11*, 64-84.

121. Mold, M.; Ouro-Gnao, L.; Wieckowski, B. M.; Exley, C., Copper Prevents Amyloid-β1–42 from Forming Amyloid Fibrils under near-Physiological Conditions In Vitro. *Sci. Rep.* **2013**, *3*, 1256.

122. Zou, J.; Kajita, K.; Sugimoto, N., Cu^{2+} Inhibits the Aggregation of Amyloid β-Peptide(1–42) In vitro. *Angew. Chem. Int. Ed.* **2001**, *40*, 2274-2277.

123. Yoshiike, Y.; Tanemura, K.; Murayama, O.; Akagi, T.; Murayama, M.; Sato, S.; Sun, X.; Tanaka, N.; Takashima, A., New Insights on How Metals Disrupt Amyloid β-Aggregation and Their Effects on Amyloid-β Cytotoxicity. *J. Biol. Chem.* **2001**, *276*, 32293-32299.

124. Pedersen, J. T.; Østergaard, J.; Rozlosnik, N.; Gammelgaard, B.; Heegaard, N. H. H., Cu(II) Mediates Kinetically Distinct, Non-amyloidogenic Aggregation of Amyloid-β Peptides. *J. Biol. Chem.* **2011**, *286*, 26952-26963.

125. Ha, C.; Ryu, J.; Park, C. B., Metal Ions Differentially Influence the Aggregation and Deposition of Alzheimer's β-Amyloid on a Solid Template. *Biochemistry* **2007**, *46*, 6118-6125.

126. Garai, K.; Sengupta, P.; Sahoo, B.; Maiti, S., Selective destabilization of soluble amyloid β oligomers by divalent metal ions. *Biochem. Biophys. Res. Commun.* **2006**, *345*, 210-215.

127. Bolognin, S.; Messori, L.; Drago, D.; Gabbiani, C.; Cendron, L.; Zatta, P., Aluminum, Copper, Iron and Zinc Differentially Alter Amyloid-Aβ1–42 Aggregation and Toxicity. *Int. J. Biochem. Cell Biol.* **2011**, *43*, 877-885.

128. Matheou, C. J.; Younan, N. D.; Viles, J. H., Cu^{2+} Accentuates Distinct Misfolding of $Aβ_{(1–40)}$ and $Aβ_{(1–42)}$ Peptides, and Potentiates Membrane Disruption. *Biochem. J.* **2015**, *466*, 233-242.

129. Kepp, K. P., Alzheimer's Disease: How Metal Ions Define β-amyloid Function. *Coord. Chem. Rev.* **2017**, *351*, 127-159.

130. House, E.; Mold, M.; Collingwood, J.; Baldwin, A.; Goodwin, S.; Exley, C., Copper Abolishes the β-sheet Secondary Structure of Preformed Amyloid Fibrils of Amyloid-β 42. *J. Alzheimers Dis.* **2009**, *18*, 811-817.

131. Sharma, A. K.; Pavlova, S. T.; Kim, J.; Kim, J.; Mirica, L. M., The Effect of Cu^{2+} and Zn^{2+} on the Aβ 42 Peptide Aggregation and Cellular Toxicity. *Metallomics* **2013**, *5*, 1529-1536.

132. Pedersen, J. T.; Chen, S. W.; Borg, C. B.; Ness, S.; Bahl, J. M.; Heegaard, N. H. H.; Dobson, C. M.; Hemmingsen, L.; Cremades, N.; Teilum, K., Amyloid-β and α-Synuclein Decrease the Level of Metal-Catalyzed Reactive Oxygen Species by Radical Scavenging and Redox Silencing. *J. Am. Chem. Soc.* **2016**, *138*, 3966-3969.

133. Barnham, K. J.; Haeffner, F.; Ciccotosto, G. D.; Curtain, C. C.; Tew, D.; Mavros, C.; Beyreuther, K.; Carrington, D.; Masters, C. L.; Cherny, R. A., Tyrosine Gated Electron Transfer is Key to the Toxic Mechanism of Alzheimer's Disease β-amyloid. *FASEB J.* **2004**, *18*, 1427-1429.

134. House, E.; Collingwood, J.; Khan, A.; Korchazkina, O.; Berthon, G.; Exley, C., Aluminium, Iron, Zinc and Copper Onfluence the In Vitro Formation of Amyloid Fibrils of Aβ 42 in a Manner which may have Consequences for Metal Chelation Therapy in Alzheimer's Disease. *J. Alzheimers Dis.* **2004**, *6*, 291-301.

135. Branch, T.; Barahona, M.; Dodson, C. A.; Ying, L., Kinetic Analysis Reveals the Identity of Aβ-Metal Complex Responsible for the Initial Aggregation of Aβ in the Synapse. *ACS Chem. Neurosci.* **2017**, *8*, 1970-1979.

136. Huang, X.; Atwood, C. S.; Hartshorn, M. A.; Multhaup, G.; Goldstein, L. E.; Scarpa, R. C.; Cuajungco, M. P.; Gray, D. N.; Lim, J.; Moir, R. D.; Tanzi, R. E.; Bush, A. I., The Aβ Peptide of Alzheimer's Disease Directly Produces Hydrogen Peroxide through Metal Ion Reduction. *Biochemistry* **1999**, *38*, 7609-7616.

137. Huang, X.; Cuajungco, M. P.; Atwood, C. S.; Hartshorn, M. A.; Tyndall, J. D. A.; Hanson, G. R.; Stokes, K. C.; Leopold, M.; Multhaup, G.; Goldstein, L. E.; Scarpa, R. C.; Saunders, A. J.; Lim, J.; Moir, R. D.; Glabe, C.; Bowden, E. F.; Masters, C. L.; Fairlie, D. P.; Tanzi, R. E.; Bush, A. I., Cu(II) Potentiation of Alzheimer Aβ Neurotoxicity: Correlation with Cell-free Hydrogen Peroxide Production and Metal Reduction. *J. Biol. Chem.* **1999**, *274*, 37111-37116.

138. Stohs, S. J.; Bagchi, D., Oxidative Mechanisms in the Toxicity of Metal Ions. *Free Radic. Biol. Med.* **1995**, *18*, 321-336.

139. Hureau, C.; Balland, V.; Coppel, Y.; Solari, P. L.; Fonda, E.; Faller, P., Importance of Dynamical Processes in the Coordination Chemistry and Redox Conversion of Copper Amyloid-β Complexes. *J. Biol. Inorg. Chem.* **2009**, *14*, 995-1000.

140. Dikalov, S. I.; Vitek, M. P.; Mason, R. P., Cupric–amyloid β Peptide Complex Stimulates Oxidation of Ascorbate and Generation of Hydroxyl Radical. *Free Radic. Biol. Med.* **2004**, *36*, 340-347.
141. Rice, M. E., Ascorbate Regulation and its Neuroprotective Role in the Brain. *Trends Neurosci.* **2000**, *23*, 209-216.

Chapter 2

Orobol: An Isoflavone Exhibiting Regulatory Multifunctionality against Four Pathological Features of Alzheimer's Disease
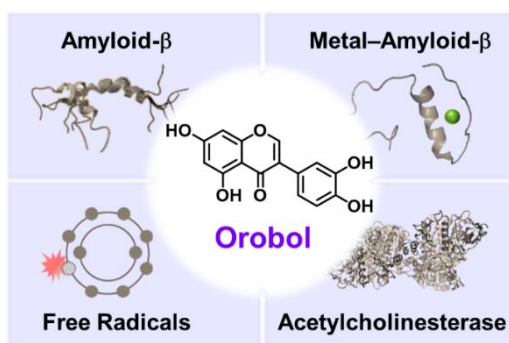
The results and discussion presented in this chapter were reported in the publication [Nam, G.;[†] Ji, Y.;[†] Lee, H. J.;[†] Kang, J.; Yi, Y.; Kim, M.; Lin, Y.; Lee, Y.-H.; Lim, M. H. *ACS Chem. Neurosci.* **2019**, *10*, 3386–3390 ([†]equal contribution)]. Yonghwan Ji synthesized **orobol** and carried out biochemical assays. Dr. Hyuck Jin Lee performed gel/Western blot, TEM, and mass spectrometric experiments. Dr. Juhye Kang provided helpful discussion and guidance for the synthesis of **orobol**. Yelim Yi and Mingeun Kim contributed helpful discussions. Dr. Yuxi Lin and Professor Young-Ho Lee carried out the studies of 2D HMQC NMR. I was involved in the synthesis of **orobol**, the studies by gel/Western blot and mass spectrometry with data analysis, and writing the manuscript with Dr. Hyuck Jin Lee under the supervision of Professor Mi Hee Lim.

2.1. Introduction

Most dementia cases are diagnosed as the progress neurodegenerative disease AD, which presents a pessimistic outlook based on the lack of a cure and aging world population.[1,2] Despite efforts of investigating AD pathology, our comprehension on the subject matter remains fragmental. Numerous pathological factors of AD have been implicated as contributors towards the clinical cognitive decline, however, the principal causative factors of the disease remain unidentified.[1] This fact is practically demonstrated by the clinical failures of drugs formulated based on the individual pathogenic targets [*i.e.*, Aβ, metal ions, free radicals, and AChE]. In response, resesarchers began looking in to the malignant connections among these pathogenic elements of AD.[1] For example, the close association between Aβ and metal ions [*e.g.*, Cu(II) and Zn(II)] have led to the introduction of metal–Aβ as a hybrid pathogenic component in AD.[3-5] Endeavors to identify the evaluate such pathogenic connections in AD are hindered by experimental challenges that arise from the complexity involving multiple intricate biological components under physiologically relevant conditions. Chemical tools with the ability to target multiple pathogenic elements of AD could significantly expedite our efforts to elucidate the relationships between them. In this chapter, we present a naturally occurring isoflavone, **orobol** (**Oro**), as a multifunctional molecule with the capacity to (i) alter the aggregation pathways of metal-free $A\beta_{42}$ and metal–$A\beta_{42}$, (ii) scavenge organic free radicals, and (iii) inhibit the catalytic activity of AChE. Although numerous compounds have been tested as multifunctional chemicals, reports of flavonoids capable of regulating four or more pathological factors found in AD are very limited.

2.2. Results and discussion

2.2.1. Rational selection of orobol (Oro)

In this study, we report, for the first time, a multifunctional isoflavone (**Oro**, Figure 2.1) capable of modulating four pathogenic elements of AD (*i.e.*, metal-free Aβ, metal–Aβ, free radicals, and AChE). **Oro** is characterized by an isoflavone framework with structural variations from the basic flavone backbone (Figure 2.1 and Scheme 2.1): (i) four hydroxyl substituents; (ii) catechol functionality on the B-ring; (iii) translocation of the B-ring. The molecular structure of **Oro** foreshadows its potential versatility in modulating our target subjects. First, oxidation of "catechol-type flavonoids" is reported to produce an ortho-quinone that covalently binds to primary amine-containing residues of Aβ (*e.g.*, K16 and K28).[6] Previous research regarding synthetic aminoisoflavones demonstrated the pertinence of both the catechol functionality and isoflavone framework towards their ability to modify the aggregation of Aβ.[7] Two potential metal chelation sites of **Oro** (*i.e.*, 3'-OH/4'-OH and 4-oxo/5-OH) indicate the molecule's ability to bind to metal ions by forming 5- or 6-membered rings.[7,8] The B-ring catechol moiety has been reported as a source of antioxidant activity fostered by
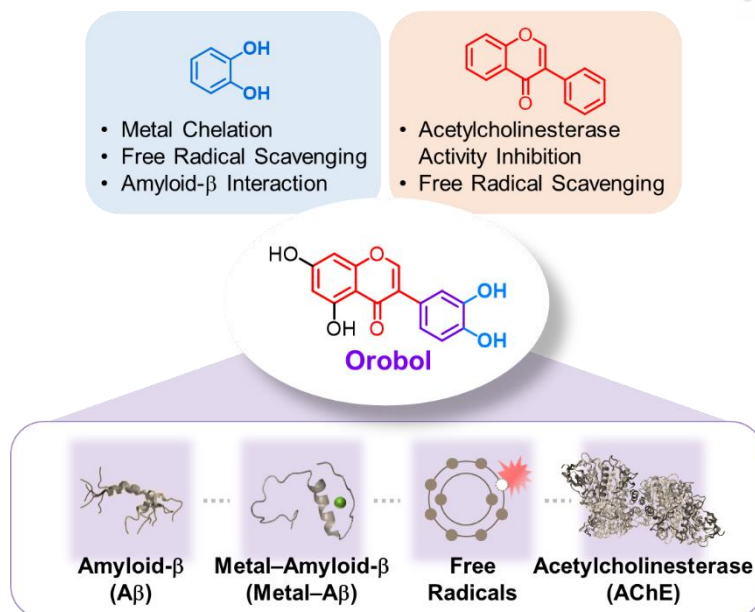
Figure 2.1. Rational identification of **Oro** as a multifunctional small molecule for regulating four pathological factors implicated in AD (*i.e.*, metal-free Aβ, metal–Aβ, free radicals, and AChE).

its radical stabilization capabilities *via* intramolecular hydrogen bonding.[9,10] Although there are no reports of **Oro**'s effect against AChE, structure-activity relationship studies of flavonoids' ability to suppress the activity of AChE indicate the inhibitory potency of isoflavones and the significance of the catechol functional group.[11] Despite the collective implications for the versatility of **Oro** from previous studies, the multifunctionality of the compound against four pathological factors linked to AD pathology (*i.e.*, metal-free Aβ, metal–Aβ, free radicals, and AChE) has not been directly examined until now.

2.2.2. Synthesis of orobol (Oro)

Scheme 2.1. Synthetic routes to **orobol (O-ro)**.
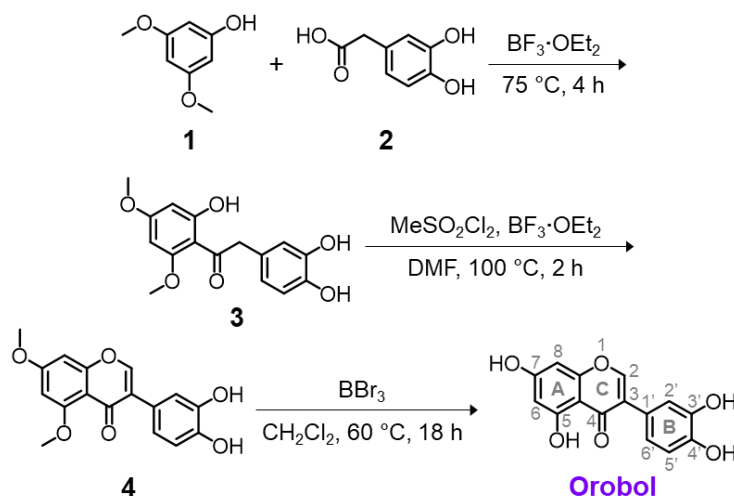
Oro was prepared following previously reported procedures with minor modifications as shown in Scheme 2.1.[12,13] An electrophilic aromatic substitution reaction (Friedel-crafts acylation) of **1** with **2**

generated **3** (17% yield) using boron trifluoride ethyl etherate (BF$_3$·OEt$_2$) as both the solvent and catalyst.[14] The subsequent cyclization of **3** in the presence of methanesulfonyl chloride (MeSO$_2$Cl$_2$) generated **4** in 19% yield. Lastly, the demethylation of **4** with boron tribromide (BBr$_3$) afforded **Oro** (10% yield).[13]

2.2.3. Modulative reactivity towards metal-free Aβ$_{42}$ and metal–Aβ$_{42}$ aggregation

Oro's effects on the aggregation pathways of metal-free Aβ$_{42}$ and metal–Aβ$_{42}$ were first determined through gel electrophoresis with Western blotting (gel/Western blot) in both inhibition (inhibition of Aβ$_{42}$ aggregate formation; Figure 2.2a) and disaggregation (disassembly and/or aggregation of preformed Aβ$_{42}$ aggregates; Figure 2.3a) experiments. In the inhibition experiments, **Oro** noticeably altered the molecular weight (MW) distribution of metal-free Aβ$_{42}$ species by increasing the intensity of smearing bands greater than *ca.* 20 kDa compared to **Oro**-free Aβ$_{42}$ (Figure 2.2b; left). Cu(II)–Aβ$_{42}$

Figure 2.2. Influence of **orobol** on the formation of metal-free and metal-induced Aβ$_{42}$ aggregates. (a) Scheme of the inhibition experiment. (b) Analysis of the MW distribution of the resultant Aβ$_{42}$ species by gel/Western blot using an anti-Aβ antibody (6E10). (c) TEM images of the samples from (b). Conditions: [Aβ$_{42}$] = 25 μM; [CuCl$_2$ or ZnCl$_2$] = 25 μM; [**orobol**] = 50 μM; 20 mM HEPES, pH 7.4 [for metal-free and Zn(II)-containing samples] or pH 6.6 [for Cu(II)-added samples], 150 mM NaCl; 37 °C; 24 h incubation; constant agitation.

treated with **Oro** exhibited darker bands at *ca.* 20-240 kDa and less intense bands at *ca.* 7-20 kDa, relative to Cu(II)–Aβ$_{42}$ without treatment of the compound. In the presence of Zn(II), **Oro** enhanced the band intensity at *ca.* 7-100 kDa. In addition to the inhibition studies, the disaggregation experiments illustrated the reactivity of **Oro** towards preformed aggregates of metal-free Aβ$_{42}$ and metal–Aβ$_{42}$ (Figure 2.3). Under metal-free conditions, when preformed Aβ$_{42}$ aggregates were incubated with **Oro**, a different MW distribution from **Oro**-free Aβ$_{42}$ aggregates with darker bands at *ca.* 50-240 kDa was observed (Figure 2.3b). **Oro** noticeably reduced the band intensity of preformed Cu(II)–Aβ$_{42}$ aggregates smaller than at *ca.* 100 kDa. As for Zn(II)–Aβ$_{42}$, the MW distribution of preformed species was altered by **Oro** with an increase in the intensity of the smearing band at *ca.* 20-50 kDa. It should be noted that the Aβ$_{42}$ aggregate species detected through gel/Western blot are small enough to enter the gel matrix. In order to visualize the larger Aβ$_{42}$ assemblies, transmission electron microscopy (TEM) was used to examine the morphology of the resultant metal-free Aβ$_{42}$ and metal–Aβ$_{42}$ aggregates from the

Figure 2.3. Influence of **orobol** on the disassembly and/or aggregation of preformed metal-free and metal-associated Aβ$_{42}$ aggregates. (a) Scheme of the disaggregation experiment. (b) Analysis of the molecular weight distribution of the resultant Aβ$_{42}$ species by gel/Western blot with an anti- Aβ antibody (6E10). (c) TEM images of the samples from (b). Conditions: [Aβ$_{42}$] = 25 μM; [CuCl$_2$ or ZnCl$_2$] = 25 μM; [**orobol**] = 50 μM; 20 mM HEPES, pH 7.4 [for metal-free and Zn(II)-containing samples] or pH 6.6 [for Cu(II)-added samples], 150 mM NaCl; 37 °C; 24 h incubation; constant agitation.

gel/Western blot experiments (Figures 2.2c and 2.3c). According to the TEM images, **Oro** noticeably modified the morphology of metal-free Aβ_{42} and metal–Aβ_{42} assemblies from both the inhibition and disaggregation experiments, inducing the formation of smaller chopped fibrils or amorphous aggregates. Overall, the gel/Western blot and TEM results support **Oro**'s modulative reactivity towards the aggregation of both metal-free and metal-bound Aβ_{42} species.

To elucidate the mechanistic details regarding **Oro**'s ability to modulate the aggregation pathways of metal-free Aβ_{42} and metal–Aβ_{42}, spectrometric and spectroscopic studies [*i.e.*, electrospray ionization mass spectrometry (ESI-MS), tandem MS (ESI-MS^2), and UV–Visible spectroscopy (UV–Vis)] were performed to determine the interactions of **Oro** with metal-free Aβ_{42}, Cu(II), and Cu(II)–Aβ_{42} (Figures 2.4 and 2.5). Under metal-free conditions, a 2Aβ_{42}–**Oro** complex was detected (Figure 2.4a; purple). The complexation of **Oro** with Aβ_{42} dimer was observed to vary the size distribution of the peptide dimer indicating a structural compaction, according to the ion mobility-mass spectrometry (IM-MS) data (Figure 2.4b; purple). Such changes could be responsible for the altered aggregation pathways of Aβ_{42}.[8,15]

Interactions between Cu(II) and **Oro** was confirmed *via* UV–Vis denoted by notable optical changes with the addition of Cu(II) to an aqueous solution of the isoflavone (Figure 2.5a). Under Cu(II)-present conditions, the mass spectrometric analysis of **Oro**-treated Aβ_{42} led to the detection of singly oxidized Aβ_{42} (Figure 2.5b; red circle). The oxidation-induced conformational change of Aβ_{42} monomer was monitored by IM-MS (Figure 2.5c), in which the singly oxidized Aβ_{42} exhibited a more compact structure. Using ESI-MS^2, the oxidation sites of Aβ_{42} were determined by analyzing the peptide

Figure 2.4. Interactions of **Oro** with metal-free Aβ_{42}. (a) Interaction of **Oro** with soluble metal-free Aβ_{42}, monitored by ESI-MS. Inset: Zoom-in spectrum from 1860 to 1880 *m/z* (indication of [2Aβ_{42} + **Oro**]$^{5+}$ at 1863 *m/z*). (b) Analysis of the IM-MS spectra of [2Aβ_{42}]$^{5+}$ (black) and [2Aβ_{42} + **Oro**]$^{5+}$ (purple). Conditions: [Aβ_{42}] = 20 μM; [**Oro**] = 100 μM; 100 mM ammonium acetate, pH 7.4; 3 h incubation; no agitation.

Figure 2.5. Interactions of **Oro** with Cu(II) and Cu(II)−Aβ$_{42}$. (a) Cu(II) binding of **Oro** in a buffered solution. UV−Vis spectra of **Oro** (black) with up to 5 equiv of Cu(II) (blue). Conditions: [**Oro**] = 25 μM; [CuCl$_2$] = 0, 12.5, 25, 50, and 125 μM; pH 7.4; room temperature. Interaction of **Oro** with soluble Cu(II)−Aβ$_{42}$, monitored by (b) ESI-MS and (c) IM-MS. (d) Tandem mass spectrometric analysis in conjunction with CID of the singly oxidized Aβ$_{42}$ (1511 *m/z*). Conditions: [Aβ$_{42}$] = 20 μM; [CuCl$_2$] = 20 μM; [**Oro**] = 100 μM; 100 mM ammonium acetate, pH 7.4; 3 h incubation; no agitation.

fractions of the singly oxidized Aβ$_{42}$, reported as *b* fragments (Figure 2.5d). Upon collision-induced dissociation (CID) of [Aβ$_{42}$ + O]$^{3+}$ at 1511 *m/z*, Aβ fragments were found in their oxidized form from b_{14}, revealing H14 as a possible oxidation site. Based on the indication of a mixture containing both the oxidized and non-oxidized fragments from b_{14} to b_{34} and the sole detection of the oxidized Aβ fragments starting from b_{35}, M35 was designated as another plausible oxidation site of Aβ. A noteworthy observation was that **Oro** noticeably diminished the peak intensity of Cu(II)–Aβ$_{42}$ while increasing that of metal-free Aβ$_{42}$ (Figure 2.5b), indicating that the isoflavone may disrupt the interaction between Aβ$_{42}$ and Cu(II), potentially through Cu(II) chelation.[7] Together, our spectrometric and spectroscopic studies of **Oro** demonstrate its ability to (i) interact with metal-free Aβ$_{42}$ and Cu(II), (ii) disrupt the interaction

29

between Cu(II) and $A\beta_{42}$, and (iii) oxidize $A\beta_{42}$ in the presence of Cu(II) at H14 or M35. Such molecular interactions and alterations of $A\beta$ have previously been reported as mechanistic strategies to modify the aggregation pathways of $A\beta_{42}$ in both the absence and presence of metal ions.[16-19] Note that Zn(II)–$A\beta_{42}$ could not be detected under our experimental conditions for ESI-MS studies.

2.3. Inhibitory activities against organic free radicals and acetylcholinesterase (AChE)

The free radical scavenging activity of **Oro** was determined relative to Trolox, a vitamin E analog with notable antioxidant activity, using the Trolox equivalent antioxidant capacity (TEAC) assay (Figure 2.6a).[14] **Oro** was observed to significantly scavenge free radicals with a TEAC value of 3.39 ($\pm$ 0.14). Moreover, **Oro**'s inhibitory activity against AChE was measured by a fluorometric AChE assay,[20] indicating a nanomolar IC_{50} value [123 ($\pm$ 32) nM; Figure 2.6a]. *In silico* studies (Figures 2.6b and 2.6c) presented that **Oro** could interact with multiple amino acid residues lining the active site gorge (*e.g.*, G120, Y124, F295, Y337, and Y341). In addition, **Oro** was shown to interact with S203 of the catalytic triad, responsible for initiating the enzymatic hydrolysis of ACh,[21] *via* hydrogen bonding, suggesting a potential mechanism for **Oro**'s inhibitory activity against AChE.
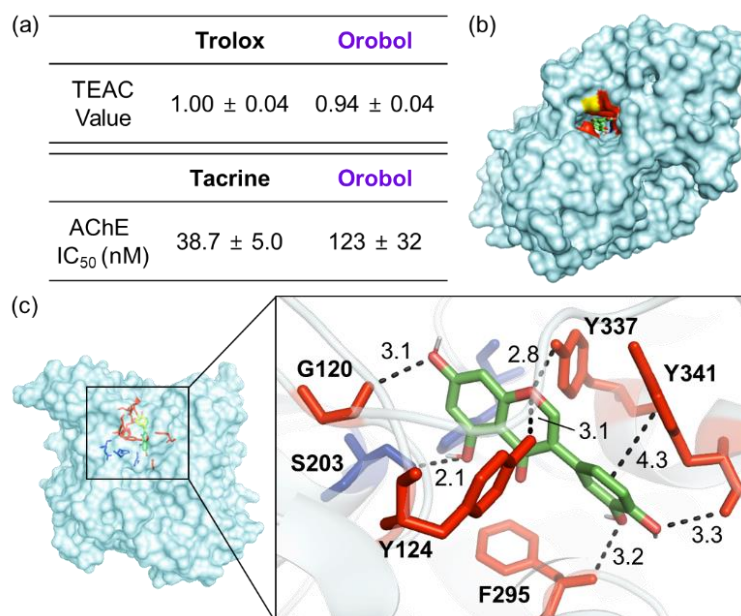
Figure 2.6. Free radical scavenging and AChE inhibitory activities of **Oro**. (a) TEAC values and IC_{50} values against AChE activity of **Oro** and the corresponding standards (Trolox: antioxidant; Tacrine: AChE inhibitor).[20] (b,c) Docking studies of **Oro** and AChE (PDB 1C2B[21]). (b) Top view perspective looking into the active site gorge of AChE. (c) Side view of **Oro** bound to AChE and zoom-in image of the interaction between **Oro** and the amino acid residues of the active site gorge. The dashed lines and the corresponding numbers indicate the possible hydrogen bonding between **Oro** and AChE and their predicted distances (Å).

2.4. Conclusions

Oro, a naturally occurring isoflavone, is demonstrated as a multifunctional small molecule able to modulate four distinct pathological features found in the brains affected by AD (*i.e.*, metal-free and metal-induced Aβ aggregation, oxidative stress, and AChE-catalyzed ACh hydrolysis). Aside from the properties tested herein, additional neuroprotective properties of **Oro** have been previously reported: (i) protection against 6-hydroxydopamine-induced neurotoxicity by restoring proteasomal function;[22] (ii) anti-inflammatory effects;[23] (iii) inhibition of tyrosine-specific protein kinase;[24] phosphatidylinositol turnover;[25] and 15-lipoxygenase;[26] (iv) hypotensive effects.[27] Based on its functional versatility, the isoflavone framework of **Oro** conferring multifunctionality could be useful towards developing chemical reagents for advancing our understanding of the multi-faceted pathology of neurodegenerative disorders, including AD.

2.5. Experimental section

2.5.1. Materials and methods

All reagents were purchased from commercial suppliers and used as received unless noted otherwise. NMR and high-resolution mass spectrometric analyses of small molecules were conducted on an Agilent 400-MR DD2 NMR spectrometer (UNIST Central Research Facilities, Ulsan, Republic of Korea) and a Q exactive plus orbitrap mass spectrometer (HRMS; Thermo Fisher Scientific, Waltham, MA, USA), respectively. Absorbance and fluorescence values for biological assays were measured on a Molecular Devices SpectraMax M5e microplate reader (Sunnyvale, CA, USA). Trace metal contamination was removed from buffers and solutions used in metal binding and $Aβ_{42}$ experiments by treating with Chelex overnight (Sigma-Aldrich, St. Louis, MO, USA). Optical spectra were recorded on an Agilent 8453 UV−Vis spectrometer. $Aβ_{42}$ (DAEFRHDSGYEVHHQKLVFFAEDVGSNKGAI-IGLMVGGVVIA) was purchased from AnaSpec (Fremont, CA, USA) and Peptide Institute (Osaka, Japan). AChE assay kit was purchased from Abcam (Cambridge, UK). Double-distilled H_2O (ddH_2O) was obtained from a Milli-Q Direct 16 system (18.2 MΩ·cm; Merck KGaA, Darmstadt, Germany). Transmission electron microscopical images were taken using a Tecnai F30 (FEI) transmission electron microscope (KAIST Analysis Center for Research Advancement, Daejeon, Republic of Korea).

2.5.2. Synthesis of orobol (Oro)

Synthesis of 3 [3-(3,4-dihydroxyphenyl)-5,7-trimethoxy-4*H*-chromen-4-one] A solution (BF_3·OEt_2, 15 mL) of 3,4-dihydroxyphenylacetic acid (1.5 g, 9.1 mmol) and 3,5-dimethoxyphenol (1.4 g, 9.1 mmol) was refluxed at 75 °C. After 4 h, the reaction mixture was extracted in a solution of ethyl acetate (EtOAc) and saturated sodium acetate (NaOAc) (12 g/100 mL). The organic layer was collected, washed with brine, dried with $MgSO_4$, filtered, and concentrated. The crude product was purified *via* column chromatography (SiO2, 1:1 EtOAc/hexanes, R_f = 0.4; > 90% purity) to yield **3** (yellow oil; 459 mg, 1.5

mmol, 17% yield). ^{1}H NMR [400 MHz, $(CD_3)_2CO$, δ (ppm)]: 13.89 (1H, s), 7.75 (2H, br), 6.75 (2H, dd, J = 8.3, 1.7 Hz), 6.60 (1H, d, J = 8.0 Hz), 6.07 (2H, dd, J = 9.1, 2.0 Hz), 4.18 (2H, s), 3.94 (3H, d, J = 1.9 Hz), 3.86 (3H, d, J = 1.9 Hz). ^{13}C NMR [100 MHz, $(CD_3)_2CO$, δ (ppm)]: 203.5, 167.8, 166.5, 162.9, 144.8, 144.7, 127.3, 120.9, 116.5, 115.0, 105.2, 93.7, 90.6, 55.3, 55.2, 49.1. HRMS: $[M + Na]^+$ calcd, 327.0847; found, 327.0844.

Synthesis of 4 [3-(3,4-dihydroxyphenyl)-5,7-dimethoxy-4H-chromen-4-one] 3 (459 mg, 1.5 mmol) was dissolved in dried N,N-dimethylformamide (DMF, 6 mL) and $BF_3 \cdot OEt_2$ (1.07 mL, 15 mmol) was added dropwise and heated to 50 °C for 1 h followed by the introduction of $MeSO_2Cl$ [173 μL, 1.5 mmol, DMF (2 mL)] dropwise. The reaction mixture was refluxed at 100 °C for 2 h. After the reaction, the mixture was extracted in a solution of EtOAc and saturated NaOAc (12 g/100 mL). The organic layer was collected, washed with brine, dried with $MgSO_4$, filtered, and concentrated. The crude product was purified by column chromatography (SiO_2, 3:1 EtOAc/hexanes, R_f = 0.4). **4** (white powder) was obtained by washing the solid with CH_3OH. (88 mg, 0.28 mmol, 19% yield). ^{1}H NMR [400 MHz, $(CD_3)_2SO$, δ (ppm)]: 9.02 (1H, s), 8.96 (1H, s), 8.15 (1H, s), 7.00 (1H, s), 6.79 (2H, s), 6.69 (1H, d, J = 2.1 Hz), 6.54 (1H, d, J = 2.1 Hz), 3.92 (3H, s), 3.87 (3H, s). ^{13}C NMR [100 MHz, $(CD_3)_2SO$, δ (ppm)]: 174.3, 164.0, 161.3, 159.6, 151.0, 145.6, 145.2, 125.5, 123.6, 120.4, 117.2, 115.6, 109.4, 96.6, 93.3, 56.6, 56.4. HRMS: $[M – H]^-$ calcd, 313.0712; found, 313.0721.

Synthesis of Oro [3-(3,4-Dihydroxyphenyl)-5,7-dihydroxy-4H-chromen-4-one] A solution (dry CH_2Cl_2) of **4** (87.2 mg, 0.28 mmol) was stirred in an ice bath. A solution of BBr_3 in CH_2Cl_2 (1 M, 250 μL) was added to the solution of **4** dropwise. Then the ice-bath was removed to stir the reaction mixture at 60 °C for 18 h. The reaction mixture was refluxed at 100 °C for 2 h. After the reaction, the mixture was extracted with EtOAc and water. The organic layer was collected, washed with brine, dried with $MgSO_4$, filtered, and concentrated. The crude was purified by column chromatography (SiO_2, 1:30 CH_3OH/CH_2Cl_2, R_f = 0.2). The final product, **Oro** (pale yellow powder), was obtained by recrystallization using a mixture of acetone, hexanes, and CH_2Cl_2. ^{1}H NMR [400 MHz, $(CD_3)_2CO$, δ (ppm)]: 13.07 (1H, s), 8.41 (2H, br), 8.16 (1H, s), 7.16 (1H, d, J = 2.0 Hz), 6.95 (1H, dd, J = 8.2, 2.1 Hz), 6.89 (1H, d, J = 8.2 Hz), 6.43 (1H, d, J = 2.2 Hz), 6.29 (1H, d, J = 2.2 Hz). ^{13}C NMR [100 MHz, $(CD_3)_2CO$, δ (ppm)]: 180.9, 164.2, 163.2, 159.2, 153.6, 145.5, 144.8, 123.2, 122.8, 120.6, 116.5, 115.0, 105.4, 98.9, 93.7. HRMS: $[M – H]^-$ calcd, 285.0397; found, 285.0405.

2.5.3. Aβ$_{42}$ aggregation experiments

All experiments were carried out following previously published procedures.[28] Initially, Aβ$_{42}$ was dissolved in ammonium hydroxide (NH_4OH, 1% v/v, aq), aliquoted, lyophilized overnight, and stored

at -80 °C. The stock solution of Aβ_{42} was prepared by dissolving the lyophilized Aβ_{42} in NH$_4$OH (1% v/v; 10 μL) and diluting it with ddH$_2$O. The concentration of Aβ_{42} was determined by measuring the absorbance of the solution at 280 nm ($\varepsilon = 1490$ M^{-1}cm^{-1}). The peptide stock solution was diluted to a final concentration of 25 μM in a Chelex-treated buffered solution [20 mM 4-(2-hydroxyethyl)-1-piperazineethanesulfonic acid (HEPES), pH 7.4 (for metal-free and Zn(II) samples) or pH 6.6 (for Cu(II) samples), 150 mM NaCl]. In the inhibition experiments, **Oro** [final concentration, 50 μM; 1% v/v dimethyl sulfoxide (DMSO)] was added to the freshly prepared samples of Aβ_{42} (25 μM) in the absence and presence of a metal chloride salt (CuCl$_2$ or ZnCl$_2$; 25 μM) followed by incubation for 24 h at 37 °C with constant agitation. For the disaggregation experiments, Aβ_{42} (25 μM) was pre-incubated for 24 h at 37 °C with constant agitation in the absence and presence of CuCl$_2$ or ZnCl$_2$ (25 μM). The pre-incubated samples were then treated with **Oro** (final concentration, 50 μM; 1% v/v DMSO) and incubated for an additional 24 h at 37 °C with constant agitation.

2.5.4. Gel/Western blot

Size distributions of the incubated Aβ_{42} samples were analyzed by gel/Western blot using an anti-Aβ antibody (6E10). 10 μL of each sample was separated on a 10-20% Tris-tricine gel (Thermo Fisher Scientific, Carlsbad, CA, USA). After separation, the peptides were transferred onto a nitrocellulose membrane and blocked with bovine serum albumin (BSA, 3% w/v, RMBIO, Missoula, MT, USA) in Tris-buffered saline (TBS) containing 0.1% Tween-20 (TBS-T) for 2 h at room temperature. Then, the membranes were incubated with an anti-Aβ antibody (6E10) (1:2,000; Covance, Princeton, NJ, USA) in a solution of 2% BSA (w/v in TBS-T) overnight at 4 ºC. The membranes were then washed with TBS-T three times for 10 min each and incubated with a horseradish peroxidase-conjugated goat antimouse secondary antibody (1:5,000) in 2% BSA for 1 h at room temperature. The membranes were visualized on a ChemiDoc MP Imaging System (Bio-Rad, Hercules, CA, USA) using a homemade ECL kit.[29]

2.5.5. TEM

Samples for TEM measurements were prepared based on previously published methods.[30] Glow-discharged grids (Formvar/Carbon 300-mesh, Electron Microscopy Sciences, Hatfield, PA, USA) were treated with Aβ samples for 2 min at room temperature. Excess sample was removed using filter paper. Each grid was washed three times with ddH$_2$O and incubated with uranyl acetate (1% w/v ddH$_2$O, 5 μL) for 1 min. After removing excess uranyl acetate, the grids were dried for at least 20 min at room temperature. Images of each grid were taken on a Tecnai F30 (FEI) transmission electron microscope (200 kV; 29,000x magnification).

2.5.6. Cu(II)-binding studies

The interaction of **Oro** with Cu(II) was monitored by UV–Vis spectroscopy. UV–Vis experiments were carried out in a Chelex-treated buffered solution (20 mM HEPES, pH 7.4, 150 mM NaCl). The solution of **Oro** was titrated up to 5 equiv of $CuCl_2$ at room temperature. The mixture solution was allowed to equilibrate for 5 min after the addition of $CuCl_2$ at room temperature before the spectra were recorded.

2.5.7. Mass spectrometric analyses

Experiments were carried out following previously reported procedures.[31-33] $A\beta_{42}$ (20 μM) was incubated with **Oro** (100 μM; 1% v/v DMSO) and/or $CuCl_2$ (20 μM) in 100 mM ammonium acetate, pH 7.2 at 37 °C without agitation. The incubated samples were then diluted by five-fold with ddH_2O and injected into the mass spectrometer. A Waters Synapt G2-Si quadrupole time-of-flight (Q-Tof) ion mobility mass spectrometer (Waters, Manchester, UK) equipped with an ESI source [DGIST Center for Core Research Facilities (CCRF)] was used for the experiments. The capillary voltage, sampling cone voltage, and source temperature were set to 2.8 kV, 70 V, and 40 °C, respectively. The backing pressure was adjusted to 2.7 mbar. Ion mobility wave height and velocity were adjusted to 10 V and 300 m/s, respectively, and gas flows for the helium and ion mobility cell were set to 120 and 30 mL/min, respectively. ESI-MS^2 analyses were additionally performed on the singly oxidized $A\beta_{42}$. The ESI parameters and experimental conditions were the same as above. Collision-induced dissociation was conducted by applying collision energy in the trap.

2.5.8. TEAC assay

The free radical scavenging capacity of **Oro** was determined by the TEAC assay based on the decolorization of ABTS [2,2'-azino-bis(3-ethylbenzothiazoline-6-sulfonic acid)diammonium salt] cation radicals in comparison to that of the vitamin E analog, Trolox, known for its antioxidant properties.[34] Previously reported procedures were followed with minor modifications.[28] Blue $ABTS^{•+}$ cation radicals were generated by dissolving ABTS (7.0 mM) with potassium persulfate (2.5 mM) in ddH_2O (5 mL) and incubating the solution for 16 h at room temperature in the dark. Then the solution was diluted with ethanol to an absorbance of *ca.* 0.7 at 734 nm. The $ABTS^{•+}$ solution (200 μL) was then added to a clear 96 well plate and incubated for 5 min at 25 ºC. Various concentrations of **Oro** or Trolox were added to the 96 well plate and incubated at 25 ºC for multiple time periods (1, 3, 6, and 10 min). Percent inhibition was calculated based on the measured absorbance at 734 nm [% inhibition = 100 x $(A_0 - A)/A_0$; A_0 = absorbance of the control well without compound; A = absorbance of the wells treated with compounds] and plotted as a function of compound concentration. The TEAC values of each time point were calculated as the ratios between the slope of **Oro** and the slope of Trolox. All measurements were carried out in triplicate.

2.5.9. AChE activity assay

AChE inhibitory activities of **Oro** was determined using a fluorometric AChE assay kit (Abcam, Cambridge, MA, USA) following the manufacturer's protocol with slight modifications. *ee*AChE was dissolved and diluted to a working solution of 400 mU/mL. The *ee*AChE solution (50 µL) was added to a 96 well plate. Various concentrations of **Oro** were then added to the 96 well plate. After shaking, the mixture of *ee*AChE and **Oro** was pre-incubated for 15 min. A reaction mixture containing ACh, an AChE probe, and AbRed^{TM} was added to the 96 well plate to initiate the reaction. Calculations of the AChE activity were made based on the fluorescence intensity ($\lambda_{ex}/\lambda_{em}$ = 540/590 nm) of the wells detected after 15 min. Data was normalized to the control (no inhibitor). All experiments were performed in duplicate.

2.5.10. Docking studies

Flexible ligand docking studies for **Oro** against *Electrophorus electricus* acetylcholinesterase (*ee*AChE; PDB 1C2B)[21] using AutoDock Vina.[35] The MMFF94 energy minimization in ChemBio3D Ultra 11.0 was used to optimize the ligand structure for docking studies. The structural files of **Oro** and the protein were generated by AutoDock Tools and imported into PyRx, which were used to run AutoDock Vina. The search space dimensions were set to contain the catalytic active site (CAS) and peripheral anionic site (PAS) for AChE (PDB 1C2B). The exhaustiveness for the docking runs was set to 1024. Docked poses of the ligand with *ee*AChE were visualized using Pymol.

2.6. Acknowledgments

2.7. References

1. Savelieff, M. G.; Nam, G.; Kang, J.; Lee, H. J.; Lee, M.; Lim, M. H., Development of Multifunctional Molecules as Potential Therapeutic Candidates for Alzheimer's Disease, Parkinson's Disease, and Amyotrophic Lateral Sclerosis in the Last Decade. *Chem. Rev.* **2019**, *119*, 1221-1322.
2. Mullard, A., Alzheimer Amyloid Hypothesis Lives On. *Nat. Rev. Drug Discov.* **2017**, *16*, 3-5.
3. Faller, P.; Hureau, C.; La Penna, G., Metal Ions and Intrinsically Disordered Proteins and Peptides: From Cu/Zn Amyloid-β to General Principles. *Acc. Chem. Res.* **2014**, *47*, 2252-2259.
4. Pithadia, A. S.; Lim, M. H., Metal-associated Amyloid-β Species in Alzheimer's Disease. *Curr. Opin. Chem. Biol.* **2012**, *16*, 67-73.
5. Gonzalez, P.; da Costa, V. C.; Hyde, K.; Wu, Q.; Annunziata, O.; Rizo, J.; Akkaraju, G.; Green, K. N., Bimodal-Hybrid Heterocyclic Amine Targeting Oxidative Pathways and Copper Mis-Regulation in Alzheimer's Disease. *Metallomics* **2014**, *6*, 2072-2082.

6.   Ma, D.-L.; Shiu-Hin Chan, D.; Pui-Yan Ma, V.; Leung, K.-H.; Zhong, H.-J.; Leung, C.-H., Current Advancements in Aβ Luminescent Probes and Inhibitors of Aβ Aggregation. *Curr. Alzheimer Res.* **2012**, *9*, 830-843.

7.   Lee, H. J.; Kerr, R. A.; Korshavn, K. J.; Lee, J.; Kang, J.; Ramamoorthy, A.; Ruotolo, B. T.; Lim, M. H., Effects of Hydroxyl Group Variations on a Flavonoid Backbone toward Modulation of Metal-free and Metal-induced Amyloid-β Aggregation. *Inorg. Chem. Front.* **2016**, *3*, 381-392.

8.   Ansari, M. A.; Abdul, H. M.; Joshi, G.; Opii, W. O.; Butterfield, D. A., Protective Effect of Quercetin in Primary Neurons against Aβ(1–42): Relevance to Alzheimer's Disease. *J. Nutr. Biochem.* **2009**, *20*, 269-275.

9.   DeToma, A. S.; Krishnamoorthy, J.; Nam, Y.; Lee, H. J.; Brender, J. R.; Kochi, A.; Lee, D.; Onnis, V.; Congiu, C.; Manfredini, S.; Vertuani, S.; Balboni, G.; Ramamoorthy, A.; Lim, M. H., Synthetic Flavonoids, Aminoisoflavones: Interaction and Reactivity with Metal-Free and Metal-Associated Amyloid-β Species. *Chem. Sci.* **2014**, *5*, 4851-4862.

10. Man, B. Y.-W.; Chan, H.-M.; Leung, C.-H.; Chan, D. S.-H.; Bai, L.-P.; Jiang, Z.-H.; Li, H.-W.; Ma, D.-L., Group 9 Metal-based Inhibitors of β-amyloid (1–40) Fibrillation as Potential Therapeutic Agents for Alzheimer's Disease. *Chem. Sci.* **2011**, *2*, 917-921.

11. Lai-Fung Chan, S.; Lu, L.; Lung Lam, T.; Yan, S.-C.; Leung, C.-H.; Ma, D.-L., A Novel Tetradentate Ruthenium(II) Complex Containing Tris(2- pyridylmethyl)amine (tpa) as an Inhibitor of Beta-Amyloid Fibrillation. *Curr. Alzheimer Res.* **2015**, *12*, 434-438.

12. Lu, L.; Zhong, H.-J.; Wang, M.; Ho, S.-L.; Li, H.-W.; Leung, C.-H.; Ma, D.-L., Inhibition of Beta-Amyloid Fibrillation by Luminescent Iridium(III) Complex Probes. *Sci. Rep.* **2015**, *5*, 14619.

13. Istrate, A. N.; Kozin, S. A.; Zhokhov, S. S.; Mantsyzov, A. B.; Kechko, O. I.; Pastore, A.; Makarov, A. A.; Polshakov, V. I., Interplay of Histidine Residues of the Alzheimer's Disease Aβ Peptide Governs its Zn-induced Oligomerization. *Sci. Rep.* **2016**, *6*, 21734.

14. Wähälä, K.; Hase, T. A., Expedient Synthesis of Polyhydroxyisoflavones. *J. Chem. Soc. Perkin Trans. I* **1991**, *12*, 3005-3008.

15. Ghosh, A.; Pradhan, N.; Bera, S.; Datta, A.; Krishnamoorthy, J.; Jana, N. R., Inhibition and Degradation of Amyloid Beta (Aβ40) Fibrillation by Designed Small Peptide: A Combined Spectroscopy, Microscopy, and Cell Toxicity Study. *ACS Chem. Neurosci.* **2017**, *8*, 718-722.

16. Wright, J. S.; Johnson, E. R.; DiLabio, G. A., Predicting the Activity of Phenolic Antioxidants: Theoretical Method, Analysis of Substituent Effects, and Application to Major Families of Antioxidants. *J. Am. Chem. Soc.* **2001**, *123*, 1173-1183.

17. Silva, M. M.; Santos, M. R.; Caroço, G.; Rocha, R.; Justino, G.; Mira, L., Structure-antioxidant Activity Relationships of Flavonoids: A Re-examination. *Free Rad. Res.* **2002**, *36*, 1219-1227.

18. Sato, M.; Murakami, K.; Uno, M.; Nakagawa, Y.; Katayama, S.; Akagi, K.-i.; Masuda, Y.; Takegoshi, K.; Irie, K., Site-specific Inhibitory Mechanism for Amyloid β42 aggregation by catechol-type flavonoids targeting the Lys residues. *J. Biol. Chem.* **2013**, *288*, 23212-23224.

19. Uriarte-Pueyo, I.; I. Calvo, M., Flavonoids as Acetylcholinesterase Inhibitors. *Curr. Med. Chem.* **2011**, *18*, 5289-5302.

20. Eagger, S. A.; Levy, R.; Sahakian, B. J., Tacrine in Alzheimer's Disease. *Lancet* **1991**, *337*, 989-992.

21. Bourne, Y.; Grassi, J.; Bougis, P. E.; Marchot, P., Conformational Flexibility of the Acetylcholinesterase Tetramer Suggested by X-ray Crystallography. *J. Biol. Chem.* **1999**, *274*, 30370-30376.

22. Bitan, G.; Tarus, B.; Vollers, S. S.; Lashuel, H. A.; Condron, M. M.; Straub, J. E.; Teplow, D. B., A Molecular Switch in Amyloid Assembly: Met35 and Amyloid β-Protein Oligomerization. *J. Am. Chem. Soc.* **2003**, *125*, 15359-15365.

23. Palmblad, M.; Westlind-Danielsson, A.; Bergquist, J., Oxidation of Methionine 35 Attenuates Formation of Amyloid β-peptide 1–40 Oligomers. *J. Biol. Chem.* **2002**, *277*, 19506-19510.

24. Inoue, K.; Garner, C.; Ackermann, B. L.; Oe, T.; Blair, I. A., Liquid Chromatography/Tandem Mass Spectrometry Characterization of Oxidized Amyloid Beta Peptides as Potential Biomarkers of Alzheimer's Disease. *Rapid Commun. Mass Spectrom.* **2006**, *20*, 911-918.

25. Schöneich, C.; Williams, T. D., Cu(II)-Catalyzed Oxidation of β-Amyloid Peptide Targets His13 and His14 over His6: Detection of 2-Oxo-histidine by HPLC-MS/MS. *Chem. Res. Toxicol.* **2002**, *15*, 717-722.

26. van den Berg, R.; Haenen, G. R. M. M.; van den Berg, H.; Bast, A., Applicability of an Improved Trolox Equivalent Antioxidant Capacity (TEAC) Assay for Evaluation of Antioxidant Capacity Measurements of Mixtures. *Food Chem.* **1999**, *66*, 511-517.

27. Kochi, A.; Eckroat, T. J.; Green, K. D.; Mayhoub, A. S.; Lim, M. H.; Garneau-Tsodikova, S., A Novel Hybrid of 6-chlorotacrine and Metal–amyloid-β Modulator for Inhibition of Acetylcholinesterase and Metal-induced Amyloid-β Aggregation. *Chem. Sci.* **2013**, *4*, 4137-4145.

28. Ji, Y.; Lee, H. J.; Kim, M.; Nam, G.; Lee, S. J. C.; Cho, J.; Park, C.-M.; Lim, M. H., Strategic Design of 2, 2′-bipyridine Derivatives to Modulate Metal–amyloid-β Aggregation. *Inorg. Chem.* **2017**, *56*, 6695-6705.

29. Mruk, D. D.; Cheng, C. Y., Enhanced Chemiluminescence (ECL) for Routine Immunoblotting: An Inexpensive Alternative to Commercially Available Kits. *Spermatogenesis* **2011**, *1*, 121-122.

30. Derrick, J. S.; Kerr, R. A.; Nam, Y.; Oh, S. B.; Lee, H. J.; Earnest, K. G.; Suh, N.; Peck, K. L.; Ozbil, M.; Korshavn, K. J., A Redox-active, Compact Molecule for Cross-linking Amyloidogenic Peptides into Nontoxic, Off-pathway Aggregates: In Vitro and In Vivo Efficacy and Molecular Mechanisms. *J. Am. Chem. Soc.* **2015**, *137*, 14785-14797.

31. Beck, M. W.; Derrick, J. S.; Suh, J. M.; Kim, M.; Korshavn, K. J.; Kerr, R. A.; Cho, W. J.; Larsen, S. D.; Ruotolo, B. T.; Ramamoorthy, A., Minor Structural Variations of Small Molecules Tune Regulatory Activities toward Pathological Factors in Alzheimer's Disease. *ChemMedChem* **2017**, *12*, 1828-1838.

32. Derrick, J. S.; Lee, J.; Lee, S. J. C.; Kim, Y.; Nam, E.; Tak, H.; Kang, J.; Lee, M.; Kim, S. H.; Park, K., Mechanistic Insights into Tunable Metal-mediated Hydrolysis of Amyloid-β Peptides. *J. Am. Chem. Soc.* **2017**, *139*, 2234-2244.

33. Han, J.; Lee, H. J.; Kim, K. Y.; Lee, S. J. C.; Suh, J.-M.; Cho, J.; Chae, J.; Lim, M. H., Tuning Structures and Properties for Developing Novel Chemical Tools toward Distinct Pathogenic Elements in Alzheimer's Disease. *ACS Chem. Neurosci.* **2018**, *9*, 800-808.

34. Barclay, L. R. C.; Locke, S. J.; MacNeil, J. M.; VanKessel, J.; Burton, G. W.; Ingold, K. U., Autoxidation of Micelles and Model Membranes. Quantitative Kinetic Measurements Can be Made by Using either Water-soluble or Lipid-soluble Initiators with Water-soluble or Lipid-soluble Chain-breaking Antioxidants. *J. Am. Chem. Soc.* **1984**, *106*, 2479-2481.

35. Trott, O.; Olson, A. J., AutoDock Vina: Improving the Speed and Accuracy of Docking with a New Scoring Function, Efficient Optimization, and Multithreading. *J. Comput. Chem.* **2010**, *31*, 455-461.

Chapter 3

Multiple Reactivities of Flavonoids towards Pathological Elements in Alzheimer's Disease: Structure-Activity Relationship
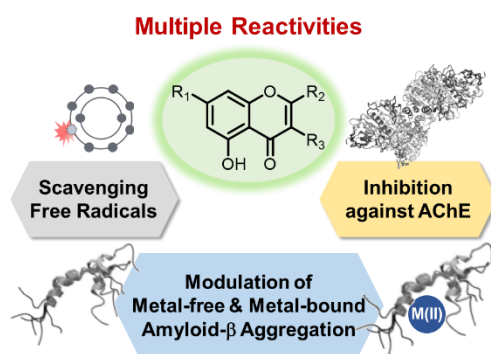
The results and discussion presented in this chapter were described in the submitted manuscript [Nam, G.;† Hong, M.;† Lee, H. J.; Ji, Y.; Lee, J.; Kang, J.; Baik, M. -H.; Lim, M. H. Submitted for Publication (†equal contribution)]. Professor Baik and Mannkyu Hong carried out all computational studies and analyses regarding the redox potentials and AChE interactions of the flavonoids. Yonghwan Ji, Dr. Juhye Kang, and I were involved in synthesizing 5-hydroxyisoflavone (**HIF**) and orobol (**Oro**). Dr. Hyuck Jin Lee and I performed gel/Western blot experiments. Dr. Hyuck Jin Lee obtained the TEM images. Juri Lee carried out the TEAC and AChE activity assays with the corresponding data analyses. Mannkyu Hong and I wrote the manuscript under the direction of Professor Mi Hee Lim.

3.1. Introduction

AD is a progressive neurodegenerative disorder responsible for a majority of dementia.[1,2] Despite extensive research aimed at developing therapeutics, there is no cure and our capability of controlling the development and progression of AD is severely limited.[2,3] Currently available symptomatic treatments offer temporary relief using AChE inhibitors and N-methyl-D-aspartic acid receptor antagonists.[3] AChE terminates cholinergic transmission at the synapse by catalyzing the hydrolysis of the neurotransmitter, ACh.[4] The cholinergic hypothesis identifies the reduced level of ACh as a primary culprit in the pathogenesis of AD.[5] In recent years, however, the inability of AChE inhibitors to effectively halt the progressive neurodegeneration in AD has led to a re-evaluation of this hypothesis.[6] The prevailing perception of AD pathology reflects the multifaceted quality of the disease.[2]

Identification of additional pathological contributors of AD such as Aβ,[7] metal ions,[8] metal–Aβ,[9-12] and ROS[13] corroborates the complex nature of the disease. Aβ, the major component of senile plaques, is an aggregation-prone peptide composed of 36-43 amino acids.[7] Aβ aggregation is a subject of intensive research and Aβ oligomers were recently identified as potential toxic species capable of disrupting neuronal homeostasis.[14] Metal ions present two neurochemical implications: (i) they functions as essential cofactors and structural anchors in enzymatic reactions and protein folding and (ii) they are neurotoxic by catalyzing the generation of ROS.[10] For these reasons, metal ions are tightly regulated in biological systems. Dyshomeostasis and miscompartmentalization of metal ions such as Cu(II) and Zn(II) are observed in the brains of AD patients and linked to neurodegeneration.[10] Moreover, metal ions can affect the aggregation and conformation of Aβ by directly binding to the peptide.[9,10,15] Based on their physiological roles and reactivity with Aβ, metal ions are considered an important part of AD pathogenesis.[16] Research regarding the pathological relationship between metal ions and Aβ introduced the concept of metal–Aβ as a pathogenic factor based on its potential toxicity and involvement in producing ROS.[10,16,17] Lastly, oxidative stress, characterized by the imbalance between the formation and removal of ROS, has been indicated in a spectrum of diseases including AD for detriments such as lipid peroxidation and peptide oxidation.[18,19]

Attempts to exploit these pathological elements for the development of single target-based therapeutics have been made, but were largely shown to be clinically ineffective.[20,21] As a result, research efforts have shifted towards understanding the connections among the various pathogenic pathways in AD. There is growing recognition that chemical reagents capable of simultaneously targeting and modulating multiple pathological features are necessary for potential therapeutic candidates and chemical tools for elucidating the pathology of AD at the molecular level. In this work, we evaluated the reactivities of flavonoids against the pathological elements of AD such as metal-free and metal-bound Aβ, free radicals, and AChE and identified the structural features responsible for their versatile reactivities, as depicted in Figure 3.1.

Flavonoids are a family of phytochemicals exhibiting low toxicity,[22] anti-/pro-oxidant
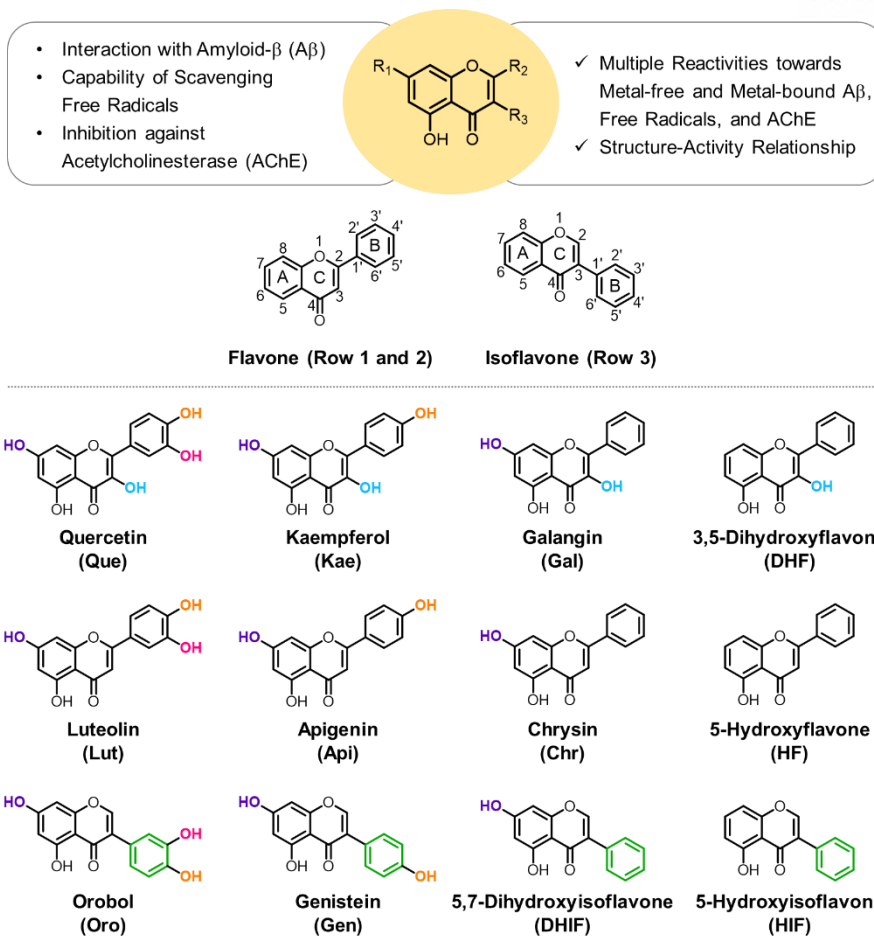
Figure 3.1. Rational selection of 12 flavonoids. The presented library of flavonoids was chosen based on structural variations, including the number and position of hydroxyl groups and the location of the B ring, to identify the structural features responsible for reactivities against multiple pathological factors found in AD [*i.e.*, metal-free Aβ, metal–Aβ, free radicals, and AChE].

activity,[23] and numerous utilitarian biological activities (*e.g.*, anti-cancer,[24] anti-viral,[25] and anti-bacterial[26]). The direct administration of flavonoids, however, presents limitations in practical applications. For example, the solubility and stability of flavonoids often present challenges. Therefore, understanding the molecular structures of flavonoids and identifying their pharmacophores could be valuable in designing small molecules with multiple reactivities for investigating and treating AD. In this work, the modulative reactivities of 12 flavonoids enumerated in Figure 3.1 towards metal-free Aβ, metal–Aβ, free radicals, and AChE were assessed and analyzed based on their molecular structures to identify the structural moieties critical for their reactivities. Moreover, computational studies were carried out to obtain a more in-depth perspective of their activities against free radicals and AChE.

3.2. Results and discussion

3.2.1. Rational selection of the flavonoid library

Quercetin (**Que**), **luteolin** (**Lut**), and **orobol** (**Oro**) were included in our study because they have been

tested previously against several pathogenic elements in AD. Both **Que** and **Lut** exhibited a variety of biological activities[23,24,26] including the ability to modulate the aggregation of metal–Aβ and inhibit AChE activity.[27,28] **Oro** was found to interact with metal ions, alter the aggregation of both metal-free and metal-bound Aβ, scavenge free radicals, and inhibit the catalytic activity of AChE.[29] The 12 flavonoids enumerated in Figure 3.1 include three different classes, namely the flavonols (row 1), flavones (row 2), and isoflavones (row 3) that offer significant structural variance. These flavonoids chosen according to three structural criteria: (i) inclusion of the chromone framework containing the 4-oxo group and the double bond between C2 and C3 on the C ring; (ii) variation in hydroxyl groups at C3 (row 1 vs. row 2), C3', C4', and C7 (columns 1, 2, and 3, respectively); (iii) change in the position of the B ring from C2 to C3 (row 2 vs. row 3). Previous studies identified the 4-oxo group and the unsaturated bond between C2 and C3 on the C ring to be important in various chemical and biological properties such as their metal-binding ability and antioxidant activity.[28,30,31] Moreover, the unsaturated C2–C3 bond may contribute to interactions of the compounds with the hydrophobic regions of Aβ such as the self-recognition site and the *C*-terminal region that are essential for peptide aggregation.[32-35] The 4-oxo functionality can form 5- and 6-membered metal chelation sites with the 3-OH or 5-OH group, respectively. The catechol moiety on the B ring can also chelate metal ions. In

Scheme 3.1. Synthetic routes to **5-hydroxyisoflavone** (**HIF**).
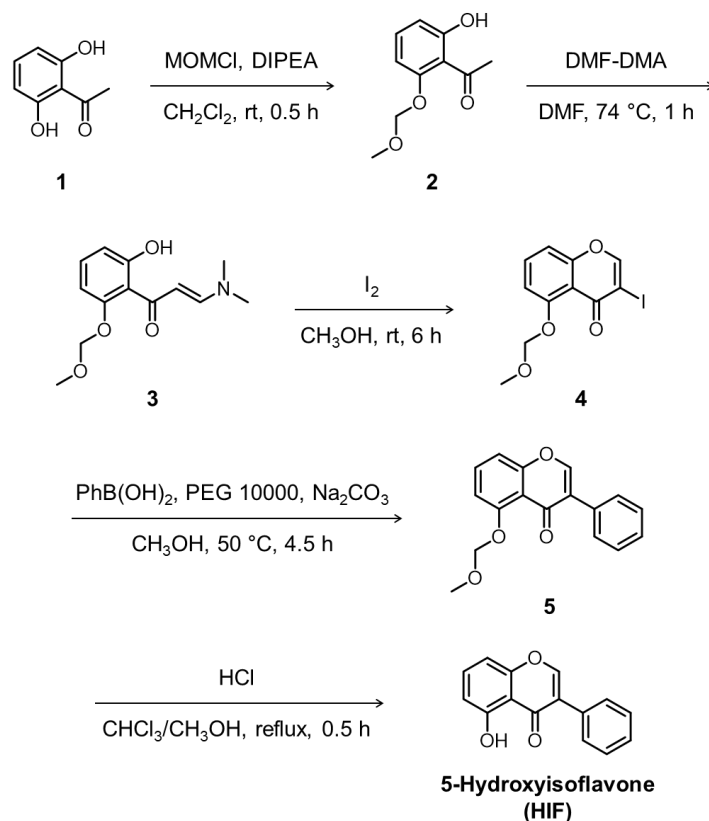
addition, the number and location of electron-donating hydroxyl groups can impact the flavonoids' redox potentials that direct their capacity to quench free radicals.[36] These 12 flavonoids were obtained through commercial sources or prepared in our laboratory in the cases of **Oro**[29] and **5-hydroxyisoflavone** (**HIF**) as depicted in Schemes 2.1 and 3.1.

3.2.2. Interaction with Cu(II)

To verify that the flavonoids interact with metal ions in solution, UV–is spectra were monitored. Significant spectral changes in the UV–Vis range were observed upon adding Cu(II), as illustrated in Figure 3.2 Two characteristic $\pi–\pi^*$ transition bands are characteristic: band I associated with the B ring of flavonoids ($\lambda = ca.$ 300–400 nm) and band II associated with the A ring ($\lambda = ca.$ 240–280 nm).[37] Treatment of the flavonoids with Cu(II) showed optical shifts of either or both band I and II, *e.g.*, bathochromic/hypsochromic and hyper/hypochromic shifts, indicative of interactions between Cu(II) and the oxygen (O) donor atoms in the A, B and C rings of the flavonoids such as 4-oxo/5-OH, 3-OH/4-oxo, and 3'-OH/4'-OH. Together, these observations confirm that all of the selected flavonoids interact with Cu(II) in solution. Unfortunately, quantitative measurements for metal-binding affinities of the flavonoids was not possible due to the limited stability of the complexes.
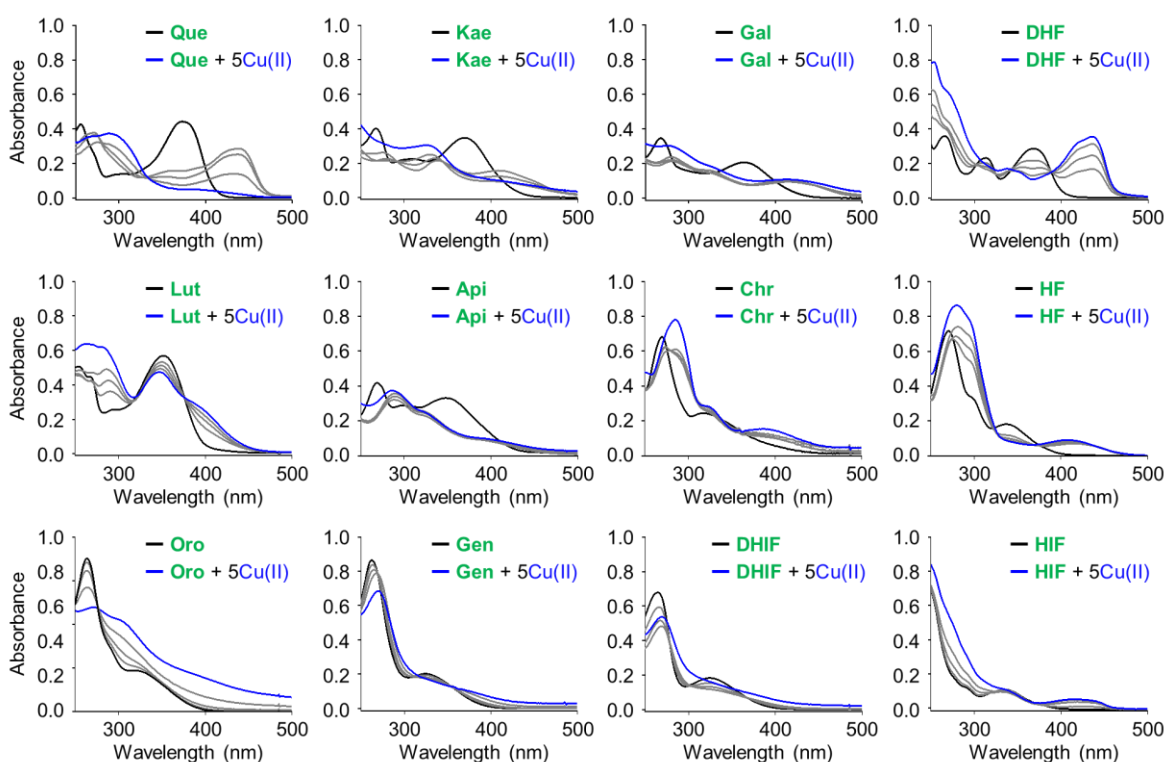

Figure 3.2. Interaction of the flavonoids with Cu(II) monitored by UV–Vis spectroscopy. Conditions: [flavonoid] = 25 μM; [CuCl$_2$] = 0, 12.5, 25, 50, and 125 μM; 20 mM HEPES, pH 6.6, 150 mM NaCl or EtOH [for chrysin (**Chr**) and 5-hydroxyflavone (**HF**)].

3.2.3. Modulation of metal-free Aβ_{42} and metal–Aβ_{42} aggregation

To determine the effects of the flavonoids on the aggregation of metal-free and metal-treated Aβ_{42}, the MW distribution and morphology of the resultant Aβ_{42} species upon incubation with the compounds were analyzed by gel/Western blot and TEM, respectively. The amount of β-sheet-rich aggregates generated through metal-free and metal-induced Aβ_{42} aggregation with treatment of the flavonoids could not be quantitatively determined due to the optical interference from the compounds within the analysis window of the assays (*e.g.*, thioflavin-T assay). Two types of Aβ aggregation experiments were performed: inhibition and disaggregation experiments, as summarized in Figures 3.3 and 3.4. For the inhibition experiments, freshly prepared metal-free or metal-added Aβ_{42} was incubated with the flavonoids for 24 h to assess whether the compounds could inhibit the formation of peptide aggregates. In the disaggregation experiments, the samples containing Aβ_{42} with and without metal ions were pre-incubated for 24 h to produce peptide aggregates and then treated with the flavonoids for an additional 24 h. The disaggregation studies determined whether the flavonoids could disassemble preformed peptide aggregates or modulate their aggregation. Under our experimental conditions, Aβ_{42} alone spontaneously aggregated to yield a heterogeneous mixture of Aβ ensembles including large aggregates that were too big to penetrate the gel matrix and be visualized by gel/Western blot. Such large aggregates were probed by TEM.[38,39] On the other hand, smaller Aβ_{42} species such as monomers and low MW oligomers indicated visible bands in gel/Western blot, but they were not detected by TEM.[40,41]

     In the inhibition experiments, as shown in Figure 3.3b, the introduction of **Que**, **Lut**, and **Oro** slightly changed the MW distribution of metal-free Aβ_{42}. The signal intensities of the bands corresponding to smaller oligomeric Aβ_{42} species (from 7 to 20 kDa) and larger oligomers (from 50 to 100 kDa) were reduced by **Que**, **Lut**, and **Oro**. In the case of Cu(II)–Aβ_{42}, **Que**, **Lut**, **Oro**, and **kaempferol** (**Kae**) modified the aggregation of the peptide notably and increased the smearing bands corresponding to species larger than *ca.* 20 kDa. Moreover, **Que**, **Lut**, and **Oro** altered the aggregation of Zn(II)–Aβ_{42}, resulting in diverse MW distributions from *ca.* 7 to 270 kDa. **Kae** did not significantly influence the aggregation of Aβ_{42} in the absence and presence of Zn(II). **Apigenin** (**Api**), **genistein** (**Gen**), **galangin** (**Gal**), **chrysin** (**Chr**), **5,7-dihydroxyisoflavone** (**DHIF**), **3,5-dihydroxyflavone** (**DHF**), **5-hydroxyflavone** (**HF**), and **HIF** did not exhibit any significant reactivity against metal-free or metal-induced Aβ_{42} aggregation.

     As depicted in Figure 3.3c, TEM images corroborated the effect of the flavonoids on the Cu(II)-induced aggregation of Aβ_{42}. The flavonoids exhibiting modulative reactivity towards the aggregation of Cu(II)–Aβ_{42} in gel/Western blot led to notable morphological changes in the peptide aggregates: (i) **Que** gave significantly shorter fibrillar aggregates; (ii) **Lut** decreased the degree of branching in the
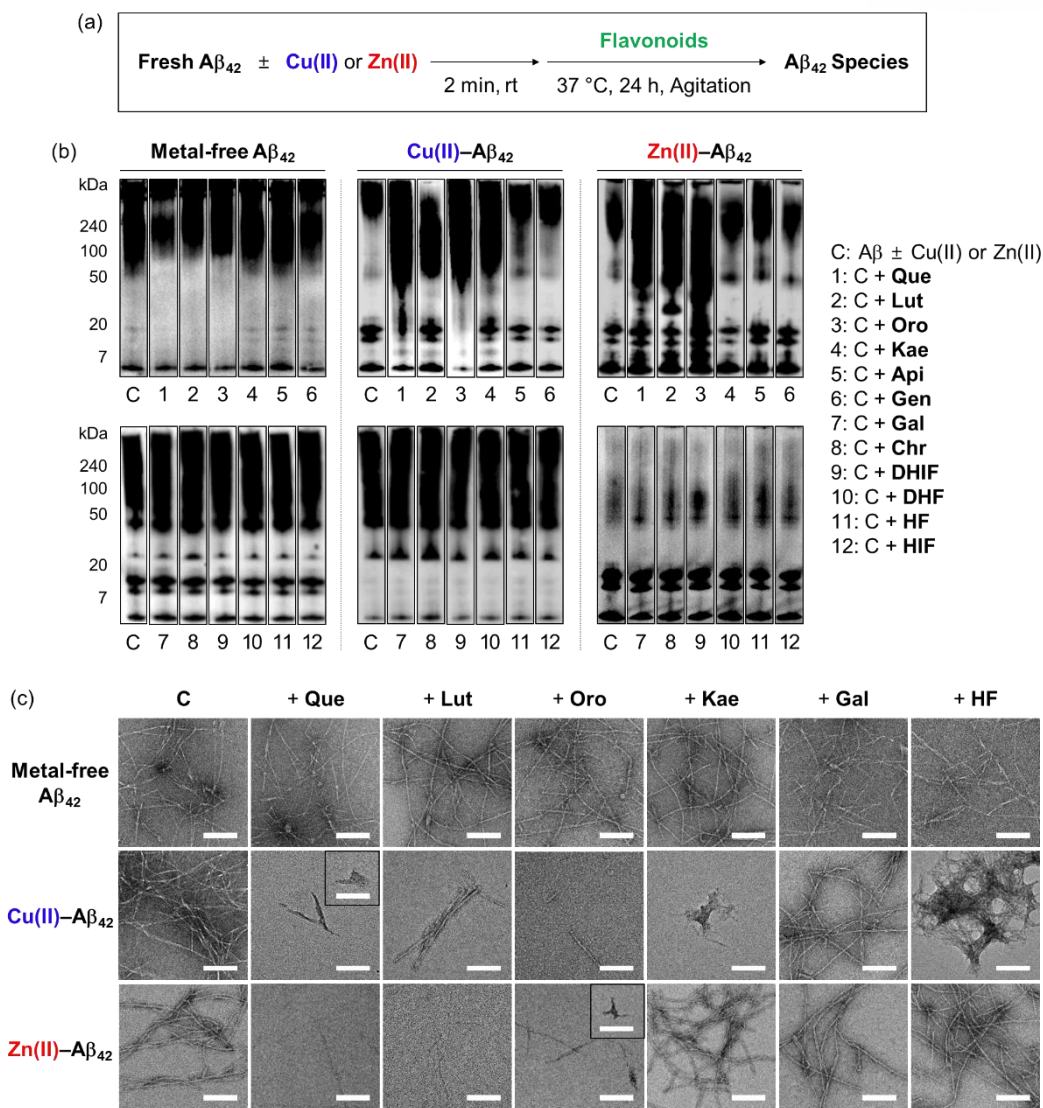
Figure 3.3. Influence of the flavonoids on the aggregation of metal-free and metal-treated $A\beta_{42}$. (a) Scheme of the inhibition experiment. (b) Analysis of the MW distribution of the resultant $A\beta_{42}$ species by gel/Western blot with an anti-$A\beta$ antibody (6E10). (c) TEM images of the samples from (b). Conditions: $[A\beta_{42}] = 25\ \mu M$; $[CuCl_2$ or $ZnCl_2] = 25\ \mu M$; $[flavonoid] = 50\ \mu M$; 20 mM HEPES, pH 7.4 [for metal-free and Zn(II)-containing samples] or pH 6.6 [for Cu(II)-added samples], 150 mM NaCl; 37 °C; 24 h incubation; constant agitation.

fibrils; (iii) **Oro** afforded thinner and shorter aggregates; (iv) **Kae** generated amorphous assemblies distinct from native $A\beta_{42}$ fibrils. As expected, **Gal** and **HF** did not significantly alter the morphologies of $A\beta_{42}$ aggregates regardless of the presence of Cu(II) or Zn(II). When Zn(II)–$A\beta_{42}$ was incubated with **Que**, **Lut**, or **Oro** that modified Zn(II)–$A\beta_{42}$ aggregation in the gel/Western blot studies, thinner chopped fibrils were detected. In the presence of **Kae**, **Gal**, and **HF**, fibrillar aggregates similar to those from the compound-free Zn(II)–$A\beta_{42}$ sample were produced. None of the flavonoids studied *via* TEM exhibited the ability to particularly change the aggregate morphology of metal-free $A\beta_{42}$.
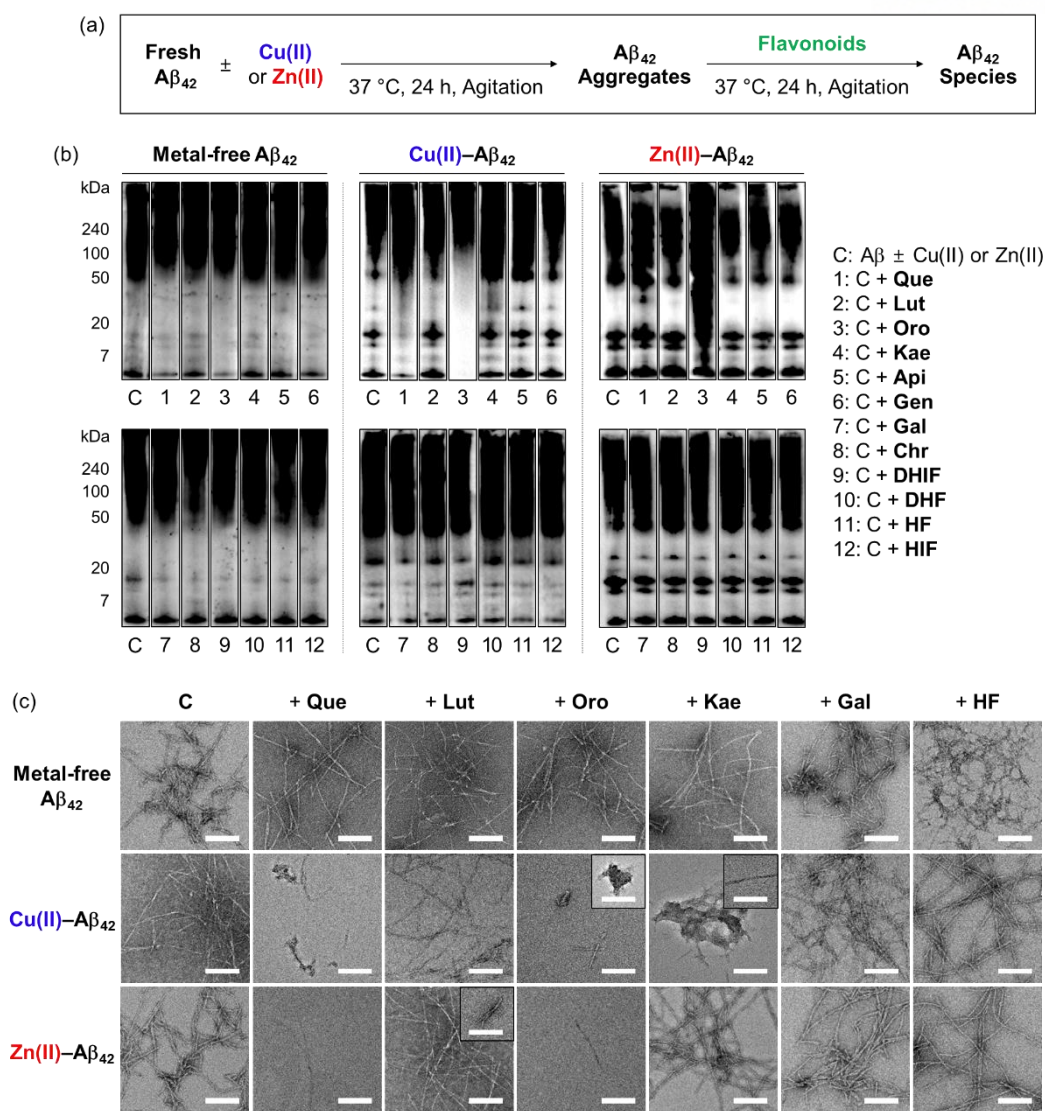
Figure 3.4. Impact of the flavonoids on the disassembly and aggregation of preformed metal-free and metal-added $A\beta_{42}$ aggregates. (a) Scheme of the disaggregation experiment. (b) Analysis of the MW distribution of the resultant $A\beta_{42}$ species by gel/Western blot with an anti-$A\beta_{42}$ antibody (6E10). (c) TEM images of the samples from (b). Conditions: $[A\beta_{42}] = 25$ μM; $[CuCl_2$ or $ZnCl_2] = 25$ μM; [flavonoid] = 50 μM; 20 mM HEPES, pH 7.4 [for metal-free and Zn(II)-containing samples] or pH 6.6 [for Cu(II)-added samples], 150 mM NaCl; 37 °C; 24 h incubation; constant agitation.

In the disaggregation experiments, as illustrated in Figure 3.4b, **Que** and **Oro** very mildly varied the MW distribution of preformed metal-free $A\beta_{42}$ aggregates. In the case of Cu(II)–$A\beta_{42}$, **Que**, **Oro**, and **Kae** exhibited the reactivity towards preformed $A\beta_{42}$ aggregates: (i) **Que** decreased the intensity of the bands corresponding to monomeric and small oligomeric species of $A\beta_{42}$ (< 20 kDa) and resulted in smearing in the range from 20 to 270 kDa; (ii) **Oro** reduced the signal intensity of all MW species below *ca.* 100 kDa; (iii) **Kae** increased smearing in the MW region from *ca.* 20 to 100 kDa. The size distribution of preformed Zn(II)–$A\beta_{42}$ aggregates upon treatment with **Que** and **Oro** differed from that of the compound-free sample, displaying greater smearing below 50 kDa. While a faint band

corresponding to species smaller than 50 kDa was observed in the **Que**-treated sample, **Oro** indicated a significantly stronger signal for the species in the same range. **Lut**, **Api**, **Gen**, **Gal**, **Chr**, **DHIF**, **DHF**, **HF**, and **HIF** did not exhibit the notable reactivity with preformed metal-free and metal-induced $A\beta_{42}$ aggregates. Demonstrating modulative reactivity towards preformed Cu(II)–$A\beta_{42}$ aggregates, **Kae** did not impact the disaggregation samples of metal-free $A\beta_{42}$ and Zn(II)–$A\beta_{42}$. As presented in Figure 3.4c, morphological changes in the metal-free and metal-treated $A\beta_{42}$ aggregates in the presence of flavonoids were monitored by TEM. As for preformed Cu(II)–$A\beta_{42}$ aggregates, **Que**, **Oro**, and **Kae** exhibiting modulative reactivity in gel/Western blot altered the morphologies of the resultant aggregates with indications of a mixture of amorphous aggregates and thinner chopped fibrils. Treatment of **Que** and **Oro** with preformed Zn(II)–$A\beta_{42}$ aggregates produced shorter fibrils. As expected from the gel/Western blot experiments, the flavonoids lacking modulative reactivity in the disaggregation experiments did not result in any morphological variations in preformed peptide aggregates.

In general, increasing the number of hydroxyl substituents on the backbone promotes the ability of the flavonoids to modify the aggregation pathways of metal–$A\beta_{42}$. Among the flavonoids, the isoflavone **Oro** carrying four hydroxyl groups with two potential metal chelation sites, *i.e.* 4-oxo/5-OH on the A/C rings and 3'-/4'-OH on the B ring, demonstrated notable modulation on the aggregation of both metal-free and metal-added $A\beta_{42}$. The pertinence of the 3-OH group in the flavonoids' modulative reactivity towards $A\beta_{42}$ was denoted by the distinctions between (i) **Kae** and **Api** and (ii) **Que** and **Lut**. **Kae** displayed notable reactivity with Cu(II)–$A\beta_{42}$ in both inhibition and disaggregation experiments, while **Api** did not show such reactivity. Moreover, **Que** altered the MW distribution of Cu(II)–$A\beta_{42}$ in both inhibition and disaggregation experiments, but **Lut** only inhibited the generation of Cu(II)–$A\beta_{42}$ aggregates. Structurally comparing **Kae**, **Gal**, and **Api**, a connection between the 3-OH and 4'-OH groups on the C and B rings, respectively, can be recognized regarding the flavonoid's influence on the aggregation of $A\beta_{42}$. The presence of the 3-OH or 4'-OH functionality alone (**Gal** and **Api**, respectively) does not result in the reactivity towards metal–$A\beta_{42}$ aggregation; however, the presence of both hydroxyl groups on the B and C rings (**Kae**) leads to noticeable reactivity. The catechol moiety on the B ring (**Que**, **Lut**, and **Oro**) fostered their interactions with metal ions and $A\beta$. Catechol-type flavonoids were reported to undergo oxidation to form *o*-quinones that in turn covalently bind to the lysine residues of $A\beta$.[42] Our results confirm the importance of the catechol moiety in the flavonoids' modulative reactivity towards $A\beta$ in the absence and presence of metal ions and further support that such reactivity could be maintained and may be altered by changing the location of the B ring catechol group, as observed with **Oro**. Taken together, the reactivity studies on metal-free and metal-induced $A\beta$ aggregation reveal three major structural features of flavonoids: (i) the 3-OH group on the C ring, (ii) a catechol moiety on the B ring, and (iii) the position of the B ring.

3.2.4. Scavenging free organic radicals

To evaluate the capacity of the flavonoids for quenching free organic radicals relative to the vitamin E analog Trolox, the TEAC assay was conducted with the cationic radical form of 2,2'-azino-bis(3-ethylbenzthiazoline-6-sulphonic acid) as the organic radical substrate.[43] As presented in Figure 3.5a, the flavonols **Que**, **Kae**, **Gal**, and **DHF** (Figure 3.1, row 1) exhibited notable scavenging capacity against free organic radicals, suggesting the importance of the 3-OH group on the C ring for this activity. As expected, **Que**, **Lut**, and **Oro** carrying a catechol moiety on the B ring showed significant antioxidant activity. Among the selected flavonoids, **Que** embodying both the 3-OH functionality and the catechol moiety was the most effective scavenger against free organic radicals. In contrast, **Api**, **Chr**, **DHIF**, **HF**, and **HIF** presented negligible radical scavenging activity compared to Trolox.

The antioxidant properties of the flavonoids are reportedly affected by the 4-oxo functionality and the double bond between C2 and C3.[44] Conjugation of the A, B, and C rings resulting in the stabilization of the flavonoid radical through resonance may be critical for their scavenging activity
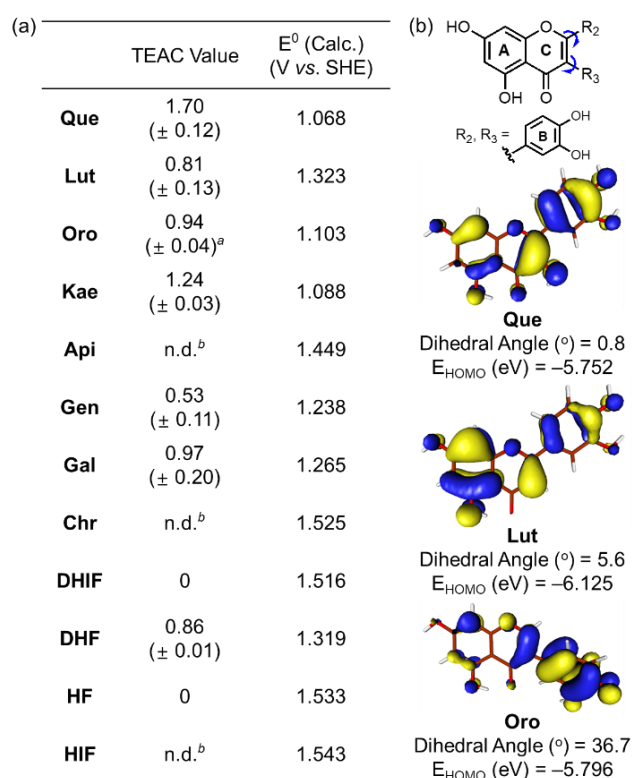

	TEAC Value	E^0 (Calc.) (V *vs.* SHE)
Que	1.70 (± 0.12)	1.068
Lut	0.81 (± 0.13)	1.323
Oro	0.94 (± 0.04)[a]	1.103
Kae	1.24 (± 0.03)	1.088
Api	n.d.[b]	1.449
Gen	0.53 (± 0.11)	1.238
Gal	0.97 (± 0.20)	1.265
Chr	n.d.[b]	1.525
DHIF	0	1.516
DHF	0.86 (± 0.01)	1.319
HF	0	1.533
HIF	n.d.[b]	1.543

Que
Dihedral Angle (°) = 0.8
E_{HOMO} (eV) = −5.752

Lut
Dihedral Angle (°) = 5.6
E_{HOMO} (eV) = −6.125

Oro
Dihedral Angle (°) = 36.7
E_{HOMO} (eV) = −5.796

Figure 3.5. Scavenging activity of the flavonoids against free organic radicals determined by the TEAC assay and their computed redox potentials. (a) Summary of the TEAC values for the flavonoids and their computed redox potentials (E^0 *vs.* SHE). Conditions: EtOH; 25 °C; λ_{abs} = 734 nm. [a]This value was obtained from reference 29. [b]n.d., not determined. The TEAC values of **Api**, **Chr**, and **HIF** could not be obtained due to limited solubility or marginal antioxidant activity levels undetected under our experimental conditions. (b) Isosurface plots (isodensity value = 0.03 a.u.) of the HOMO energy for **Que**, **Lut**, and **Oro** and their dihedral angles between two planes calculated from carbon coordinates of the A/C rings and the B ring, respectively.

against free radicals.[44] Our results employing **Chr**, **DHIF**, **HF**, and **HIF**, however, indicate that the 4-oxo group and the unsaturated C2–C3 bond do not guarantee a molecule's ability to quench free radicals effectively. The difference in the scavenging capacity against free radicals between flavonols and flavones, as shown in Figure 3.1 (row 1 and 2), respectively, may be prompted by the presence of electron-donating groups, especially at C3, that could lower their redox potentials (*vide infra*).[45] These observations indicate that the 3-OH group on the C ring is an important structural feature for the free radical scavenging capability of flavonoids. **Que**, **Lut**, and **Oro** containing a catechol moiety on the B ring exhibited the best inhibitory activity against free organic radicals according to the TEAC assay. Catechol and "catechol-type flavonoids" are recognized for their notable antioxidant activity and mechanistic studies further support their significance.[46,47] Conversely, the flavonoids possessing the 4'-OH group without 3'-OH, as depicted in Figure 3.1 (column 2), except **Kae**, did not demonstrate significant antioxidant property, further emphasizing the significance of the catechol moiety and the 3-OH group for the ability to scavenge free radicals.

3.2.5. Redox potentials

To verify the antioxidant activity of our flavonoid series, the redox potentials of all compounds were computed following a previously reported method.[48] Attempts to determine the redox potentials experimentally were made, but their instability and limited solubility in both aqueous media and organic solvents hampered electrochemical measurements. As summarized in Figure 3.5a, the computed redox potentials (E^0 vs. SHE) of the flavonoids support that the incorporation of electron-donating hydroxyl groups into the molecular framework lowers the redox potentials. Furthermore, the redox potentials depended not only on the number of electron-donating hydroxyl groups but also on their positions affecting the degree of π–conjugation between the core skeleton of the molecule and the functional group. Directly comparing the changes in the calculated E^0 suggested that the impact of a hydroxyl group on the B or C ring is more prominent than that on the A ring. The 4'-OH (column 2 vs. 3 shown in Figure 3.1), 3'-OH (column 1 vs. 2), and 3-OH (row 1 vs. 2) groups on the B and C rings decreased the E^0 values by *ca.* 0.18, 0.09, and 0.27 V, respectively, but the 7-OH group on the A ring (column 3 vs. 4) gave a difference of only *ca.* 0.03 V in the computed E^0.

Figure 3.5b illustrates the calculated dihedral angles and the highest occupied molecular orbital (HOMO) levels of the neutral forms of **Que**, **Lut**, and **Oro**. **Lut** exhibited the lowest HOMO energy (–6.13 eV) out of the three compounds of interest, which is in accord with the more positive E^0 (1.32 V vs. SHE). The HOMO level of **Que** that embodies an additional hydroxyl group at C3 on the framework of **Lut** with a relatively planar structure was elevated to –5.75 eV. On the other hand, the HOMO level of **Oro**, a regioisomer of **Lut**, was at –5.80 eV, which was higher than that of **Lut**. The better antioxidant ability of **Oro** can be rationalized by the distinctions in the conjugated π-system of the HOMO for **Lut** and **Oro**. Considering the intrinsic electronic property of the C ring enone, the α-carbon of the enone

(C3) possesses a δ^- partial charge while the β-carbon (C2) has a partial δ^+ charge. In the case of **Lut**, the electron-rich catechol is attached to the δ^+ charged β-carbon C2, preferring the π-conjugation throughout ring B and C. On the other hand, in the case of **Oro**, the catechol moiety is attached to the δ^- charged α-carbon (C3) of the enone, therefore the resonance between the B and C rings will be weakened. In the optimized structure of **Oro**, the dihedral angle between the A/C rings and the B ring was 36.7°, which is notably greater than that of **Lut**. The frontier orbitals showed that the HOMO of **Lut** was composed of a conjugated π-system throughout the A/C rings and the B ring. In contrast, the orbital lobes in the HOMO of **Oro** displayed a biased localization towards the B ring resulting in a less electronically stable HOMO. This distorted alignment of π-orbitals and the consequential disruption of π-conjugation between the two π-ring planes elevated the HOMO levels of **Oro**, making its redox potential more negative. Therefore, our experimental and computational data support that three structural components including the 3-OH group, catechol moiety, and position of the B ring considerably influence the redox potentials of the flavonoids and, subsequently, their antioxidant activity.

3.2.6. Inhibition against AChE

The 12 flavonoids were tested for their ability to inhibit the catalytic activity of AChE following a previously reported fluorometric assay with slight modifications employing *electrophorus electricus* AChE.[49] As a reference, **tacrine**, a potent inhibitor against AChE,[50] was tested under our experimental conditions ($IC_{50} = 38.7 \pm 5.0$ nM). Thereafter, the inhibitory activities of all flavonoids towards AChE were determined under the same conditions. As shown in Figure 3.6a, **Que**, **Lut**, **Oro** carrying a catechol moiety displayed notable inhibition against the activity of AChE, exhibiting IC_{50} values in the nanomolar range, although weaker than that of **tacrine**. **Kae** and **Gal** indicated high nanomolar IC_{50} values comparable to that of **Que**, while those of **Gen**, **DHIF**, and **DHF** were within the micromolar range. Lastly, the activity of AChE was not inhibited by **Api**, **Chr**, **HF**, and **HIF** under our experimental settings.

Relating these experimental results to the molecular structures, several features stand out. The catechol functionality is important for the inhibitory activity against AChE. **DHF** exhibited an IC_{50} value in the low micromolar range and the incorporation of the 7-OH group led to an increase in the inhibitory activity as observed with **Gal**. The distinct inhibitory activity between **DHIF** and **HIF** further supports the involvement of the 7-OH group, whereas the pertinence of the 3-OH functionality can be inferred from the general enhancement of the inhibitory capacity from **Api**, **Chr**, and **HF** to **Kae**, **Gal**, and **DHF**, respectively. Lastly, the enhanced AChE inhibitory effects of **Gen** and **DHIF**, relative to **Api** and **Chr**, implicate the potential influence of the B ring position on their ability to inhibit the catalytic activity of AChE.
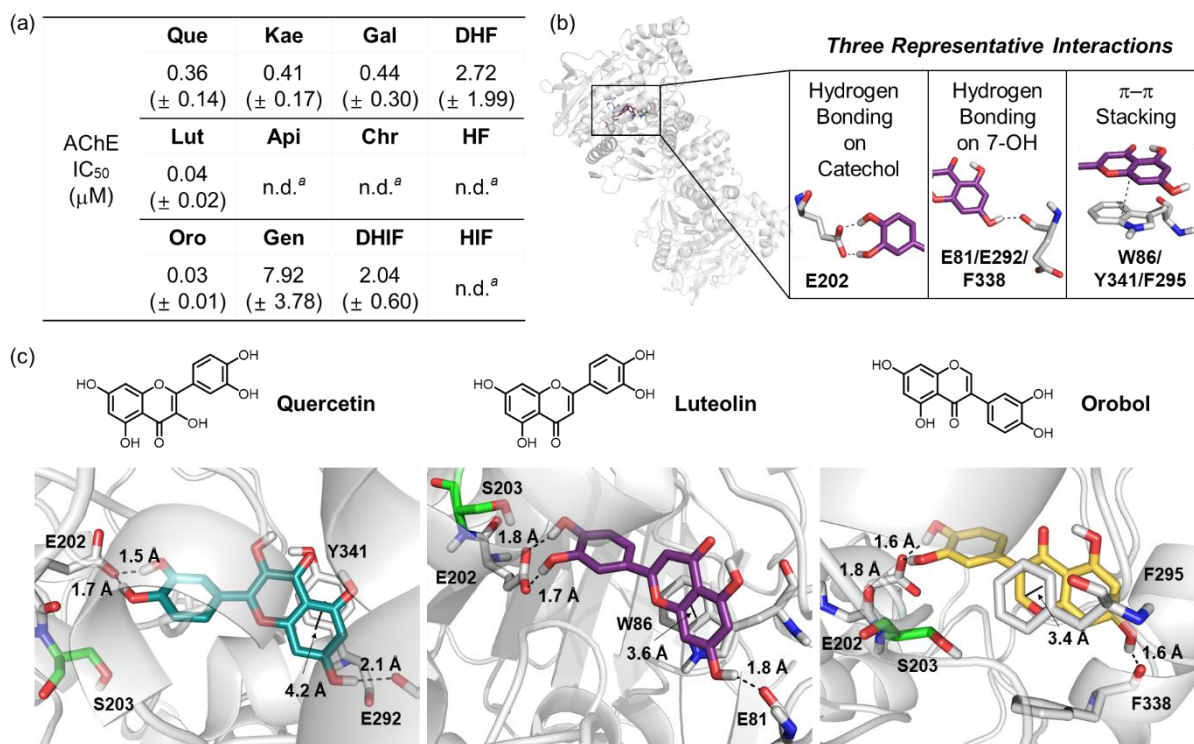
Figure 3.6. Inhibitory activity of the flavonoids against AChE. (a) Summary of the IC_{50} values of the flavonoids against *ee*AChE determined by a fluorometric assay. (b) Intermolecular interactions between the flavonoids and AChE (PDB 1C2O)[51] observed by aMD simulations. (c) Visualization of the flavonoid–AChE interactions modeled through aMD simulations. N, O, and H (from hydroxyl groups) atoms in the flavonoid ligand are depicted in blue, red, and white, respectively. *a*n.d., not determined. Inhibitory activity of **Api**, **Chr**, **HF**, and **HIF** against AChE was too low to be detected under our experimental conditions and, thus, an accurate IC_{50} value could not be determined.

3.2.7. Computational studies for interactions with AChE

Based on their distinct structural characteristics and IC_{50} values against AChE, five flavonoids, **Que**, **Lut**, **Oro**, **HF**, and **DHF**, were chosen for a detailed computational evaluation of their interactions with AChE. Specifically, the binding configurations and interactions of the selected flavonoids towards the AChE dimer were analyzed by accelerated molecular dynamics (aMD) simulations. Details of these simulations are given in the Supporting Information. This method has been shown to improve the fidelity of the simulated poses in studies of ligand–protein interactions by enhancing the sampling efficiencies.[52] The structural clustering analysis of three potent flavonoids, **Que**, **Lut**, and **Oro**, against AChE identified three representative interactions between the compounds and AChE (PDB 1C2O[51]), as depicted in Figure 3.6b and 3.6c: (*i*) The most dominant interaction observed by the aMD simulations is the hydrogen bonding between the catechol moiety on the B ring and neighboring amino acid residues, where the E202 residue in AChE is the dominant partner hydrogen bond accepting partner. (*ii*) The 7-OH group on the A ring serves as a hydrogen bond donor to interact with a carbonyl moiety from a backbone amide group of E81/G82, E292/S293, or F338/L339 in the gorge region of the pocket. (*iii*) A

π–π stacking interaction between the chromone framework of the flavonoids on the A and C rings and the amino acid residues containing a π-ring such as W86, Y341, and F295 within the hydrophobic pocket of AChE was detected.

Based on the initial identification of these flavonoid–AChE interactions, a more detailed computational analysis was performed on the representative binding modes of the three potent inhibitors, **Que**, **Lut**, and **Oro**, against AChE. As shown in Figure 3.6b and 3.6c, a closer inspection of the binding configurations between the flavonoids and AChE revealed the hydrogen bonding between the catechol moiety on the B ring and the carboxylate group of E202. The presence of such hydrogen bonding interactions in close proximity to S203 could limit the accessibility of the substrate ACh to the catalytic triad responsible for catalyzing the hydrolysis of the neurotransmitter. Such anchoring of the flavonoids near S203 through hydrogen bonding may explain the relatively high inhibitory activity of **Que**, **Lut**,
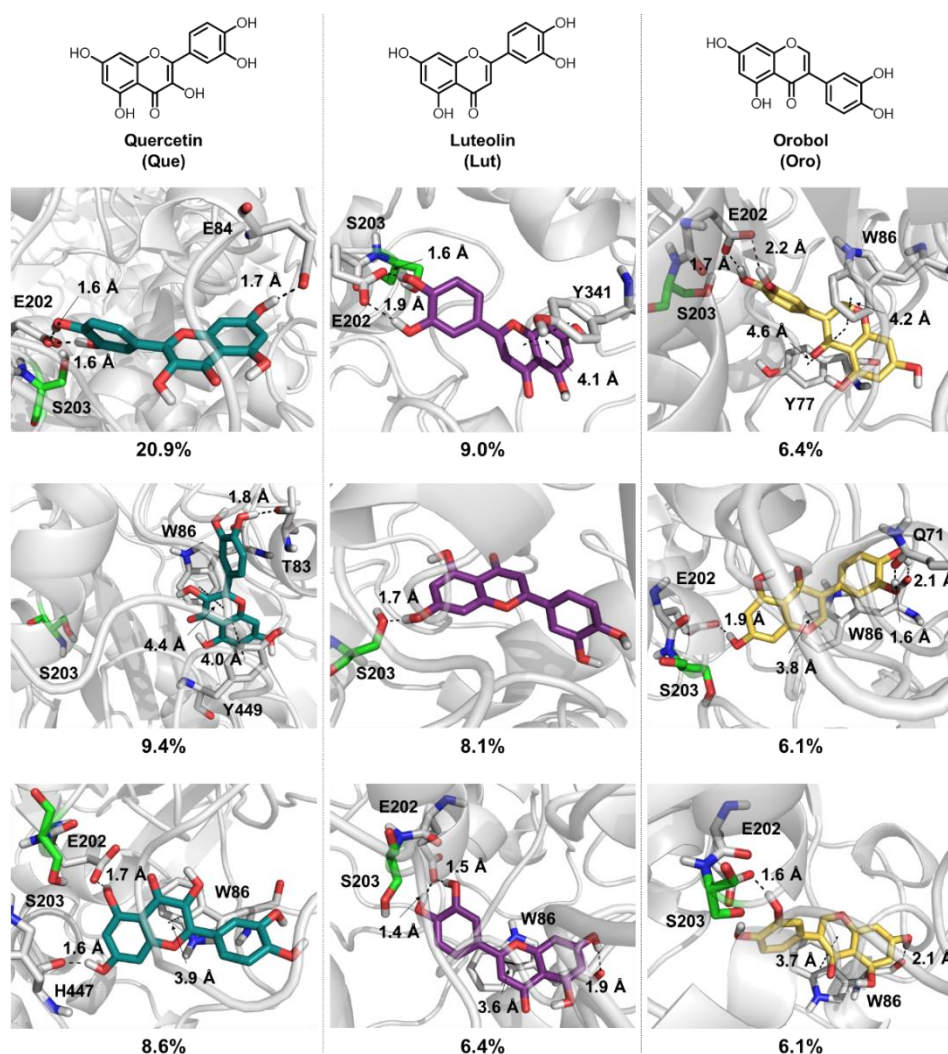

Figure 3.7. Alternative binding modes of **Que**, **Lut**, and **Oro** against AChE (PDB 1C2O)[51] modeled through aMD simulations and their % populations (# of snapshots for each cluster / # of snapshots in the total simulation × 100).

51

and **Oro** towards AChE. These observations emphasize the pertinent role of the catechol moiety on the B ring in controlling the activity of AChE. Other binding modes, *e.g.* where the A ring is arranged towards S203, were also sampled from the clustering analysis, as illustrated in Figure 3.7. They typify a relatively small population, suggesting that they play only a minor role in the overall binding characteristic. Moreover, the π–π stacking interactions between the A/C rings and the tryptophan, tyrosine, and phenylalanine residues also provided additional stability for binding of the flavonoids to AChE. The chromone moieties of **Lut** and **Oro** interact with W86 and F295, respectively, while **Que** displayed a slightly longer π–π distance to Y341. The additional 3-OH functionality on **Que**, distinguishing it from **Lut**, did not show notable interactions with any amino acid residues in the binding pocket of AChE, as presented in Figure 3.8a. The hydrogen bond mediated by the 7-OH group indicated longer distances with a large standard deviation than those formed between the catechol moiety and E202.
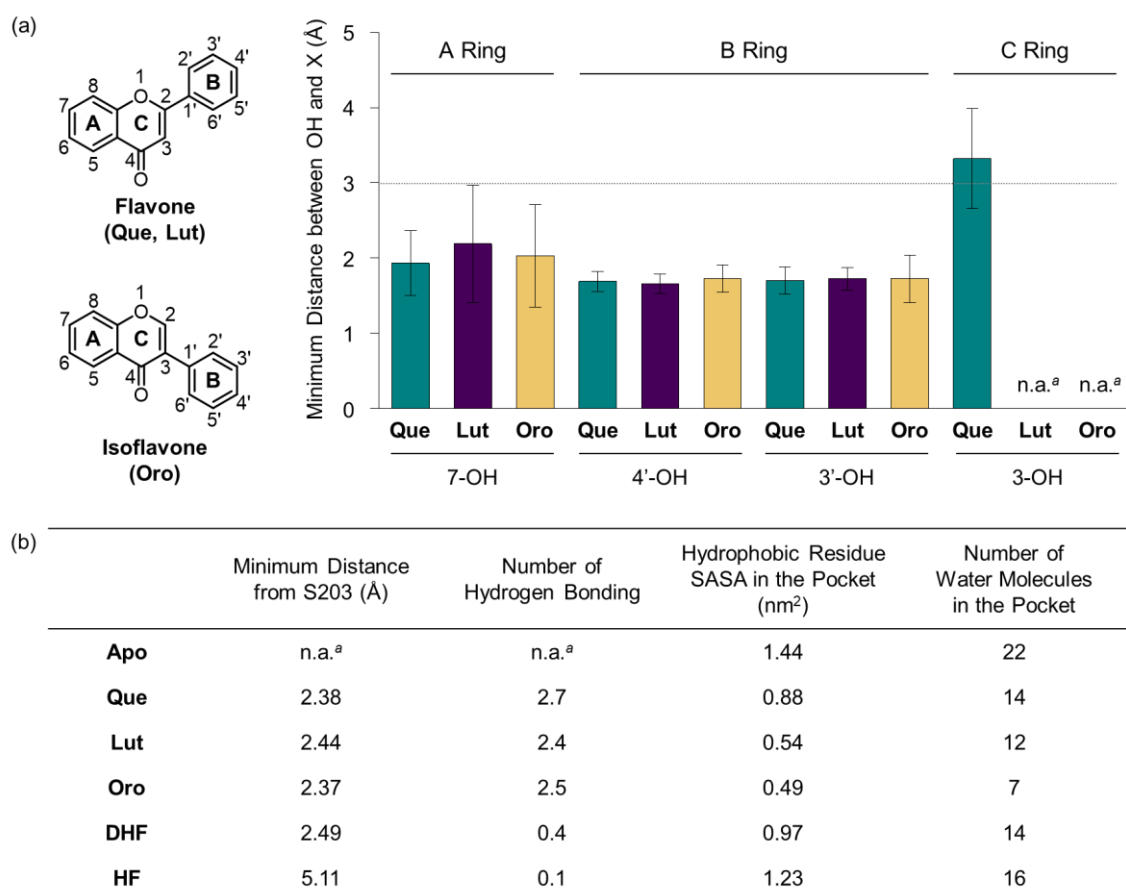

	Minimum Distance from S203 (Å)	Number of Hydrogen Bonding	Hydrophobic Residue SASA in the Pocket (nm^2)	Number of Water Molecules in the Pocket
Apo	n.a.[a]	n.a.[a]	1.44	22
Que	2.38	2.7	0.88	14
Lut	2.44	2.4	0.54	12
Oro	2.37	2.5	0.49	7
DHF	2.49	0.4	0.97	14
HF	5.11	0.1	1.23	16

Figure 3.8. Computational parameters of the interactions between the selected flavonoids and AChE (PDB 1C2O[51]). (a) Closest distance between hydroxyl groups in the flavonoids and the heteroatom (X = O or N) in the binding pocket. [a]n.a., not available. Error bars represent the standard deviation. (b) Calculated mean values for the selected binding determinants: the minimum distance from S203, the number of hydrogen bonding, the SASA of the hydrophobic residues in the binding pocket, and the number of water molecules in the binding pocket.
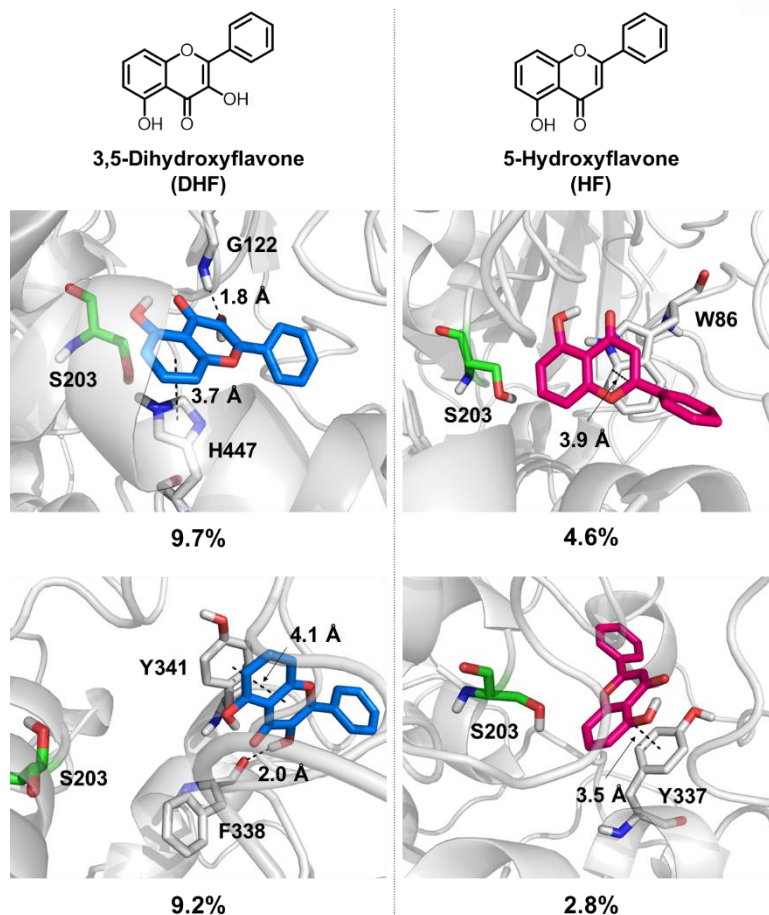
Figure 3.9. Possible binding modes of **DHF** and **HF** against AChE (PDB 1C2O)[51] generated by aMD simulations and their % populations (# of snapshots for each cluster / # of snapshots in the total simulation × 100).

The binding modes of **DHF** and **HF**, whose inhibitory potency towards AChE was relatively weak ($IC_{50} > 2.0$ μM), were also analyzed, as visualized in Figure 3.9. The two compounds do not possess the catechol moiety on the B ring or the 7-OH group on the A ring. The clustering analysis of the aMD trajectories indicated distinct binding characteristics of **DHF** and **HF** towards AChE compared to **Que**, **Lut**, and **Oro**. **DHF** did not interact with E202, but it was still compact enough to position itself within the hydrophobic pocket by preserving the hydrogen bonding between the 3-OH group and the side chain of G122. In the case of **HF**, we were not able to obtain an aMD cluster for the compound populating more than 5% of the trajectories, in accord with its low inhibitory activity against AChE. Nevertheless, we considered the most clustered conformation of **HF** for further exploration and analysis.

Upon determining the binding configurations between the selected flavonoids and AChE, statistical analysis regarding four specific physical parameters, including the distance from S203, the number of hydrogen bonding, the solvent accessible surface area (SASA) of the hydrophobic residues lining the active site pocket, and the number of water molecules in the active site pocket, were conducted to provide more in-depth details of the flavonoid–AChE interactions, as shown in Figures 3.8b and 3.10.
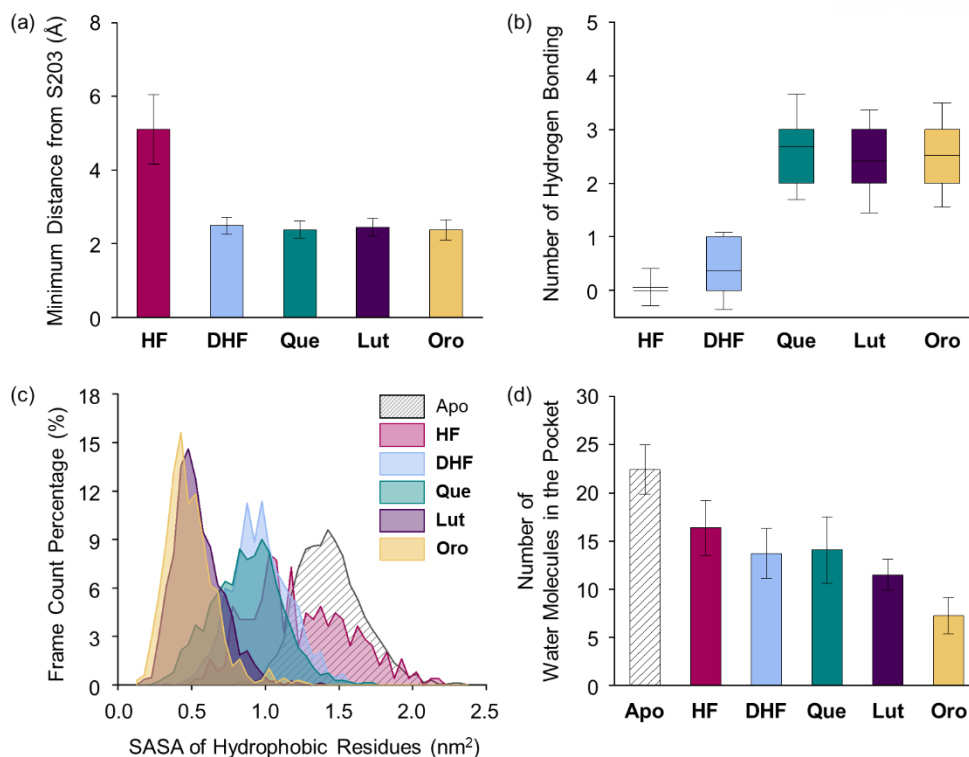
Figure 3.10. Evaluation of flavonoid-binding determinants against AChE (PDB 1C2O)[51]. (a) Closest distance between the flavonoid and S203 of the catalytic triad. (b) Box plot of the number of hydrogen bonding between the flavonoid and AChE. The box extends to the top 25% and bottom 75% of the clustered data. The black line represents the mean value of each computed case. (c) SASA distribution of the hydrophobic residues in the active site. (d) Average count of water molecules in the binding pocket for the apo and holo cases. Error bars represent the standard deviation.

The minimum distance between the flavonoid and S203 was measured. On average, aMD simulations with **Que**, **Lut**, **Oro**, and **DHF** presented relatively short distances (below 2.5 Å) to S203, as illustrated in Figure 3.10a, implying that they can remain in the binding site interior. **HF** was positioned away (5.1 Å) from the catalytic residue, which is consistent with its minimal inhibitory potency. The distance to S203 alone is not sufficient to discern more potent inhibitors, however, as **DHF** was also found to maintain close contact with S203 despite its weak inhibitory activity towards AChE. The number of hydrogen bonding between the flavonoids and the binding pocket residues was calculated to assess the relative stabilities of the identified binding poses, as presented in Figure 3.10b. The lack of adequately positioned hydrogen bond donors or acceptors on **HF** and **DHF** led to poorly established hydrogen bonding with AChE, as shown in Figure 3.9. **Que**, **Lut**, and **Oro** exhibited a significantly greater number of hydrogen bonds than **HF** and **DHF**, which supports again the notion that the catechol moiety on the B ring and the 7-OH group on the A ring are crucial structural features for interacting with AChE.

The SASA values of the hydrophobic residues residing within 6.0 Å from S203 was examined as a measure of the binding pocket stability in the presence of a ligand.[53] As displayed in Figure 3.10c, the SASA values of the hydrophobic residues in the presence of **Lut** and **Oro** were found to be 0.54

54

and 0.49 nm^2, respectively, suggesting that the hydrophobic residues effectively minimized unfavorable contacts with the polar solvent medium. In addition, the relatively low level of fluctuations in the computed SASAs indicated the increased stability of the binding pocket with **Lut** and **Oro**. The SASA alone, however, cannot be considered a computational parameter in evaluating the potency of compounds as **Que** and **DHF** showed comparable SASA values (0.88 and 0.97 nm^2, respectively), while their ability to inhibit AChE activity varied significantly. The **HF**-bound structure exhibited a mean SASA value of 1.23 nm^2 with significantly large fluctuations. This implied the unstable organization of the hydrophobic residues upon binding of **HF** to the active site.

Finally, the dynamics of the water molecules in the binding pocket is another critical factor influencing the binding properties of ligands.[54] We analyzed the number of water molecules in the active site gorge within 8.0 Å from the C$_{\alpha}$ atom of S203 for each simulated flavonoid–AChE binding modes, relative to the number of water molecules in the *apo* state, as illustrated in Figure 3.10d. The number of water molecules in *holo* states decreased by more than 5 in the presence of the flavonoids, while 22 water molecules were present in the *apo* state. In line with the computational findings described above, the **HF**-bound conformation contained the most water molecules in the binding pocket (16 on average). In contrast, **Que** and **DHF** disclosed the lower number of water molecules within the active site than that of **HF**. **Lut** and **Oro** exhibiting stronger inhibition activity against AChE led to the least amount of water molecules in the hydrophobic pocket (on average, 12 and 7, respectively). Combining the experimental and computational results, several structural features of the flavonoids can be connected to their inhibitory activity against AChE. Our structure-activity relationship study regarding the inhibition towards AChE underscores the importance of (i) the catechol moiety on the B ring to facilitate hydrogen bonding with E202, (ii) the 7-OH group for hydrogen bonding, and (iii) the chromone framework for π–π stacking with the hydrophobic residues lining the active site gorge. The aMD simulations also provide a detailed representation of the possible interactions between the flavonoids and AChE at the active site with multiple key parameters related to the strength of their interactions.

3.3. Conclusions

The complexity of the multifaceted AD pathology has led to increased interest in the development of chemical reagents with multiple functions. Considering the versatile reactivity of the three naturally occurring flavonoids, a series of 12 flavonoids was selected and investigated with respect to their reactivities towards four pathogenic elements including metal-free Aβ$_{42}$, metal–Aβ$_{42}$, free radicals, and AChE implicated in AD. Through our detailed investigations, several structural features were identified to be likely connected to the reactivities towards the aforementioned targets. First, the catechol moiety on the B ring of the flavonoids notably promoted the molecules' modulative reactivities against metal-free Aβ, metal–Aβ, free organic radicals, and AChE. The two *ortho*-hydroxyl substituents on the B ring of flavonoids presented the ability to (i) chelate metal ions in a bidentate manner forming a 5-membered

ring, (ii) undergo oxidation to produce an *ortho*-quinone that can covalently bind to the lysine residues in Aβ,[42] (iii) effectively scavenge free organic radicals *via* radical stabilization through hydrogen bonding,[55,56] and (iv) inhibit the catalytic activity of AChE by sterically blocking off the catalytic active site by interacting with the amino acid residues lining the active site gorge. Second, the hydroxyl group at C3 contributed towards the (i) chelation of metal ions in a bidentate manner manifesting a 5-membered metal-binding site, (ii) modulation of metal-free or metal-induced Aβ aggregation when accompanied by hydroxyl substituents on the B ring, (iii) scavenging free organic radicals, and (iv) inhibition of AChE activity in conjunction with the hydroxyl group at C7. Third, the isoflavone variation accompanied by the presence of a catechol moiety on the B ring impacted the molecule's reactivities by altering the molecule's thermodynamic properties such as HOMO energy. As for the free radical scavenging activity of the flavonoids, the structural features lowering the computed redox potentials were observed to increase the molecule's antioxidant capacity. In addition to the catechol functionality on the B ring, the 7-OH group on the A ring contributed towards inhibition against AChE through hydrogen bonding. The chromone framework of the flavonoids also demonstrated supplemental interactions with the active site gorge of AChE through π–π stacking. Overall, our structure-activity relationship study employing a series of 12 flavonoids demonstrates that alterations in the number and location of hydroxyl groups, the presence of a catechol moiety, and the location of the B ring substantially contribute towards the versatile reactivities of flavonoids with multiple pathogenic elements in AD.

3.4. Experimental section

3.4.1. Materials and methods

All reagents were purchased from commercial suppliers and used as received unless noted otherwise. NMR and high-resolution mass spectrometric analyses of small molecules were conducted on an Agilent 400-MR DD2 NMR spectrometer (UNIST Central Research Facilities, Ulsan, Republic of Korea) and Q exactive plus orbitrap mass spectrometer (HRMS; Thermo Fisher Scientific, Waltham, MA, USA), respectively. Absorbance and fluorescence values for biological assays were measured on a Molecular Devices SpectraMax M5e microplate reader (Sunnyvale, CA, USA). Trace metal contamination was removed from buffers and solutions used in metal binding and Aβ aggregation experiments by treating with Chelex overnight (Sigma-Aldrich, St. Louis, MO, USA). Optical spectra were recorded on an Agilent 8453 UV−Vis spectrophotometer (Santa Clara, CA, USA). $Aβ_{42}$ (DAEFRHDSGYEVHHQKLVFFAEDVGSNKGAIIGLMVGGVVIA) was purchased from AnaSpec (Fremont, CA, USA) and Peptide Institute (Osaka, Japan). ddH_2O was obtained from a Milli-Q Direct 16 system (18.2 MΩ·cm; Merck KGaA, Darmstadt, Germany). Morphologies of peptide aggregates were taken by a JEOL JEM-2100 transmission electron microscope (200 kV; 25,000x magnification; UNIST Central Research Facility, Ulsan, Republic of Korea) and a Tecnai F30 (FEI) transmission

electron microscope (KAIST Analysis Center for Research Advancement, Daejeon, Republic of Korea).

3.4.2. Synthesis of 5-hydroxyisoflavone (HIF)

Synthesis of 1-[2-hydroxy-6-(methoxymethoxy)phenyl]ethanone (2). 2,6-Dihydroxyacetophenone (303 mg, 2.0 mmol) was dissolved with CH_2Cl_2 (10 mL) in a flame-dried flask. The resultant mixture was cooled to 0 °C, and N,N-diisopropylethylamine (450 μL, 3 mmol) was slowly introduced. After 20 min, methyl chloromethyl ether (MOMCl; 159 μL, 2 mmol) was added dropwise. The reaction mixture was maintained at 0 °C for 20 min and then brought to room temperature followed by being quenched with H_2O (40 mL). The aqueous collection was extracted with $CHCl_3$ (3 × 40 mL). The combined organic layers were dried using magnesium sulfate ($MgSO_4$) and concentrated to obtain the product [yield: 316 mg (82%)]. ^1H NMR [400 MHz; $CDCl_3$, δ (ppm)]: 13.12 (s, 1H), 8.36 (t, $J = 8.4$ Hz, 1H), 6.62 (m, 2H), 5.30 (s, 2H), 3.54 (s, 3H), 2.74 (s, 3H). ^{13}C NMR [100 MHz; $CDCl_3$, δ (ppm)]: 205.0, 164.4, 158.9, 136.1, 111.7, 111.6, 104.0, 94.5, 56.7, 33.7.

Synthesis of 3-(dimethylamino)-1-[2-hydroxy-6-(methoxymethoxy)phenyl]prop-2-en-1-one (3). 2 (316 mg, 1.6 mmol) was dissolved in N,N-dimethylformamide (DMF) (10 mL), and the solution was heated to 74 °C in an oil bath. N,N-dimethylformamide dimethyl acetal (DMF-DMA; 700 μL, 8.0 mmol) was then added dropwise to the flask. After the mixture was stirred for 4.5 h, it was cooled to room temperature. The reaction was quenched with H_2O (100 mL) and the mixture was extracted with ethyl acetate (EtOAc; 100 mL). The extracts were washed with H_2O (50 mL), dried with $MgSO_4$, and concentrated under reduced pressure. The resultant residues were purified by column chromatography (SiO_2; EtOAc) to give a yellow solid [yield: 337 mg (83%)]. [400 MHz; CDCl, δ (ppm)]: 14.24 (s, 1H), 7.98 (d, $J = 12.3$ Hz, 1H), 7.21 (t, $J = 8.3$ Hz, 1H), 6.62 (d, $J = 8.3$ Hz, 1H), 6.53 (d, $J = 8.3$ Hz, 1H), 6.31 (d, $J = 12.3$ Hz, 1H), 5.25 (s, 2H), 3.54 (s, 3H), 3.20 (s, 3H), 2.96 (s, 3H). ^{13}C NMR [100 MHz; $CDCl_3$, δ (ppm)]: 190.6, 164.3, 157.4, 154.8, 133.1, 112.7, 111.9, 104.8, 97.6, 95.2, 56.6, 45.3, 37.3.

Synthesis of 3-iodo-5-(methoxymethoxy)-4H-chromen-4-one (4). A solution of **3** (337 mg, 1.3 mmol) and I_2 (399 mg, 1.9 mmol) in CH_3OH (30 mL) was stirred at room temperature for 6 h followed by being concentrated under reduced pressure to give a red-black residue. To remove the remaining I_2, the residue was treated with saturated aqueous sodium sulfite (Na_2SO_3) until the mixture became clear. The mixture was then extracted with $CHCl_3$ (3 × 40 mL), and the extracts were dried with $MgSO_4$ and concentrated under reduced pressure. The resulting off-white solid was purified by chromatography [SiO_2; EtOAc/hexanes (1:1)] to give a white solid [yield: 271 mg (61%)]. ^1H NMR [400 MHz; $CDCl_3$, δ (ppm)]: 8.19 (s, 1H), 7.58 (t, $J = 8.4$ Hz, 1H), 7.12 (m, 2H), 5.35 (s, 2H), 3.57 (s, 3H). ^{13}C NMR [100 MHz; $CDCl_3$, δ (ppm)]: 172.0, 158.0, 157.0, 156.1, 134.0, 113.6, 111.9, 111.2, 95.5, 89.2, 56.7.

Synthesis of 5-(methoxymethoxy)-3-phenyl-4*H***-chromen-4-one (5).** PEG 10000 (6.7 g), ground to a fine consistency in a mortar, and palladium acetate [Pd(OAc)$_2$; 7.9 mg, 0.04 mmol] were added to a solution of sodium carbonate (Na$_2$CO$_3$; 174 mg, 2.0 mmol) in CH$_3$OH (10 mL). The reaction mixture was heated to 50 °C in a water bath. When the mixture turned black, 4 (271 mg, 0.82 mmol) and phenylboronic acid (209 mg, 2.1 mmol) were added. After being stirred for 3 h, the resulting mixture was filtered, washed with CH$_3$OH (40 mL), and concentrated under reduced pressure. The mixture was extracted with H$_2$O and EtOAc (3 × 40 mL), and the extracts were dried with MgSO$_4$ and concentrated under reduced pressure. The white solid was used in the next reaction without further purification [yield: 181 mg (80%)]. ^{1}H NMR [400 MHz; CDCl$_3$, δ (ppm)]: 7.80 (s, 1H), 7.46 (m, 3H), 7.32(m, 3H), 7.02 (m, 2H), 5.26 (s, 2H), 3.47 (s, 3H). ^{13}C NMR [100 MHz; CDCl$_3$, δ (ppm)]: 175.9, 158.2, 157.6, 151.3, 133.6, 131.8, 192.2, 128.4, 128.1, 126.5, 111.7, 111.6, 95.5, 56.6.

Synthesis of 5-hydroxy-3-phenyl-4*H***-chromen-4-one (HIF).** A solution of **5** (181 mg, 0.99 mmol) in CHCl$_3$ (2 mL) / CH$_3$OH (2 mL) with concentrated HCl (36%, 0.5 mL) was refluxed for 1 h. The reaction was quenched with H$_2$O, and the mixture was extracted with CHCl$_3$ (2 × 10 mL). The extracts were washed with H$_2$O (10 mL) and purified by column chromatography to give the final product [SiO$_2$; EtOAc/hexanes (1:4); yield: 84 mg (35%)]. ^{1}H NMR [400 MHz; CDCl$_3$, δ (ppm)]: 12.68 (s, 1H), 8.02 (s, 1H), 7.57 (m, 3H), 7.48 (m, 3H), 6.96 (d, J = 8.4 Hz, 1H), 6.86 (d, J = 8.3 Hz, 1H). ^{13}C NMR [100 MHz; CDCl$_3$, δ (ppm)]: 181.8, 161.4, 156.6, 153.9, 135.6, 130.6, 124.4, 111.5, 107.1. HRMS: Calcd for [M + Na]$^+$, 261.0522; found, 261.0529.

3.4.3. UV−Vis measurements

The interaction of compounds with Cu(II) was detected by UV−Vis spectroscopy. The experiments were carried out in 20 mM HEPES, pH 7.4, 150 mM NaCl for most of compounds. In the case of **Chr** and **HF**, their Cu(II) interaction was monitored in ethanol (EtOH). The solutions of compounds were titrated up to 5 equiv of CuCl$_2$ at room temperature. The mixture solution was allowed to equilibrate for 5 min after the addition of CuCl$_2$ at room temperature before the spectra were recorded.

3.4.4. Aβ aggregation experiments

Aβ$_{42}$ was dissolved in ammonium hydroxide [1% v/v NH$_4$OH (aq)]. The resulting solution was aliquoted, lyophilized overnight, and stored at −80 °C. A stock solution of Aβ$_{42}$ was then prepared by dissolving the lyophilized peptide using 1% v/v NH$_4$OH (aq) (10 μL) and diluting with ddH$_2$O. All Aβ$_{42}$ samples were prepared following previously reported procedures.[57] The concentration of the peptide solution was determined by measuring the absorbance of the solution at 280 nm (ε = 1,490 M^{-1}cm^{-1}).

The buffered solution (20 mM HEPES, pH 7.4, 150 mM NaCl) was used for the preparation of $A\beta_{42}$ samples. For the inhibition studies, compounds (final concentration, 50 μM; 1% v/v DMSO) were added to the samples of $A\beta_{42}$ (25 μM) in the absence and presence of Cu(II) or Zn(II) (25 μM) followed by incubation for 24 h at 37 °C with constant agitation. For the disaggregation studies, $A\beta_{42}$ (25 μM) was incubated with and without Cu(II) or Zn(II) (25 μM) for 24 h at 37 °C with constant agitation to generate preformed $A\beta_{42}$ aggregates. The resulting $A\beta_{42}$ aggregates were then treated with compounds (50 μM) and incubated for an additional 24 h with constant agitation.

3.4.5. Gel/Western Blot

The resultant $A\beta_{42}$ species from the inhibition and disaggregation experiments were analyzed through gel/Western blot using an anti-Aβ antibody (6E10).[1] The samples (10 μL) were separated on a 10-20% Tris-tricine gel (Invitrogen, Carlsbad, CA, USA). Following separation, the peptides were transferred onto nitrocellulose membranes and blocked with bovine serum albumin (BSA; 3% w/v; Sigma-Aldrich) in TBS containing 0.1% v/v Tween-20 (Sigma-Aldrich) (TBS-T) for 4 h at room temperature or overnight at 4 °C. The membranes were incubated with 6E10 (1:2,000, Covance, Princeton, NJ, USA) in a solution of BSA (2% w/v in TBS-T) for 2 h at room temperature or overnight at 4 °C. After washing with TBS-T (3x, 10 min each), a horseradish peroxidase-conjugated goat anti-mouse secondary antibody (1:5,000 in 2% w/v BSA in TBS-T; Cayman Chemical Company, Ann Arbor, MI, USA) was added for 2 h at room temperature. Lastly, a homemade ECL kit[58] was used to visualize gel/Western blots on a ChemiDoc MP Imaging System (Bio-Rad, Hercules, USA).

3.4.6. TEM

Samples for TEM were prepared following previously reported methods.[57] Glow-discharged grids (Formvar/Carbon 300-mesh, Electron Microscopy Sciences, Hatfield, PA, USA) were treated with Aβ samples (5 μL, 25 μM) for 2 min at room temperature. Excess sample was removed using filter paper followed by washing twice with ddH₂O. Each grid, incubated with uranyl acetate (5 μL, 1% w/v in ddH₂O) for 1 min, was blotted off and dried for 15 min at room temperature. Images for each sample were taken on a transmission electron microscope. For the TEM studies, we randomly selected the locations of samples on the grids for imaging and collected more than 25 images from each grid (sample).

3.4.7. TEAC assay

The free radical scavenging capacities of compounds were determined by the TEAC assay based on the decolorization of ABTS [2,2'-azino-bis(3-ethylbenzothiazoline-6-sulfonic acid)diammonium salt] cation radical in comparison to that of the vitamin E analog, Trolox, known for its antioxidant

properties.[59] The TEAC assay was conducted in EtOH following previously reported methods.[41] Blue ABTS$^{\bullet+}$ cation radicals were generated by dissolving ABTS (7.0 mM) with potassium persulfate (2.5 mM) in H_2O (5 mL) and incubating the solution for 16 h at room temperature in the dark. Then the solution was diluted with EtOH to an absorbance of *ca.* 0.7 at 734 nm. The ABTS$^{\bullet+}$ solution (200 μL) was then added to a clear 96 well plate. Various concentrations of compounds or Trolox were added to the 96 well plate and incubated at 25 ºC for various time periods (1, 3, 6, and 10 min). Percent inhibition was calculated based on the measured absorbance at 734 nm [% inhibition = 100 x $(A_0 - A)/A_0$; A_0 = absorbance of control well without compounds; A = absorbance of wells treated with compounds] and plotted as a function of compounds' concentration. The TEAC values of each time point were calculated as the ratio between the slope of compounds and the slope of Trolox. All measurements were carried out in triplicate.

3.4.8. Calculation of redox potentials

All calculations were performed based on the density functional theory (DFT)[60] with the Jaguar 9.1 suite[61] at the B3LYP-D3[62-64] level of theory. The optimization of compounds' structures were carried out with the 6-31G** basis set.[65-67] Following geometry optimization, the electronic energies of the optimized flavonoid structures were recalculated with a high quality triple-ζ basis set cc-pVTZ(-f).[68] Vibrational frequencies for the optimized structures were calculated at the same level of theory as the geometry optimization procedure. Vibrational entropy correction along with the zero point vibrational energies were considered for proper thermodynamic approximations. Based on the optimized gas phase geometries, solvation correction energies were deduced. Self-consistent reaction field (SCRF)[69-71] approximations were considered to calculate the linearized Poisson-Boltzmann equations with the dielectric constant ε. The solvation energy used in the system was treated with ethanol (ε = 24.5). The Gibbs free energies in solution phase were computed as the following equations:

$$G(sol) = G(gas) + G(solv) \qquad (1)$$
$$G(gas) = H(gas) - TS(gas) \qquad (2)$$
$$H(gas) = E(SCF) + ZPE \qquad (3)$$

G(sol) represents the Gibbs free energy with solvation correction G(solv) from the gas phase free energy G(gas); H(gas) is the enthalpy of the molecule in gas phase; T is the temperature (298.15 K); S(gas) is the entropy of the molecule in the gas phase; E(SCF) is the self-consistent field converged electronic energy; ZPE represents the vibrational zero-point energy. To calculate the redox potential, the free energy of the one-electron oxidized form of the flavonoid was deduced by the free energy of its neutral form. Note that the dihedral angle was defined as the angle between two planes: A mean plane calculated

from ten carbon coordinates of the A/C rings using the least-squares method and another mean plane consisted of six carbon coordinates of the B ring.

3.4.9. AChE activity assay

The activity of AChE was determined by a change in fluorescence of Amplex Red under optimized conditions. *ee*AChE was dissolved and diluted to 400 mU/mL in 50 mM Tris-HCl, pH 7.4. The *ee*AChE solution (50 μL) was first added to a 96 well plate. Varying concentrations of compounds (1 μL) in dimethyl sulfoxide (DMSO) were then introduced to the 96 well plate. After shaking, the mixtures of *ee*AChE and compounds were pre-incubated for 15 min. A reaction mixture solution (50 μL) containing 500 μM ACh, 50 μM Amplex Red, 1 U/mL horseradish peroxidase, and 250 mU/mL choline oxidase in 50 mM Tris-HCl, pH 7.4 was added to each well to initiate the catalytic reaction yielding a fluorescence readout ($\lambda_{ex}/\lambda_{em}$ = 540/590 nm). The inhibitory activities of compounds against *ee*AChE was calculated by measuring fluorescence intensities from each well following a 10 min incubation period. The measured values were normalized to that of the compound-untreated control containing 1% v/v DMSO. All experiments were performed in triplicate.

3.4.10. Docking studies

Ligand docking studies were carried out to obtain plausible ligand bound conformations. With Autodock Vina,[72] the aforementioned DFT optimized structures of **Que**, **Lut**, **Oro**, **DHF**, and **HF** were docked to the CAS near the S203 of *ee*AChE (PDB 1C2O)[51]. The tetrameric structure was simplified to the dimeric form using PyMOL[73] to reduce the computational cost that resulted in a model with 1078 residues in total (Figure 3.6b). The docking grid for the ligand binding region was set as 20 x 30 x 20 Å^3 in dimension with a 0.375 Å grid spacing. Four ligand-bound structures with the highest binding affinity were chosen for each compound for further MD simulations.

3.4.11. MD simulation

Both *apo* and ligand-bound dimer models were simulated with the Amber16[74] software package. We considered the docked structures selected from the initial docking studies as the structural models of holo state. The Amber FF99SB force field[75] was used for the *ee*AChE dimer and the Generalized Amber Force Field (GAFF)[76] was used to parameterize the covalent bonding parameters of the ligands. Atomic partial charges of the ligands were computed as follows. First, we used the Gaussian09 software[77] to achieve ESP potentials around each molecule at HF/6-31G(d) level of theory. Then atomic partial charges were retrieved based on the Merz-Singh-Kollman algorithm. All simulation systems were immersed in octahedral solvation boxes filled with TIP3P[78] water molecules with a margin of 12 Å from the solvation boundary. Sodium ions (Na$^+$) were added to achieve electrostatic neutrality of the solvated simulation system which consists of approximately 285,000 atoms in total. The integration time step

was 2 fs for all MD simulations. The preliminary procedure was initiated by the energy minimization for 4,000 cycles. Next, the solvated system was equilibrated with the Berendsen thermostat at 300 K using the NVT ensemble for 5 ns. During these two steps, all carbons in the ligand as well as the Cα of the hydrophobic pocket residues present within 5.0 Å from the docked ligand were restrained with a restraint force constant of 5.0 kcal/mol/Å^2. As the third step, an isobaric ensemble (NPT) was used for 10 ns where the pressure was controlled to maintain 1 atm with a relatively weaker restraint force constant (0.1 kcal/mol/Å^2). At last, a 100 ns equilibrium step was performed without any restraints with the Langevin thermostat and the Monte Carlo barostat to keep the temperature at 300 K and the pressure at 1 atm. In addition, the particle mesh Ewald method[79] was used to treat the long-range electrostatic interactions and the SHAKE algorithm was employed to constrain the hydrogens.

3.4.12. aMD simulation

aMD simulation is a promising method to add a non-negative boost potential to the system and therefore accelerates the conformational sampling of the protein–ligand complex.[52] From the initial unbiased MD simulations (100 ns) mentioned above, the parameter sets were obtained for the aMD calculations. The detailed parameters used for the simulations are listed: $\alpha_D = 0.2$, $\alpha_P = 0.2$, and $E_{PerResidue} = 3.5$. aMD simulations were then performed for *ca.* 150 ns for each ligand-bound case by boosting both the torsional and non-bonded degrees of freedom of the model systems.

3.4.13. Analysis of the conformations sampled from the aMD simulations

The trajectories were merged with the VMD software[80] and the backbone coordinates of the seven residues in the hydrophobic pocket (*i.e.*, W86, G121, G122, S203, F297, F338, and H447) were aligned. For each aligned trajectory, the coordinates were clustered based on the RMSD metric of the ligand with a cutoff of 1.5 Å. In-house scripts for VMD and CPPTRAJ[81] were used to conduct clustering analysis. For each ligand-bound aMD simulation, the most populated major clusters were presented in Figure 3.6c. Detailed analyses of each cluster were conducted as explained in the following sections.

Hydrogen Bond Analysis. To assess the interactions between the ligand and the enzyme, the number of intermolecular hydrogen bonding was determined. Hydrogen bonds that fell within the criteria (D–A lower than the cutoff distance 3.0 Å and A–D–H lower than the cutoff angle 30° (D: H-bond donor; A: H-bond acceptor; H: Hydrogen) were counted using the VMD hbonds function.

Solvent Accessible Surface Area (SASA). The SASA values of the chosen hydrophobic residues (Ala, Ile, Leu, Phe, Val, Pro, Gly, Met, and Trp) residing within 6.0 Å from S203 in the AChE dimer model were calculated. The selected hydrophobic residues are W117, G120, G121, G122, F123, G201, S203, A204, G205, A206, A207, V209, G230, W236, F295, F297, F338, V407, G448, and I451.

Water Molecules in the Binding Pocket. To determine the presence of water molecules within the binding site, we counted the number of water molecules within 8.0 Å from the C_α atom of S203 in both *apo* and *holo* cases for each frame.

3.5. Acknowledgments

3.6. References

1.   Zhong, L.; Xu, Y.; Zhuo, R.; Wang, T.; Wang, K.; Huang, R.; Wang, D.; Gao, Y.; Zhu, Y.; Sheng, X.; Chen, K.; Wang, N.; Zhu, L.; Can, D.; Marten, Y.; Shinohara, M.; Liu, C.-C.; Du, D.; Sun, H.; Wen, L.; Xu, H.; Bu, G.; Chen, X.-F., Soluble TREM2 Ameliorates Pathological Phenotypes by Modulating Microglial Functions in an Alzheimer's Disease Model. *Nat. Commun.* **2019**, *10*, 1365.

2.   Savelieff, M. G.; Nam, G.; Kang, J.; Lee, H. J.; Lee, M.; Lim, M. H., Development of Multifunctional Molecules as Potential Therapeutic Candidates for Alzheimer's Disease, Parkinson's Disease, and Amyotrophic Lateral Sclerosis in the Last Decade. *Chem. Rev.* **2019**, *119*, 1221-1322.

3.   Rajasekhar, K.; Govindaraju, T., Current progress, Challenges and Future Prospects of Diagnostic and Therapeutic Interventions in Alzheimer's Disease. *RSC Adv.* **2018**, *8*, 23780-23804.

4.   H Ferreira-Vieira, T.; M Guimaraes, I.; R Silva, F.; M Ribeiro, F., Alzheimer's Disease: Targeting the Cholinergic System. *Curr. Neuropharmacol.* **2016**, *14*, 101-115.

5.   Bartus, R. T.; Dean, R. L.; Beer, B.; Lippa, A. S., The Cholinergic Hypothesis of Geriatric Memory Dysfunction. *Science* **1982**, *217*, 408-414.

6.   Hampel, H.; Mesulam, M. M.; Cuello, A. C.; Khachaturian, A. S.; Vergallo, A.; Farlow, M. R.; Snyder, P. J.; Giacobini, E.; Khachaturian, Z. S.; Cholinergic System Working, G.; for the Alzheimer Precision Medicine, I., Revisiting the Cholinergic Hypothesis in Alzheimer's Disease: Emerging Evidence from Translational and Clinical Research. *J. Prev. Alzheimers Dis.* **2019**, *6*, 2-15.

7.   Hamley, I. W., The Amyloid Beta Peptide: a Chemist's Perspective. Role in Alzheimer's and Fibrillization. *Chem. Rev.* **2012**, *112*, 5147-5192.

8.   Kepp, K. P., Bioinorganic Chemistry of Alzheimer's Disease. *Chem. Rev.* **2012**, *112*, 5193-5239.

9.   Atrián-Blasco, E.; Gonzalez, P.; Santoro, A.; Alies, B.; Faller, P.; Hureau, C., Cu and Zn Coordination to Amyloid Peptides: From Fascinating Chemistry to Debated Pathological Relevance. *Coord. Chem. Rev.* **2018**, *371*, 38-55.

10. Nam, G.; Lim, M. H., Intertwined Pathologies of Amyloid-β and Metal Ions in Alzheimer's Disease: Metal–Amyloid-β. *Chem. Lett.* **2019**, *48*, 951-960.

11. Mold, M.; Ouro-Gnao, L.; Wieckowski, B. M.; Exley, C., Copper Prevents Amyloid-β1–42 from Forming Amyloid Fibrils under Near-physiological Conditions In Vitro. *Sci. Rep.* **2013**, *3*, 1256.

12. Savelieff, M. G.; DeToma, A. S.; Derrick, J. S.; Lim, M. H., The Ongoing Search for Small Molecules to Study Metal-Associated Amyloid-β Species in Alzheimer's Disease. *Acc. Chem. Res.* **2014**, *47*, 2475-2482.

13. Yang, J.; Zhang, X.; Yuan, P.; Yang, J.; Xu, Y.; Grutzendler, J.; Shao, Y.; Moore, A.; Ran, C., Oxalate-curcumin–based Probe for Micro- and Macroimaging of Reactive Oxygen Species in Alzheimer's Disease. *Proc. Natl. Acad. Sci. U.S.A.* **2017**, *114*, 12384-12389.

14. Lee, S. J. C.; Nam, E.; Lee, H. J.; Savelieff, M. G.; Lim, M. H., Towards an Understanding of Amyloid-β Oligomers: Characterization, Toxicity Mechanisms, and Inhibitors. *Chem. Soc. Rev.* **2017**, *46*, 310-323.

15. Mital, M.; Wezynfeld, N. E.; Frączyk, T.; Wiloch, M. Z.; Wawrzyniak, U. E.; Bonna, A.; Tumpach, C.; Barnham, K. J.; Haigh, C. L.; Bal, W.; Drew, S. C., A Functional Role for Aβ in Metal Homeostasis? N-Truncation and High-Affinity Copper Binding. *Angew. Chem. Int. Ed.* **2015**, *54*, 10460-10464.

16. Nam, E.; Nam, G.; Lim, M. H., Synaptic Copper, Amyloid-β, and Neurotransmitters in Alzheimer's Disease. *Biochemistry* **2020**, *59*, 15-17.

17. Kepp, K. P., Alzheimer's disease: How Metal Ions Define β-amyloid Function. *Coord. Chem. Rev.* **2017**, *351*, 127-159.

18. Collin, F., Chemical Basis of Reactive Oxygen Species Reactivity and Involvement in Neurodegenerative Diseases. *Int. J. Mol. Sci.* **2019**, *20*, 2407.

19. Wang, X.; Wang, W.; Li, L.; Perry, G.; Lee, H.-g.; Zhu, X., Oxidative Stress and Mitochondrial Dysfunction in Alzheimer's Disease. *Biochim. Biophys. Acta* **2014**, *1842*, 1240-1247.

20. Berk, C.; Sabbagh, M., Successes and Failures for Drugs in Late-Stage Development for Alzheimer's Disease. *Drugs Aging* **2013**, *30*, 783-792.

21. Anderson, R. M.; Hadjichrysanthou, C.; Evans, S.; Wong, M. M., Why Do So Many Clinical Trials of Therapies for Alzheimer's Disease Fail? *Lancet* **2017**, *390*, 2327-2329.

22. McDonald, L.; Liu, B.; Taraboletti, A.; Whiddon, K.; Shriver, L. P.; Konopka, M.; Liu, Q.; Pang, Y., Fluorescent Flavonoids for Endoplasmic Reticulum Cell Imaging. *J. Mater. Chem. B* **2016**, *4*, 7902-7908.

23. Kilani-Jaziri, S.; Mustapha, N.; Mokdad-Bzeouich, I.; El Gueder, D.; Ghedira, K.; Ghedira-Chekir, L., Flavones Induce Immunomodulatory and Anti-inflammatory Effects by Activating Cellular Anti-oxidant Activity: a Structure-activity Relationship Study. *Tumor Biol.* **2016**, *37*, 6571-6579.

24. Abotaleb, M.; Samuel, S. M.; Varghese, E.; Varghese, S.; Kubatka, P.; Liskova, A.; Büsselberg, D., Flavonoids in Cancer and Apoptosis. *Cancers* **2018**, *11*, 28.

25. Mateeva, N.; Eyunni, S. V. K.; Redda, K. K.; Ononuju, U.; Hansberry, T. D.; Aikens, C.; Nag, A., Functional Evaluation of Synthetic Flavonoids and Chalcones for Potential Antiviral and Anticancer Properties. *Bioorg. Med. Chem. Lett.* **2017**, *27*, 2350-2356.

26. Xie, Y.; Yang, W.; Tang, F.; Chen, X.; Ren, L., Antibacterial Activities of Flavonoids: Structure-Activity Relationship and Mechanism. *Curr. Med. Chem.* **2015**, *22*, 132-149.

27. Lee, H. J.; Kerr, R. A.; Korshavn, K. J.; Lee, J.; Kang, J.; Ramamoorthy, A.; Ruotolo, B. T.; Lim, M. H., Effects of Hydroxyl Group Variations on a Flavonoid Backbone toward Modulation of Metal-free and Metal-induced Amyloid-β Aggregation. *Inorg. Chem. Front.* **2016**, *3*, 381-392.

28. Uriarte-Pueyo, I.; I Calvo, M., Flavonoids as Acetylcholinesterase Inhibitors. *Curr. Med. Chem.* **2011**, *18*, 5289-5302.

29. Nam, G.; Ji, Y.; Lee, H. J.; Kang, J.; Yi, Y.; Kim, M.; Lin, Y.; Lee, Y.-H.; Lim, M. H., Orobol: An Isoflavone Exhibiting Regulatory Multifunctionality against Four Pathological Features of Alzheimer's Disease. *ACS Chem. Neurosci.* **2019**, *10*, 3386-3390.

30. Engelmann, M. D.; Hutcheson, R.; Cheng, I. F., Stability of Ferric Complexes with 3-Hydroxyflavone (Flavonol), 5,7-Dihydroxyflavone (Chrysin), and 3',4'-Dihydroxyflavone. *J. Agric. Food Chem.* **2005**, *53*, 2953-2960.

31. Cao, S.; Jiang, X.; Chen, J., Effect of Zinc (II) on the Interactions of Bovine Serum Albumin with Flavonols Bearing Different Number of Hydroxyl Substituent on B-ring. *J. Inorg. Biochem.* **2010**, *104*, 146-152.

32. Sinha, S.; Lopes, D. H.; Bitan, G., A Key Role for Lysine Residues in Amyloid β-protein Folding, Assembly, and Toxicity. *ACS Chem. Neurosci.* **2012**, *3*, 473-481.

33. Tiiman, A.; Jarvet, J. r.; Gräslund, A.; Vukojević, V., Heterogeneity and Turnover of Intermediates during Amyloid-β (Aβ) Peptide Aggregation Studied by Fluorescence Correlation Spectroscopy. *Biochemistry* **2015**, *54*, 7203-7211.

34. Zhao, L. N.; Mu, Y.; Chew, L. Y., Heme Prevents Amyloid Beta Peptide Aggregation through Hydrophobic Interaction based on Molecular Dynamics Simulation. *Phys. Chem. Chem. Phys.* **2013**, *15*, 14098-14106.

35. Enache, T. A.; Chiorcea-Paquim, A.-M.; Oliveira-Brett, A. M., Amyloid Beta Peptide VHHQ, KLVFF, and IIGLMVGGVV Domains Involved in Fibrilization: AFM and Electrochemical Characterization. *Anal. Chem.* **2018**, *90*, 2285-2292.

36. Bendary, E.; Francis, R.; Ali, H.; Sarwat, M.; El Hady, S., Antioxidant and Structure–activity Relationships (SARs) of some Phenolic and Anilines Compounds. *Ann. Agric. Sci.* **2013**, *58*, 173-181.

37. Souza, R. F. V. d.; De Giovani, W. F., Synthesis, Spectral and Electrochemical Properties of Al(III) and Zn(II) Complexes with Flavonoids. *Spectrochim. Acta A* **2005**, *61*, 1985-1990.

38. Derrick, J. S.; Kerr, R. A.; Nam, Y.; Oh, S. B.; Lee, H. J.; Earnest, K. G.; Suh, N.; Peck, K. L.; Ozbil, M.; Korshavn, K. J., A Redox-active, Compact Molecule for Cross-linking Amyloidogenic Peptides into Nontoxic, Off-pathway Aggregates: In Vitro and In Vivo Efficacy and Molecular Mechanisms. *J. Am. Chem. Soc.* **2015**, *137*, 14785-14797.

39. Han, J.; Lee, H. J.; Kim, K. Y.; Lee, S. J. C.; Suh, J.-M.; Cho, J.; Chae, J.; Lim, M. H., Tuning Structures and Properties for Developing Novel Chemical Tools toward Distinct Pathogenic Elements in Alzheimer's Disease. *ACS Chem. Neurosci.* **2018**, *9*, 800-808.

40. Kang, J.; Lee, S. J. C.; Nam, J. S.; Lee, H. J.; Kang, M.-G.; Korshavn, K. J.; Kim, H.-T.; Cho, J.; Ramamoorthy, A.; Rhee, H.-W.; Kwon, T.-H.; Lim, M. H., An Iridium(III) Complex as a Photoactivatable Tool for Oxidation of Amyloidogenic Peptides with Subsequent Modulation of Peptide Aggregation. *Chem. Eur. J.* **2017**, *23*, 1645-1653.

41. Ji, Y.; Lee, H. J.; Kim, M.; Nam, G.; Lee, S. J. C.; Cho, J.; Park, C.-M.; Lim, M. H., Strategic Design of 2, 2′-bipyridine Derivatives to Modulate Metal–amyloid-β Aggregation. *Inorg. Chem.* **2017**, *56*, 6695-6705.

42. Sato, M.; Murakami, K.; Uno, M.; Nakagawa, Y.; Katayama, S.; Akagi, K.-i.; Masuda, Y.; Takegoshi, K.; Irie, K., Site-specific Inhibitory Mechanism for Amyloid β42 Aggregation by Catechol-type flavonoids Targeting the Lys Residues. *J. Biol. Chem.* **2013**, *288*, 23212-23224.

43. Forrest, V. J.; Kang, Y.-H.; McClain, D. E.; Robinson, D. H.; Ramakrishnan, N., Oxidative Stress-induced Apoptosis Prevented by Trolox. *Free Radic. Biol. Med.* **1994**, *16*, 675-684.

44. Rice-Evans, C. A.; Miller, N. J.; Paganga, G., Structure-antioxidant Activity Relationships of Flavonoids and Phenolic Acids. *Free Radic. Biol. Med.* **1996**, *20*, 933-956.

45. Treml, J.; Šmejkal, K., Flavonoids as Potent Scavengers of Hydroxyl Radicals. *Compr. Rev. Food Sci. Food Safety* **2016**, *15*, 720-738.

46. Tejero, I.; González-García, N.; González-Lafont, À.; Lluch, J. M., Tunneling in Green Tea: Understanding the Antioxidant Activity of Catechol-containing Compounds. A Variational Transition-state Theory Study. *J. Am. Chem. Soc.* **2007**, *129*, 5846-5854.

47. De La Cruz, J.; Ruiz-Moreno, M.; Guerrero, A.; López-Villodres, J.; Reyes, J.; Espartero, J.; Labajos, M.; González-Correa, J., Role of the Catechol Group in the Antioxidant and Neuroprotective Effects of Virgin Olive Oil Components in Rat Brain. *J. Nutr. Biochem.* **2015**, *26*, 549-555.

48. Baik, M.-H.; Friesner, R. A., Computing Redox Potentials in Solution: Density Functional Theory as A Tool for Rational Design of Redox Agents. *J. Phys. Chem. A* **2002**, *106*, 7407-7412.

49. Santillo, M. F.; Liu, Y., A Fluorescence Assay for Measuring Acetylcholinesterase Activity in Rat Blood and a Human Neuroblastoma Cell Line (SH-SY5Y). *J. Pharmacol. Toxicol. Met.* **2015**, *76*, 15-22.

50. Ahmed, M.; Rocha, J. B. T.; Corrêa, M.; Mazzanti, C. M.; Zanin, R. F.; Morsch, A. L. B.; Morsch, V. M.; Schetinger, M. R. C., Inhibition of Two Different Cholinesterases by Tacrine. *Chem. Biol. Interact.* **2006**, *162*, 165-171.

51. Bourne, Y.; Grassi, J.; Bougis, P. E.; Marchot, P., Conformational Flexibility of the Acetylcholinesterase Tetramer Suggested by X-ray Crystallography. *J. Biol. Chem.* **1999**, *274*, 30370-30376.

52. Hamelberg, D.; Mongan, J.; McCammon, J. A., Accelerated Molecular Dynamics: A Promising and Efficient Simulation Method for Biomolecules. *J. Chem. Phys.* **2004**, *120*, 11919-11929.

53. Barros, E. P.; Schiffer, J. M.; Vorobieva, A.; Dou, J.; Baker, D.; Amaro, R. E., Improving the Efficiency of Ligand-Binding Protein Design with Molecular Dynamics Simulations. *J. Chem. Theory Comput.* **2019**, *15*, 5703-5715.

54. Mobley, D. L.; Dill, K. A., Binding of Small-Molecule Ligands to Proteins: "What You See" Is Not Always "What You Get". *Structure* **2009**, *17*, 489-498.

55. Wright, J. S.; Johnson, E. R.; DiLabio, G. A., Predicting the Activity of Phenolic Antioxidants: Theoretical Method, Analysis of Substituent Effects, and Application to Major Families of Antioxidants. *J. Am. Chem. Soc.* **2001**, *123*, 1173-1183.

56. Procházková, D.; Boušová, I.; Wilhelmová, N., Antioxidant and Prooxidant Properties of Flavonoids. *Fitoterapia* **2011**, *82*, 513-523.

57. Lee, S.; Zheng, X.; Krishnamoorthy, J.; Savelieff, M. G.; Park, H. M.; Brender, J. R.; Kim, J. H.; Derrick, J. S.; Kochi, A.; Lee, H. J.; Kim, C.; Ramamoorthy, A.; Bowers, M. T.; Lim, M. H., Rational Design of a Structural Framework with Potential Use to Develop Chemical Reagents That Target and Modulate Multiple Facets of Alzheimer's Disease. *J. Am. Chem. Soc.* **2014**, *136*, 299-310.

58. Mruk, D. D.; Cheng, C. Y., Enhanced Chemiluminescence (ECL) for Routine Immunoblotting: An Inexpensive Alternative to Commercially Available Kits. *Spermatogenesis* **2011**, *1*, 121-122.

59. Barclay, L. R. C.; Locke, S. J.; MacNeil, J. M.; VanKessel, J.; Burton, G. W.; Ingold, K. U., Autoxidation of Micelles and Model Membranes. Quantitative Kinetic Measurements Can be Made by Using either Water-soluble or Lipid-soluble Initiators with Water-soluble or Lipid-soluble Chain-breaking Antioxidants. *J. Am. Chem. Soc.* **1984**, *106*, 2479-2481.

60. Parr, R.; Yang, W., *Density-Functional Theory of Atoms and Molecules*, Oxford University Press, New York, **1989**.

61. Bochevarov, A. D.; Harder, E.; Hughes, T. F.; Greenwood, J. R.; Braden, D. A.; Philipp, D. M.; Rinaldo, D.; Halls, M. D.; Zhang, J.; Friesner, R. A., Jaguar: A High-performance Quantum Chemistry Software Program with Strengths in Life and Materials Sciences. *I. J. Quant. Chem.* **2013**, *11*, 2110-2142.

62. Lee, C.; Yang, W.; Parr, R. G., Development of the Colle-Salvetti Correlation-energy Formula into a Functional of the Electron Density. *Phys. Rev. B* **1988**, *37*, 785-789.

63. Grimme, S.; Antony, J.; Ehrlich, S.; Krieg, H., A Consistent and Accurate Ab Initio Parametrization of Density Functional Dispersion Correction (DFT-D) for the 94 Elements H-Pu. *J. Chem. Phys.* **2010**, *132*, 154104.

64. Becke, A. D., Density-functional Exchange-energy Approximation with Correct Asymptotic Behavior. *Phys. Rev. A* **1988**, *38*, 3098-3100.

65. Hay, P. J.; Wadt, W. R., Ab Initio Effective Core Potentials for Molecular Calculations. Potentials for the Transition Metal Atoms Sc to Hg. *J. Chem. Phys.* **1985**, *82*, 270-283.

66. Wadt, W. R.; Hay, P. J., Ab Initio Effective Core Potentials for Molecular Calculations. Potentials for Main Group Elements Na to Bi. *J. Chem. Phys.* **1985**, *82*, 284-298.

67. Hay, P. J.; Wadt, W. R., Ab Initio Effective Core Potentials for Molecular Calculations. Potentials for K to Au including the Outermost Core Orbitals. *J. Chem. Phys.* **1985**, *82*, 299-310.

68. Dunning Jr., T. H., Gaussian Basis Sets for Use in Correlated Molecular Calculations. I. The Atoms Boron through Neon and Hydrogen. *J. Chem. Phys.* **1989**, *90*, 1007-1023.

69. Edinger, S. R.; Cortis, C.; Shenkin, P. S.; Friesner, R. A., Solvation Free Energies of Peptides: Comparison of Approximate Continuum Solvation Models with Accurate Solution of the Poisson−Boltzmann Equation. *J. Phys. Chem. B* **1997**, *101*, 1190-1197.

70. Friedrichs, M.; Zhou, R.; Edinger, S. R.; Friesner, R. A., Poisson−Boltzmann Analytical Gradients for Molecular Modeling Calculations. *J. Phys. Chem. B* **1999**, *103*, 3057-3061.

71. Marten, B.; Kim, K.; Cortis, C.; Friesner, R. A.; Murphy, R. B.; Ringnalda, M. N.; Sitkoff, D.; Honig, B., New Model for Calculation of Solvation Free Energies: Correction of Self-Consistent Reaction Field Continuum Dielectric Theory for Short-Range Hydrogen-Bonding Effects. *J. Phys. Chem.* **1996**, *100*, 11775-11788.

72. Trott, O.; Olson, A. J., AutoDock Vina: Improving the Speed and Accuracy of Docking with a New Scoring Function, Efficient Optimization, and Multithreading. *J. Comput. Chem.* **2010**, *31*, 455-461.

73. The PyMOL Molecular Graphics System, Version 2.0 Schrödinger, LLC, New York, NY, **2017**.

74. Case, D.; JTB, R.; Betz, D.; Cerutti III, T.; Cheatham III, T.; Darden, R., Duke, TJ Giese, H. Gohlke, AW Goetz, N. Homeyer, S. Izadi, P. Janowski, J. Kaus, A. Kovalenko, TS Lee, S. LeGrand, P. Li, T. Luchko, R. Luo, B. Madej, KM Merz, G. Monard, P. Needham, H. Nguyen, HT Nguyen, I. Omelyan, A. Onufriev, DR Roe, A. Roitberg, R. Salomon-Ferrer, CL Simmerling, W. Smith, J. Swails, RC Walker, J. Wang, RM Wolf, X. Wu, DM York and PA Kollman AMBER 2016, University of California, San Francisco, CA, **2016**.

75. Hornak, V.; Abel, R.; Okur, A.; Strockbine, B.; Roitberg, A.; Simmerling, C., Comparison of Multiple Amber Force Fields and Development of Improved Protein Backbone Parameters. *Proteins* **2006**, *65*, 712-725.

76. Wang, J.; Wolf, R. M.; Caldwell, J. W.; Kollman, P. A.; Case, D. A., Development and Testing of a General Amber Force Field. *J. Comput. Chem.* **2004**, *25*, 1157-1174.

77. Frisch, M. J.; Trucks, G. W.; Schlegel, H. B.; Scuseria, G. E.; Robb, M. A.; Cheeseman, J. R.; Scalmani, G.; Barone, V.; Petersson, G. A.; Nakatsuji, H.; Li, X.; Caricato, M.; Marenich, A. V.; Bloino, J.; Janesko, B. G.; Gomperts, R.; Mennucci, B.; Hratchian, H. P.; Ortiz, J. V.; Izmaylov, A. F.; Sonnenberg, J. L.; Williams; Ding, F.; Lipparini, F.; Egidi, F.; Goings, J.; Peng, B.; Petrone, A.; Henderson, T.; Ranasinghe, D.; Zakrzewski, V. G.; Gao, J.; Rega, N.; Zheng, G.; Liang, W.; Hada, M.; Ehara, M.; Toyota, K.; Fukuda, R.; Hasegawa, J.; Ishida, M.; Nakajima, T.; Honda, Y.; Kitao, O.; Nakai, H.; Vreven, T.; Throssell, K.; Montgomery Jr., J. A.; Peralta, J. E.; Ogliaro, F.; Bearpark, M. J.; Heyd, J. J.; Brothers, E. N.; Kudin, K. N.; Staroverov, V. N.; Keith, T. A.; Kobayashi, R.; Normand, J.; Raghavachari, K.; Rendell, A. P.; Burant, J. C.; Iyengar, S. S.; Tomasi, J.; Cossi, M.; Millam, J. M.; Klene, M.; Adamo, C.; Cammi, R.; Ochterski, J. W.; Martin, R. L.; Morokuma, K.; Farkas, O.; Foresman, J. B.; Fox, D. J. Gaussian 09 Gaussian, Inc., Wallingford, CT, **2016**.

78. Jorgensen, W. L.; Chandrasekhar, J.; Madura, J. D.; Impey, R. W.; Klein, M. L., Comparison of Simple Potential Functions for Simulating Liquid Water. *J. Chem. Phys.* **1983**, *79*, 926-935.

79. Darden, T.; York, D.; Pedersen, L., Particle mesh Ewald: An N·log(N) Method for Ewald Sums in Large Systems. *J. Chem. Phys.* **1993**, *98*, 10089-10092.

80. Humphrey, W.; Dalke, A.; Schulten, K., VMD: Visual Molecular Dynamics. *J. Mol. Graph.* **1996**, *14*, 33-38.

81. Roe, D. R.; Cheatham, T. E., 3rd, PTRAJ and CPPTRAJ: Software for Processing and Analysis of Molecular Dynamics Trajectory Data. *J. Chem. Theory Comput.* **2013**, *9*, 3084-3095.

Chapter 4

Drug Repurposing: Multifunctional Molecules against
Cu(II)–Amyloid-β, Reactive Oxygen Species, and Acetylcholinesterase
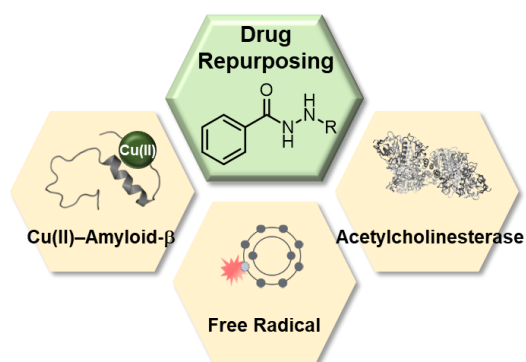
The results presented in this chapter will be included in the publication (Nam, G; Lim, M. H. Manuscript in Preparation). The synthesis of **BMX**, the studies of Cu(II) interaction, Aβ aggregation/Aβ analysis, and experiments of free organic radical scavenging and AChE inhibition were performed myself.

4.1. Introduction

Alzheimer's disease (AD) is a complex neurodegenerative disorder with fatal ramifications. The clinical symptoms of AD include progressive memory loss, deterioration of cognitive function, and abnormal psychological changes.[1] Research endeavors striving to understand the causative factors behind neurodegeneration in AD has led to the proposal of several hypotheses regarding its pathogenesis: (i) amyloid cascade, (ii) metal ion, (iii) oxidative stress, (iv) cholinergic.[1] The amyloid cascade hypothesis focuses on the role of Aβ, an aggregation-prone peptide connected to AD, in developing the pathology of the disease.[2] Recent evidence indicates soluble amyloid-β (Aβ) dimers as principal bioactive neurotoxins undermining neuronal function through the hyperexcitation of glutamatergic neurons by interfering with extracellular glutamate reuptake.[3] Metal ion dyshomeostasis and miscompartmentalization in the brain present dualistic detriments with implications in driving neurodegeneration: loss-of-function and gain-of-toxicity.[4] The redox-active metal ion, Cu(II), is denoted to contribute to AD pathology through its ability to generate reactive oxygen species (ROS) and interact with Aβ.[1] Considering the notable reactivity of ROS towards biomolecules, oxidative stress is often viewed as a general conditional pathology leading to disruption of homeostasis with implicated connections to neuroinflammation.[5] Neurons exhibit a greater sensitivity towards high concentrations of ROS due to their weaker antioxidant capabilities.[6-8] These observations indicate the enhanced neurodegenerative detriment presented by oxidative stress in the central nervous system (CNS). The cholinergic hypothesis pinpoints the deficit in the levels of the neurotransmitter acethylcholine (ACh) as a main cause of AD.[9] A majority of the currently available symptomatic treatments of AD controls the availability of ACh by inhibiting the catalytic activity of the enzyme responsible for its hydrolysis: acetylcholinesterase (AChE).[1]

The aforementioned hypotheses regarding AD pathology present four pathological factors with neurodegenerative implications. In addition to these individual factors, recent research has led to the introduction of hybrid concepts such as metal-bound Aβ (metal–Aβ).[10-11] The close association between Aβ and metal ions in amyloid plaques, found in the brains of AD patients, has led to the investigation of their pathological involvement. Reports indicate that the interactions between Aβ and metal ions [*e.g.*, Cu(II) and Zn(II)] (i) alter Aβ aggregation in a manner potentially stabilizing toxic oligomers, (ii) aggravate the miscompartmentalization of metal ions, and (iii) promote the generation of ROS through Fenton-like reactions.[1] Such observations suggest that the different pathogenic factors of AD may contribute towards neurodegeneration through interconnected pathways. This notion is further corroborated by the clinical failures of approaches individually targeting them. In recent years, a shift in paradigm towards understanding the pathogenic inter-relations among different causative factors of AD has been revealing a more complex picture of AD that is only beginning to be explored. Such experimental efforts prove that multifunctional molecules exhibiting modulative reactivities towards

multiple pathological factors of AD can be useful as investigative chemical tools or potential therapeutic candidates.

Drug repurposing presents an efficient and effective method of redeveloping previously utilized therapeutic molecules. The numerosity of pre-approved drug molecules provides an immense library of compounds accompanied with the corresponding pharmacological information including their metabolism, toxicity, and side effects. Therefore, researchers are able to search for molecules with a specific motivation and repurpose them without the need to face the grueling conventional drug development process, which can take up to 10 to 17 years from target discovery to clinical studies.[13] Major depressive disorder is a noncognitive symptom of AD affecting 5-30% of those affected by the disease.[14-15] The complexity of AD regarding the practical issues of diagnosis and patient compliance is reported to significantly affect the psychological evaluation of depression.[16] Therefore, the exact association between the two conditions remain poorly understood. Growing evidence, however, indicates a connection between depression and AD with implications in aggravating the cognitive and psychological health of the patients.[17] This notion is further supported by the consistent association between the severity of dementia and risk of depression.[18-19] Recently, alterations in the glutamatergic neurotransmitter system and microglial dysfunction have been shown to contribute towards the neurobiology linking depression and cognitive impairment.[20-22] For these reasons, our structural screening of potential multifunctional compounds for repurposing began with anti-depressants. In this work, four drug repurposing candidates were selected based on their psychological effects and molecular structures: isoniazid (**ISNZ**), iproniazid (**IPNZ**), benmoxin (**BMX**), and quetiapine (**QTP**) (Figure 4.1). The selected molecules exhibit (i) the efficacy in treating major depressive disorders, (ii) potential bidentate metal chelation sites, (iii) moderate structural similarity with previously reported Aβ-binding compounds, and the ability to bypass the blood-brain barrier (BBB).[23-25] Our biochemical and biophysical studies demonstrated the multifunctionality of **ISNZ**, **IPNZ**, and **BMX**: (i) notable modulative reactivity towards Cu(II)–Aβ$_{40}$/Aβ$_{42}$, but not metal-free or Zn(II)-treated Aβ$_{40}$/Aβ$_{42}$, (ii) capability to scavenge free organic radicals, and (iii) modest inhibitory activity against AChE.
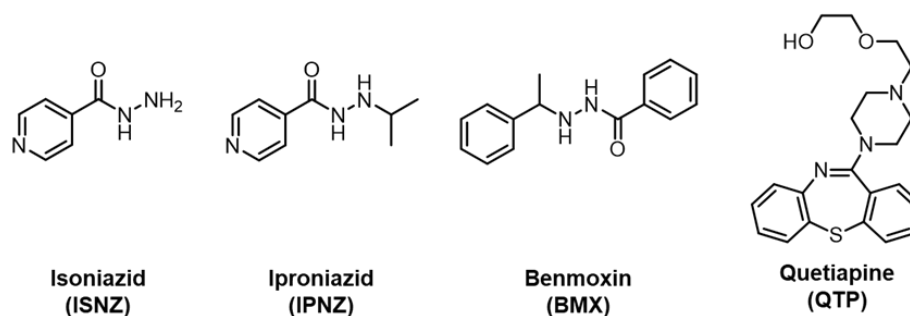

**Figure 4.1.** Chemical structures of the selected drug candidates studied in this work.

4.2. Results and discussion

4.2.1. Rational selection of repurposing candidates

A large collection of antidepressant molecules was primarily screened based on their influence on cognition and the ability to cross the BBB.[26] The molecular structures of the compounds were then examined, and those exhibiting the possibility for metal binding, structural similarity to previously reported Aβ-interacting molecules, and an adequate balance of hydrophilicity/lipophilicity were selected. Thereafter, a more in-depth inquiry of literature was performed to finalize the list of repurposing candidates: **ISNZ**, **IPNZ**, **BMX**, and **QTP** (Figure 4.1).

ISNZ is currently administered as a tuberculosis treatment based on its inhibition of monoamine oxidase (MAO).[27] Although the antidepressant effects of **ISNZ** are not utilized as the primary therapeutic purpose, the drug is noted to show the sufficient efficacy towards major depressive disorders, most likely as a result of its inhibitory effect on the activity of MAO.[28] A single study reported **ISNZ**'s ability to alter the aggregation pathways of metal-free $A\beta_{42}$.[29] **IPNZ** was previously used to treat depression through the irreversible and nonselective inhibition of MAO.[30] **IPNZ** was also reported to modify the aggregation pathways of metal-free $A\beta_{42}$.[29] **BMX** is another antidepressant capable of irreversibly and non-selectively inhibiting the activity of MAO.[32] Lastly, **QTP** is an oral antipsychotic drug used to treat schizophrenia, bipolar disorder, and major depressive disorder through its antagonistic actions against dopamine, serotonin, histamine H_1, and muscarinic ACh receptors.[33-34] Two separate studies reported that **QTP** was able to reduce the cytotoxicity of $A\beta_{25-35}$ by modulating oxidative stress and the expression and localization of Bax and BCl-X_L, two apoptotic regulators associated with the mitochondria. Previous reports of the selected compounds indicate their potential reactivity against pathogenic elements of AD. Therefore, these four antidepressant molecules, *i.e.*, **ISNZ**, **IPNZ**, **BMX**, and **QTP**, were chosen and their modulative multifunctionality against four pathological factors of AD including metal-free Aβ, metal–Aβ, ROS, and AChE were investigated. Upon establishing our series of repurposing candidates, the compounds were commercially obtained with the exception of **BMX** that was synthesized following a previously reported procedure, as described in Scheme 4.1.[35]

Scheme 4.1. Synthetic routes to **benmoxin** (**BMX**).
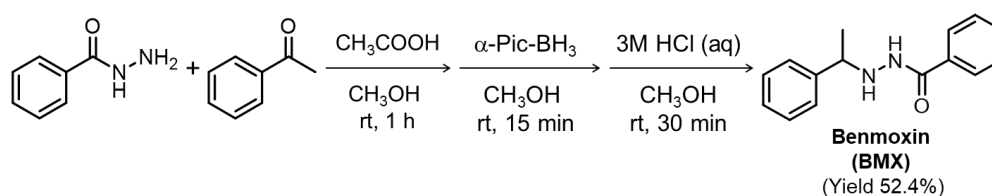
4.2.2. Modulating activity against the aggregation of metal-free Aβ₄₂ and metal–Aβ₄₂

To assess the effect of our repurposing candidates on the aggregation of Aβ₄₀/Aβ₄₂ in the absence and presence of metal ions, gel electrophoresis with Western blotting (gel/Western blot) and transmission electron microscopy (TEM) were utilized to examine the molecular weight distribution and the morphology of compound-treated Aβ species, respectively. Two types of experiments were carried out: inhibition and disaggregation experiments (Figures 4.2 and 4.3). For the inhibition experiments, freshly prepared Aβ was incubated with the compounds for 24 h in the absence or presence of metal ions to determine whether the repurposing candidates could inhibit the formation of metal-free and metal-treated Aβ aggregates. In the disaggregation experiments, the samples of metal-free Aβ and metal–Aβ were pre-incubated for 24 h to allow the generation of aggregates that were then treated with the compounds for an additional 24 h to evaluate if our selected molecules could disassemble preformed aggregates. Under our experimental conditions, Aβ alone spontaneously aggregates resulting in a heterogeneous mixture of Aβ ensembles including large assemblies that are detected *via* TEM, but are

Figure 4.2. Effects of the repurposing candidates on the formation of Aβ₄₀ and Aβ₄₂ aggregates in the absence and presence of metal ions [*i.e.*, Zn(II) and Cu(II)]. (a) Scheme of the inhibition experiments. (b) Analysis of the MW distribution of the resultant Aβ species by gel/Western blot using an anti-Aβ antibody (6E10). Conditions: [Aβ₄₀ or Aβ₄₂] = 25 μM; [CuCl₂ or ZnCl₂] = 25 μM; [compound] = 50 μM; 20 mM HEPES, pH 7.4 [for metal-free and Zn(II)-containing samples] or pH 6.6 [for Cu(II)-added samples], 150 mM NaCl; 37 °C; 24 h incubation; constant agitation.
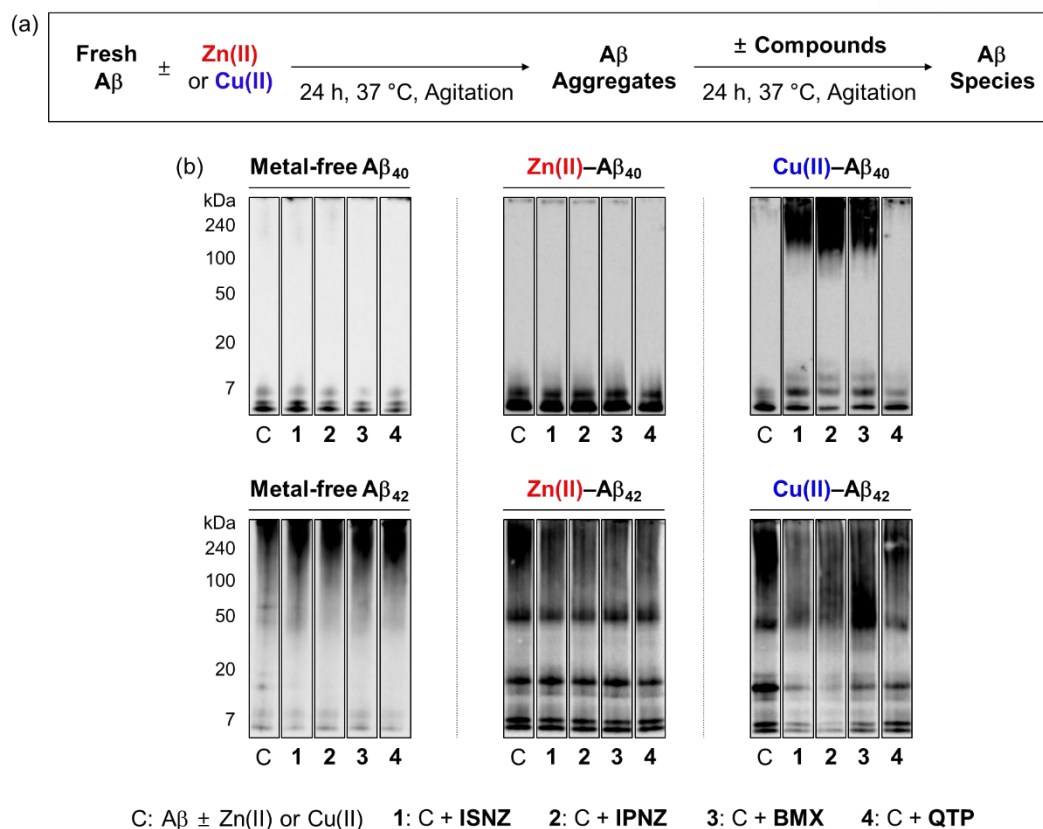
Figure 4.3. Impact of the repurposing candidates on preformed metal-free and metal-treated $A\beta_{40}$ and $A\beta_{42}$ aggregates. (a) Scheme of the disaggregation experiment. (b) Analysis of the molecular weight distribution of the resultant $A\beta_{42}$ species by gel/Western blot with an anti-$A\beta$ antibody (6E10). Conditions: $[A\beta_{40}$ or $A\beta_{42}] = 25$ μM; $[CuCl_2$ or $ZnCl_2] = 25$ μM; [compound] = 50 μM; 20 mM HEPES, pH 7.4 [for metal-free and Zn(II)-containing samples] or pH 6.6 [for Cu(II)-added samples], 150 mM NaCl; 37 °C; 24 h incubation; constant agitation.

too big to penetrate the gel matrix and be visualized by gel/Western blot.[36-38] The smaller $A\beta$ species (*e.g.*, monomers and low molecular weight oligomers) cannot be visualized by TEM; however, they produce visible bands with various molecular weights in gel/Western blot.[39,40]

Interestingly, the repurposing candidates only exhibited noticeable modulative reactivity against $A\beta$ aggregation in the presence of Cu(II) in both the inhibition and disaggregation experiments. In the inhibition experiments employing Cu(II)–$A\beta_{40}$ (Figure 4.2), the treatment of **ISNZ** led to the detection of small $A\beta$ oligomers in the range of *ca.* 7-20 kDa and the increased smearing band corresponding to aggregate species larger than *ca.* 100 kDa. **IPNZ** also resulted in the formation of small $A\beta$ oligomers in the range of *ca.* 7-20 kDa and increased smearing at *ca.* 50-240 kDa. **BMX** induced the generation of small $A\beta$ oligomers in the range of *ca.* 7-20 kDa and enhanced smearing bands corresponding to larger aggregate species *ca.* 100-270 kDa. In the case of Cu(II)–$A\beta_{42}$, both **IPNZ** and **BMX** notably altered the molecular weight distribution of Cu(II)–$A\beta_{42}$ by causing an increase in intensity of the smearing bands spanning *ca.* 7-240 kDa. **ISNZ**'s modulative reactivity towards Cu(II)–$A\beta_{42}$ was

relatively less significant in comparison to **IPNZ** and **BMX** leading to a decrease in the smaller oligomer species (*ca.* 7-20 kDa) and an increase in the smearing band (*ca.* 50-100 kDa). The disaggregation experiments demonstrated similar trends where only Cu(II)–Aβ aggregation was affected by **ISNZ**, **IPNZ**, and **BMX** (Figure 4.3). The treatment of these three molecules led to an increase in smearing at *ca.* 100-270 kDa and band intensity of *ca.* 7-20 kDa in the samples of Cu(II)–Aβ$_{40}$. In the case of Cu(II)–Aβ$_{42}$, the treatment of (i) **ISNZ** led to a general decrease in the band intensities of the species within the range of *ca.* 4-270 kDa; (ii) **IPNZ** resulted in a more significant decrease in the smaller oligomer species (*ca.* 4-20 kDa) and a less significant decrease in the band smearing at *ca.* 70-240 kDa; (iii) **BMX** induced a mild decrease in the overall band intensities and an increase in the species with the molecular weights of *ca.* 50-100 kDa. None of the compounds exhibited notable reactivity towards metal-free or Zn(II)-treated Aβ$_{40}$ and Aβ$_{42}$ under our experimental conditions in both the inhibition and disaggregation experiments. **QTP** did not display modulative reactivity against the aggregation pathways of Aβ$_{40}$ and Aβ$_{42}$ even in the presence of Cu(II).

4.2.3. Cu(II) interaction studies

Interactions between Cu(II) and the repurposing candidates were investigated by monitoring the optical changes in the ultraviolet–visible (UV–Vis) range (Figure 4.4). **ISNZ**, **IPNZ**, and **BMX** indicated discernible changes in the spectra with the addition of increasing the concentration of Cu(II), indicative of their interactions with Cu(II) in solution. The addition of Cu(II) to the solution of **QTP** did not show noticeable optical changes. Further studies regarding Cu(II) binding of **ISNZ**, **IPNZ**, and **BMX** will be carried out in the future to provide their binding affinities in solution.
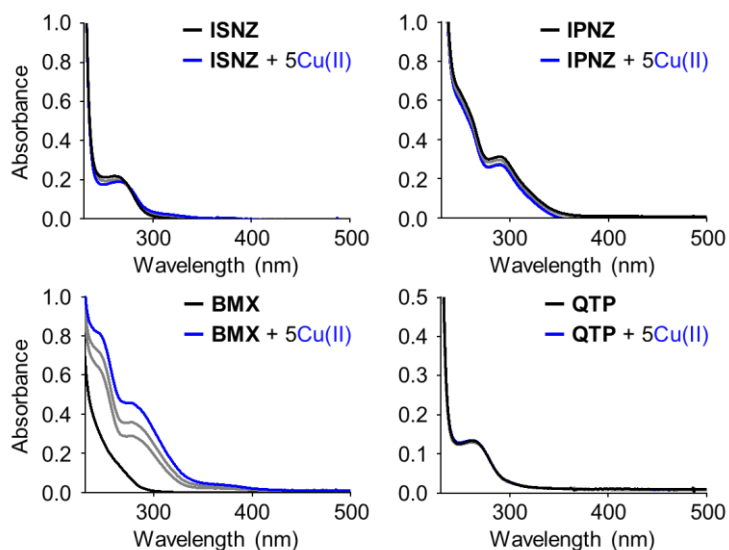

Figure 4.4. UV–Vis spectra monitoring the interactions between the repurposing candidates and Cu(II) in solution. Conditions: [Compounds] = 50 μM; [CuCl$_2$] = 0, 25, 50, 100, and 250 μM; 20 mM HEPES, pH 7.4, 150 mM NaCl; room temperature.

4.2.4. Interactions with Cu(II)-treated and metal-free Aβ

To better understand the mechanistic details behind the modulative reactivity of **ISNZ**, **IPNZ**, and **BMX** towards Cu(II)–Aβ, samples of Cu(II)–Aβ with and without the repurposing candidates were analyzed via electrospray ionization-mass spectrometry (ESI-MS). Treatment of the repurposing candidates (*i.e.*, **ISNZ**, **IPNZ**, and **BMX**) with modulative reactivity towards Cu(II)–Aβ led to the detection of singly oxidized Aβ in the samples of both Cu(II)–Aβ$_{40}$ and Cu(II)–Aβ$_{42}$ (Figure 4.5). More specifically, peaks corresponding to singly oxidized Aβ$_{40}$ at 1449.39 *m/z* were observed in the Cu(II)–Aβ$_{40}$ samples treated with **ISNZ**, **IPNZ**, and **BMX** (Figure 4.5a). In the case of Cu(II)–Aβ$_{42}$, oxidation of both metal-free Aβ$_{42}$ (1510.78 *m/z* for **ISNZ**, **IPNZ**, and **BMX**) and Cu(II)–Aβ$_{42}$ (1531.42 *m/z* for **ISNZ**, **IPNZ**, and **BMX**) was observed under our experimental conditions (Figure 4.5b).
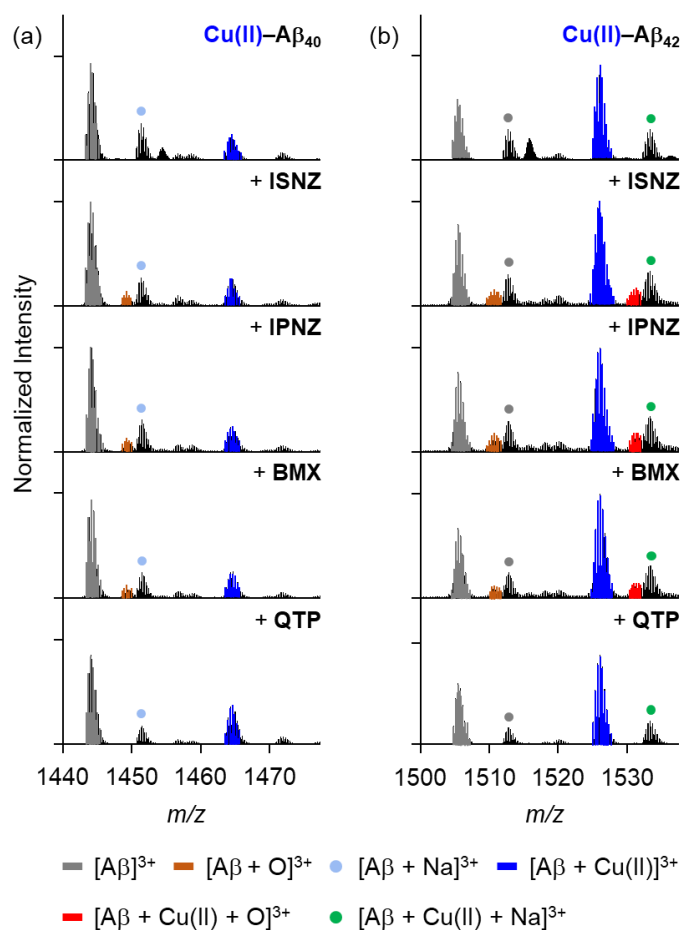
Figure 4.5. Interactions between the repositioning candidates and Cu(II)-bound Aβ monitored by ESI–MS. Spectra of the samples of (a) Cu(II)–Aβ$_{40}$ and (b) Cu(II)–Aβ$_{42}$ upon incubation with the compounds. Conditions: [Aβ$_{40}$ or Aβ$_{42}$] = 100 μM; [CuCl$_2$] = 100 μM; [compound] = 200 μM; 20 mM ammonium acetate, pH 7.4; 37 C; 3 h incubation; no agitation; the incubated samples were then diluted by ten-fold with ddH$_2$O and injected into the mass spectrometer.

It should be noted that minor peaks corresponding to the singly oxidized $A\beta_{40}$ and $A\beta_{42}$ were also detected when metal-free $A\beta_{40}$ and $A\beta_{42}$ was treated with **ISNZ**, **IPNZ**, and **BMX** (Figure 4.6). The magnitude of the aforementioned peaks, however, was significantly smaller compared to that of the peaks detected in the presence of Cu(II). Such distinctions in the degree of $A\beta$ oxidation may explain the difference in the modulative reactivity of **ISNZ**, **IPNZ**, and **BMX** towards the aggregation pathways of metal-free $A\beta$ and Cu(II)–$A\beta$. Our MS studies suggest that oxidation of $A\beta$ in the presence of Cu(II) is responsible for the ability of **ISNZ**, **IPNZ**, and **BMX** to specifically alter the aggregation of Cu(II)–$A\beta$ for both isoforms of the peptide.
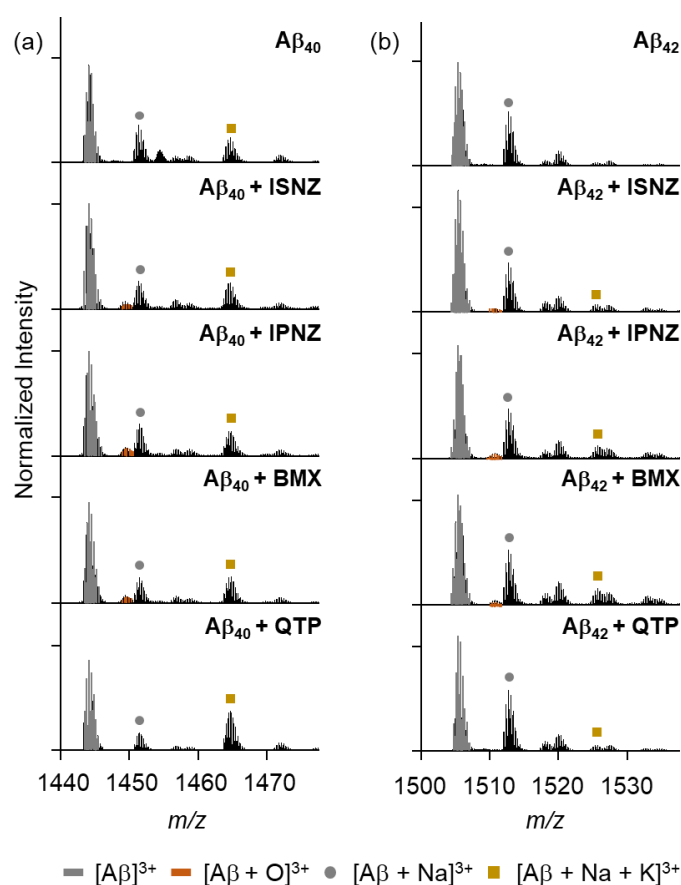
Figure 4.6. Interactions between the repositioning candidates and metal-free $A\beta$ detected by ESI–MS. Spectra of the samples of (a) metal-free $A\beta_{40}$ and (b) metal-free $A\beta_{42}$ upon incubation with the compounds. Conditions: $[A\beta] = 100$ μM; [compound] = 200 μM; 20 mM ammonium acetate, pH 7.4; 37 C; 3 h incubation; no agitation; the incubated samples were then diluted by ten-fold with ddH$_2$O and injected into the mass spectrometer.

4.2.5. Free radical scavenging capacity and Inhibitory activity against AChE

The Trolox equivalent antioxidant (TEAC) assay was utilized to evaluate the free radical scavenging capacity of the compounds, relative to Trolox, a vitamin E analog.[42] As shown in Table 4.1, The TEAC values of **ISNZ**, **IPNZ**, and **BMX** were determined to be 0.89 ± 0.06, 0.98 ± 0.10, and 0.82 ± 0.083,

respectively, which suggests that these three compounds are capable of scavenging free radicals at a magnitude comparable to Trolox. Moveover, the inhibitory capacity of the repurposing candidates against AChE was determined using a fluorometric AChE activity assay. As a reference, tacrine, a potent AChE inhibitor,[43] was first tested and its inhibitory activity against AChE was determined under our conditions (IC_{50} = 24.9 ± 2.0 nM). Thereafter, the AChE inhibitory activities of the repurposing candidates were determined under the same conditions (Table 4.1). The IC_{50} values of **ISNZ**, **IPNZ**, and **BMX** against AChE were calculated to be 56.1 ± 15.1, 1710 ± 934, and 141 ± 25.2 μM, respectively. In contrast, **QTP** did not exhibit notable inhibitory activity against free organic radicals and AChE under our experimental conditions.

Table 4.1. Inhibitory activity against free organic radicals and AChE determined *via* TEAC and fluorometric assays, respectively.

	Tacrine	ISNZ	IPNZ	BMX	QTP
TEAC Value	n/a[a]	0.89 ± 0.055	0.98 ± 0.10	0.82 ± 0.083	n.d.[b]
AChE IC_{50} (μM)	0.0249 ± 0.002	56.1 ± 15.1	1710 ± 934	141 ± 25.2	n.d.[b]

[a]n/a, not applicable. [b]n.d., not determined. The inhibitory activity of **QTP** against free organic radicals and AChE was not significant enough to be detected under our experimental conditions.

4.3. Conclusions

Three pre-approved pharmaceutical compounds (*i.e.*, **ISNZ**, **IPNZ**, and **BMX**) were identified as multifunctional molecules exhibiting modulative reactivity towards Cu(II)–$A\beta_{40}$/$A\beta_{42}$, free organic radicals, and AChE. These molecules indicated an unexpected specificity against the aggregation pathways of Cu(II)–$A\beta_{40}$/$A\beta_{42}$. Mechanistic studies demonstrated that the oxidation of $A\beta$ induced by the compounds in the presence of Cu(II) could be responsible for such modulative reactivity. It is worth noting that these compounds did not demonstrate the ability to modify the aggregation of metal-free $A\beta$ under our experimental conditions, in contrast from a previous report.[29] Such distinction could be a result of the intricacies of our experimental subject in association with differences in experimental conditions and peptide samples. Moreover, **ISNZ**, **IPNZ**, and **BMX** displayed notable antioxidant properties comparable to that of Trolox. The modest AChE inhibitory activities of these repurposing candidates were observed with the IC_{50} values in the micromolar range. Our multidisciplinary studies indicate the potential utility of the benzohydrazide functionality as a multifunctional structural feature against multiple pathological factors found in the brain of AD. Although the modulative reactivity towards only three AD pathogenic elements were shown in this study, we believe that further studies could reveal additional utility of benzohydrazide. The multifunctional molecules discovered in this study could serve as investigative chemical tools and potential therapeutics that can simultaneously treat

depression in AD. More specifically, the specific modulative reactivity of **ISNZ**, **IPNZ**, and **BMX** towards Cu(II)–Aβ$_{40}$/Aβ$_{42}$ could prove useful in clinically investigating the pathological contribution of Cu(II)–Aβ$_{40}$/Aβ$_{42}$ towards neurodegeneration associated with AD. Such findings could facilitate the development of multifunctional molecules as therapeutics capable of stopping the progression of AD.

4.4. Experimental section

4.4.1. Materials and methods

All reagents were purchased from commercial suppliers and used as received unless noted otherwise. NMR and high-resolution mass spectrometric analyses of small molecules were conducted on an Agilent 400-MR DD2 NMR spectrometer (KAIST Department of Chemistry, Daejeon, Republic of Korea) and Accurate-Mass Q-TOF LC/MS (Agilent Technologies, Santa Clara, CA, USA), respectively. Absorbance and fluorescence values for biological assays were measured on a Molecular Devices SpectraMax M5e microplate reader (Sunnyvale, CA, USA). Trace metal contamination was removed from buffers and solutions used in metal binding and Aβ experiments by treating with Chelex overnight (Sigma-Aldrich, St. Louis, MO, USA). Optical spectra were recorded on an Agilent 8453 UV−Vis spectrometer. Aβ$_{40}$ and Aβ$_{42}$ (Aβ$_{42}$ = DAEFRHDSGYEVHHQKLVFFAEDV-GSNKGAIIGLMVGGVVIA) were purchased from Peptide Institute (Osaka, Japan). Acetylcholinesterase assay kit was purchased from Abcam (Cambridge, UK). Double-distilled H$_2$O (ddH$_2$O) was obtained from a Milli-Q Direct 16 system (18.2 MΩ·cm; Merck KGaA, Darmstadt, Germany). TEM images were taken using a Tecnai F30 (FEI) transmission electron microscope (KAIST Analysis Center for Research Advancement, Daejeon, Republic of Korea).

4.4.2. Synthesis of benmoxin (BMX) [*N'*-(1-phenylethyl)benzohydrazide].
Acetic acid (99%; 0.5 mL) was added to a CH$_3$OH solution (5 mL) containing acetophenone (226 g, 1.9 mmol) and benzohydrazide (256 mg, 1.9 mmol) at 0 °C. The mixture was then allowed to reach room temperature and stirred for 1 h. α-picoline borate (201 mg, 1.9 mmol) was then added to the reaction mixture and stirred for 5 min. The solution was then cooled to 0 °C and a 3 M solution of aqueous HCl (2.5 mL) was added. The resulting mixture was then allowed to reach room temperature and stirred for 30 min. The reaction was then quenched with an aqueous solution of 25% w/v Na$_2$CO$_3$ (10 mL). The products were extracted using EtOAc three times and the combined organic phase was washed with a saturated brine solution, dried with MgSO$_4$, and filtered. The filtrate was concentrated in vacuo. The crude product was then purified *via* silica gel column chromatography (hexanes–EtOAc, 10:1–1:20) to give our final product (52% yield).

4.4.3. Aβ aggregation experiments.
Aβ was dissolved in ammonium hydroxide [1% v/v NH$_4$OH (aq)]. The resulting solution was aliquoted, lyophilized overnight, and stored at −80 °C. A stock solution of

Aβ was then prepared by dissolving the lyophilized peptide using NH$_4$OH (aq) (10 μL, 1% v/v) and diluting with ddH$_2$O. All Aβ samples were prepared following previously reported procedures.[44-47] The concentration of the peptide solution was determined by measuring the absorbance of the solution at 280 nm (ε = 1,450 M^{-1}cm^{-1} for Aβ$_{40}$; ε = 1,490 M^{-1}cm^{-1} for Aβ$_{42}$). The buffered solution [20 mM 4-(2-hydroxyethyl)-1-piperazineethanesulfonic acid (HEPES), pH 6.6 for Cu(II)-treated samples or pH 7.4 for metal-free and Zn(II)-present conditions, 150 mM NaCl] was used for the preparation of Aβ samples. For the inhibition studies, compounds (final concentration, 50 μM; 1% v/v DMSO) were added to the samples of Aβ (25 μM) in the absence and presence of Cu(II) or Zn(II) (25 μM) followed by incubation for 24 h at 37 °C with constant agitation. For the disaggregation studies, Aβ (25 μM) was incubated with and without Cu(II) or Zn(II) (25 μM) for 24 h at 37 °C with constant agitation to generate preformed Aβ aggregates. The resulting Aβ aggregates were then treated with the compounds (50 μM) and incubated for an additional 24 h with constant agitation.

4.4.4. Gel/Western Blot. The resultant Aβ species from the inhibition and disaggregation experiments were analyzed through gel/Western blot using an anti-Aβ antibody (6E10).[44-47] The samples (10 μL) were separated on a 10−20% Tris-tricine gel (Invitrogen, Carlsbad, CA, USA). Following separation, the peptides were transferred onto nitrocellulose membranes and blocked with bovine serum albumin (BSA; 3% w/v; Sigma-Aldrich) in Tris-buffered saline (TBS) containing 0.1% v/v Tween-20 (Sigma-Aldrich) (TBS-T) for 4 h at room temperature or overnight at 4 °C. The membranes were incubated with 6E10 (1:2,000, Covance, Princeton, NJ, USA) in a solution of BSA (2% w/v in TBS-T) for 2 h at room temperature or overnight at 4 °C. After washing with TBS-T (three times, 10 min each), a horseradish peroxidase-conjugated goat anti-mouse secondary antibody (1:5,000 in 2% w/v BSA in TBS-T; Cayman Chemical Company, Ann Arbor, MI, USA) was added for 2 h at room temperature. Lastly, a homemade ECL kit[49] was used to visualize gel/Western blot data on a ChemiDoc MP Imaging System (Bio-Rad).

4.4.5. Cu(II) interaction studies. The interaction of the repurposing candidates with Cu(II) was monitored by UV–Vis spectroscopy. UV–Vis experiments were carried out in Chelex-treated buffered solution [20 mM HEPES, pH 6.6, 150 mM NaCl]. The solutions of compounds were titrated up to 5 equiv of CuCl$_2$ at room temperature. The mixture solution was allowed to equilibrate for 5 min after the addition of CuCl$_2$ at room temperature before the spectra were recorded.

4.4.6. ESI-MS measurements. Aβ (100 μM) was incubated with compounds (200 μM; 1% v/v DMSO) in 1 mM ammonium acetate, pH 7.4 at 37 °C with constant agitation. The incubated samples were diluted by 10-fold with ddH$_2$O and immediately prior to injection into the mass spectrometer. The

capillary voltage, nozzle voltage, and gas temperature were set to 5.8 kV, 2 kV, and 300 °C, respectively. More than 200 spectra were obtained for each sample and averaged for analysis.

4.4.7. TEAC assay. The free radical scavenging capacity of the selected compounds was determined by the TEAC assay based on the decolorization of ABTS [2,2'-azino-bis(3-ethylbenzothiazoline-6-sulfonic acid)diammonium salt] cation radical in comparison to that of the vitamin-E analog, Trolox, known for its antioxidant properties.[50] The TEAC assay was conducted in EtOH following previously reported methods.[40] Blue ABTS$^{+\bullet}$ cation radicals were generated by dissolving ABTS (7.0 mM) with potassium persulfate (2.5 mM) in ddH$_2$O (5 mL) water and incubating the solution for 16 h at room temperature in the dark. Then the solution was diluted with EtOH to an absorbance of *ca.* 0.7 at 734 nm. The ABTS$^{+\bullet}$ solution (200 μL) was then added to a clear 96 well plate and incubated for 5 min at 25 °C. Various concentrations compounds or Trolox were added to the 96 well plate and incubated at 25 °C for various time periods (1, 3, 6, and 10 min). Percent inhibition was calculated based on the measured absorbance at 734 nm [% inhibition = 100 X (A$_0$ − A)/A$_0$; A$_0$ = absorbance of control well without compound; A = absorbance of wells treated with compound] and plotted as a function of commpound concentration. The TEAC values of each time point was calculated as the ratios between the slope of the compounds and the slope of Trolox. All measurements were carried out in triplicate.

4.4.8. AChE activity assay. AChE inhibitory activities of the selected compounds were determined using a fluorometric AChE assay kit (Abcam, Cambridge, MA, USA) following the manufacturer's protocol with slight modifications. *ee*AChE was dissolved and diluted to a working solution of 400 mU/mL. 50 μL of the *ee*AChE solution was added to a 96 well plate. Varying concentrations of compounds in DMSO were then added to a 96 well plate. After shaking, the mixtures of *ee*AChE and flavonoids were pre-incubated for 5 min. A reaction mixture solution containing ACh, AChE probe, and AbRed^{TM} was added to the 96 well plate to initiate the reaction. Calculations of the AChE inhibition activity were made based on the fluorescence intensity ($\lambda_{ex}/\lambda_{em}$ = 540/590 nm) of the wells detected after 15 min of incubation. Data were normalized to the control (DMSO). All experiments were performed in duplicate.

4.5. Acknowledgments

4.6. References

1.   Savelieff, M. G.; Nam, G.; Kang, J.; Lee, H. J.; Lee, M.; Lim, M. H., Development of Multifunctional Molecules as Potential Therapeutic Candidates for Alzheimer's Disease,

Parkinson's Disease, and Amyotrophic Lateral Sclerosis in the Last Decade. *Chem. Rev.* **2019**, *119*, 1221-1322.

2. Hardy, J.; Higgins, G., Alzheimer's Disease: the Amyloid Cascade Hypothesis. *Science* **1992**, *256*, 184-185.

3. Selkoe, D. J., Early Network Dysfunction in Alzheimer's Disease. *Science* **2019**, *365*, 540-541.

4. Kepp, K. P., Bioinorganic Chemistry of Alzheimer's Disease. *Chem. Rev.* **2012**, *112*, 5193-5239.

5. Muhammad, T.; Ali, T.; Ikram, M.; Khan, A.; Alam, S. I.; Kim, M. O., Melatonin Rescue Oxidative Stress-Mediated Neuroinflammation/ Neurodegeneration and Memory Impairment in Scopolamine-Induced Amnesia Mice Model. *J. Neuroimmune Pharmacol.* **2019**, *14*, 278-294.

6. Naudí, A.; Cabré, R.; Dominguez-Gonzalez, M.; Ayala, V.; Jové, M.; Mota-Martorell, N.; Piñol-Ripoll, G.; Gil-Villar, M. P.; Rué, M.; Portero-Otín, M.; Ferrer, I.; Pamplona, R., Region-specific Vulnerability to Lipid Peroxidation and Evidence of Neuronal Mechanisms for Polyunsaturated Fatty Acid Biosynthesis in the Healthy Adult Human Central Nervous System. *Biochim. Biophys. Acta* **2017**, *1862*, 485-495.

7. Herrero-Mendez, A.; Almeida, A.; Fernández, E.; Maestre, C.; Moncada, S.; Bolaños, J. P., The Bioenergetic and Antioxidant Status of Neurons is Controlled by Continuous Degradation of a Key Glycolytic Enzyme by APC/C–Cdh1. *Nat. Cell Biol* **2009**, *11*, 747-752.

8. Stefanatos, R.; Sanz, A., The Role of Mitochondrial ROS in the Aging Brain. *FEBS Lett.* **2018**, *592*, 743-758.

9. Bartus, R. T.; Dean, R. L.; Beer, B.; Lippa, A. S., The Cholinergic Hypothesis of Geriatric Memory Dysfunction. *Science* **1982**, *217*, 408-414.

10. Nam, E.; Nam, G.; Lim, M. H., Synaptic Copper, Amyloid-β, and Neurotransmitters in Alzheimer's Disease. *Biochemistry* **2020**, *59*, 15-17.

11. Nam, G.; Lim, M. H., Intertwined Pathologies of Amyloid-β and Metal Ions in Alzheimer's Disease: Metal–Amyloid-β. *Chem, Lett.* **2019**, *48*, 951-960.

12. Kepp, K. P., Alzheimer's Disease: How Metal Ions Define β-amyloid Function. *Coord. Chem. Rev.* **2017**, *351*, 127-159.

13. Ashburn, T. T.; Thor, K. B., Drug Repositioning: Identifying and Developing New Uses for Existing Drugs. *Nat. Rev. Drug Discov.* **2004**, *3*, 673-683.

14. Rovner, B. W.; Broadhead, J.; Spencer, M.; Carson, K.; Folstein, M. F., Depression and Alzheimer's Disease. *Am. J. Psych.* **1989**, *146*, 350-353.

15. Lyketsos, C. G.; Olin, J., Depression in Alzheimer's Disease: Overview and Treatment. *Biol. Psych.* **2002**, *52*, 243-252.

16. Burke, A. D.; Goldfarb, D.; Bollam, P.; Khokher, S., Diagnosing and Treating Depression in Patients with Alzheimer's Disease. *Neurol. Ther.* **2019**, *8*, 325-350.

17. Lyketsos, C. G.; Steele, C.; Baker, L.; Galik, E.; Kopunek, S.; Steinberg, M.; Warren, A., Major and Minor Depression in Alzheimer's Disease: Prevalence and Impact. *J. Neuropsych. Clin. Neurosci.* **1997**, *9*, 556-561.

18. Payne, J. L.; Lyketsos C. G.; Steele, C.; Baker, L.; Galik, E.; Kopunek, S.; Steinberg, M.; Warren, A., Relationship of Cognitive and Functional Impairment to Depressive Features in Alzheimer's Disease and Other Dementias. *J. Neuropsych. Clin. Neurosci.* **1998**, *10*, 440-447.

19. Ownby, R. L.; Crocco, E.; Acevedo, A.; John, V.; Loewenstein, D., Depression and Risk for Alzheimer Disease: Systematic Review, Meta-analysis, and Metaregression Analysis. *Arch. Gen. Psychiatry* **2006**, *63*, 530-538.

20. Frisardi, V.; Panza, F.; Farooqui, A. A., Late-life Depression and Alzheimer's Disease: The Glutamatergic System Inside of this Mirror Relationship. *Brain Res. Rev.* **2011**, *67*, 344-355.

21. Caraci, F.; Copani, A.; Nicoletti, F.; Drago, F., Depression and Alzheimer's Disease: Neurobiological Links and Common Pharmacological Targets. *Eur. J. Pharmacol.* **2010**, *626*, 64-71.

22. Santos, L. E.; Beckman, D.; Ferreira, S. T., Microglial Dysfunction Connects Depression and Alzheimer's Disease. *Brain, Behav. Immun.* **2016**, *55*, 151-165.

23. Nau, R.; Sörgel, F.; Eiffert, H., Penetration of Drugs through the Blood-Cerebrospinal

Fluid/Blood-Brain Barrier for Treatment of Central Nervous System Infections. *Clin. Microbiol. Rev.* **2010**, *23*, 858-883.

24. Nair, V.; Lal, H.; Roth, L. J., A Demonstration of the Early Entry of Iproniazid into the Central Nervous System. *Int. J. Neuropharmacol.* **1962**, *1*, 361-364.

25. Carreño, F.; Paese, K.; Silva, C. M.; Guterres, S. S.; Dalla Costa, T., Pharmacokinetic Investigation of Quetiapine Transport across Blood–Brain Barrier Mediated by Lipid Core Nanocapsules Using Brain Microdialysis in Rats. *Mol. Pharm.* **2016**, *13*, 1289-1297.

26. Zheng, Y.; Chen, X.; Benet, L. Z., Reliability of In Vitro and In Vivo Methods for Predicting the Effect of P-Glycoprotein on the Delivery of Antidepressants to the Brain. *Clin. Pharmacokinet.* **2016**, *55*, 143-167.

27. Pletscher, A., The Discovery of Antidepressants: A Winding Path. *Experientia* **1991,** *47* (1), 4-8.

28. Ramachandraih, C. T.; Subramanyam, N.; Bar, K. J.; Baker, G.; Yeragani, V. K., Antidepressants: from MAOIs to SSRIs and more. *Indian J. Psychiatry* **2011**, *53*, 180.

29. Maheshwari, M.; Roberts, J. K.; DeSutter, B.; Duong, K. T.; Tingling, J.; Fawver, J. N.; Schall, H. E.; Kahle, M.; Murray, I. V. J., Hydralazine Modifies Aβ Fibril Formation and Prevents Modification by Lipids In Vitro. *Biochemistry* **2010**, *49*, 10371-10380.

30. Youdim, M. B.; Weinstock, M., Therapeutic Applications of Selective and Non-selective Inhibitors of Monoamine Oxidase A and B that do not Cause Significant Tyramine Potentiation. *Neurotoxicology* **2004**, *25*, 243-250.

31. Nelson, S. D.; Mitchell, J. R.; Snodgrass, W.; Timbrell, J. A., Hepatotoxicity and Metabolism of Iproniazid and Isopropylhydrazine. *J. Pharmacol. Exp. Ther.* **1978**, *206*, 574-585.

32. Palm, D.; Fengler, H. J.; Güllner, H. G.; Planz, G.; Quiring, K.; May, B.; Helmstaedt, D.; Lemmer, B.; Moon, H. K.; Holler, C., Quantitation of Irreversible Inhibition of Monoamine Oxidase in Man. *Eur. J. Clin. Pharmacol.* **1971**, *3*, 82-92.

33. Kasper, S.; Müller-Spahn, F., Review of Quetiapine and its Clinical Applications in Schizophrenia. *Exp. Opin. Pharmacother.* **2000**, *1*, 783-801.

34. Richelson, E.; Souder, T., Binding of Antipsychotic Drugs to Human Brain Receptors: Focus on Newer Generation Compounds. *Life Sci.* **2000**, *68*, 29-39.

35. Kawase, Y.; Yamagishi, T.; Kato, J.-y.; Kutsuma, T.; Kataoka, T.; Iwakuma, T.; Yokomatsu, T., Reductive Alkylation of Hydrazine Derivatives with α-Picoline-Borane and Its Applications to the Syntheses of Useful Compounds Related to Active Pharmaceutical Ingredients. *Synthesis* **2014**, *46*, 455-464.

36. Derrick, J. S.; Kerr, R. A.; Nam, Y.; Oh, S. B.; Lee, H. J.; Earnest, K. G.; Suh, N.; Peck, K. L.; Ozbil, M.; Korshavn, K. J.; Ramamoorthy, A.; Prabhakar, R.; Merino, E. J.; Shearer, J.; Lee, J. Y.; Ruotolo, B. T.; Lim, M. H., A Redox-Active, Compact Molecule for Cross-Linking Amyloidogenic Peptides into Nontoxic, Off-Pathway Aggregates: In Vitro and In Vivo Efficacy and Molecular Mechanisms. *J. Am. Chem. Soc.* **2015**, *137*, 14785-14797.

37. Derrick, J. S.; Lee, J.; Lee, S. J. C.; Kim, Y.; Nam, E.; Tak, H.; Kang, J.; Lee, M.; Kim, S. H.; Park, K., Mechanistic Insights into Tunable Metal-mediated Hydrolysis of Amyloid-β Peptides. *J. Am. Chem. Soc.* **2017**, *139*, 2234-2244.

38. Han, J.; Lee, H. J.; Kim, K. Y.; Lee, S. J. C.; Suh, J.-M.; Cho, J.; Chae, J.; Lim, M. H., Tuning Structures and Properties for Developing Novel Chemical Tools toward Distinct Pathogenic Elements in Alzheimer's Disease. *ACS Chem. Neurosci.* **2018**, *9*, 800-808.

39. Kang, J.; Lee, S. J. C.; Nam, J. S.; Lee, H. J.; Kang, M.-G.; Korshavn, K. J.; Kim, H.-T.; Cho, J.; Ramamoorthy, A.; Rhee, H.-W.; Kwon, T.-H.; Lim, M. H., An Iridium(III) Complex as a Photoactivatable Tool for Oxidation of Amyloidogenic Peptides with Subsequent Modulation of Peptide Aggregation. *Chem. Eur. J.* **2017**, *23*, 1645-1653.

40. Ji, Y.; Lee, H. J.; Kim, M.; Nam, G.; Lee, S. J. C.; Cho, J.; Park, C.-M.; Lim, M. H., Strategic Design of 2,2′-bipyridine Derivatives to Modulate Metal–amyloid-β Aggregation. *Inorg. Chem.* **2017**, *56*, 6695-6705.

41. Han, J.; Lee, H. J.; Kim, K. Y.; Nam, G.; Chae, J.; Lim, M. H., Mechanistic Approaches for Chemically Modifying the Coordination Sphere of Copper–amyloid-β Complexes. *Proc. Natl. Acad. Sci. U.S.A.* **2020**, *117*, 5160-5167.

42. Forrest, V. J.; Kang, Y.-H.; McClain, D. E.; Robinson, D. H.; Ramakrishnan, N., Oxidative stress-Induced Apoptosis Prevented by Trolox. *Free Radic. Biol. Med.* **1994**, *16*, 675-684.

43. Ahmed, M.; Rocha, J. B. T.; Corrêa, M.; Mazzanti, C. M.; Zanin, R. F.; Morsch, A. L. B.; Morsch, V. M.; Schetinger, M. R. C., Inhibition of Two Different Cholinesterases by Tacrine. *Chem. Biol. Interact.* **2006**, *162*, 165-171.

44. Lee, S.; Zheng, X.; Krishnamoorthy, J.; Savelieff, M. G.; Park, H. M.; Brender, J. R.; Kim, J. H.; Derrick, J. S.; Kochi, A.; Lee, H. J.; Kim, C.; Ramamoorthy, A.; Bowers, M. T.; Lim, M. H., Rational Design of a Structural Framework with Potential Use to Develop Chemical Reagents that Target and Modulate Multiple Facets of Alzheimer's Disease. *J. Am. Chem. Soc.* **2014**, *136*, 299-310.

45. Choi, J. S.; Braymer, J. J.; Nanga, R. P.; Ramamoorthy, A.; Lim, M. H., Design of Small Molecules that Target Metal-Aβ Species and Regulate Metal-induced Aβ Aggregation and Neurotoxicity. *Proc. Natl. Acad. Sci. U.S.A.* **2010**, *107*, 21990-21995.

46. Hindo, S. S.; Mancino, A. M.; Braymer, J. J.; Liu, Y.; Vivekanandan, S.; Ramamoorthy, A.; Lim, M. H., Small Molecule Modulators of Copper-induced Aβ Aggregation. *J. Am. Chem. Soc.* **2009**, *131*, 16663-16665.

47. Lee, H. J.; Korshavn, K. J.; Nam, Y.; Kang, J.; Paul, T. J.; Kerr, R. A.; Youn, I. S.; Ozbil, M.; Kim, K. S.; Ruotolo, B. T.; Prabhakar, R.; Ramamoorthy, A.; Lim, M. H., Structural and Mechanistic Insights into Development of Chemical Tools to Control Individual and Inter-Related Pathological Features in Alzheimer's Disease. *Chem. Eur. J.* **2017**, *23*, 2706-2715.

48. Beck, M. W.; Oh, S. B.; Kerr, R. A.; Lee, H. J.; Kim, S. H.; Kim, S.; Jang, M.; Ruotolo, B. T.; Lee, J. Y.; Lim, M. H., A Rationally Designed Small Molecule for Identifying an In Vivo Link between Metal-amyloid-β Complexes and the Pathogenesis of Alzheimer's Disease. *Chem. Sci.* **2015**, *6*, 1879-1886.

49. Mruk, D. D.; Cheng, C. Y., Enhanced Chemiluminescence (ECL) for Routine Immunoblotting: An Inexpensive Alternative to Commercially Available Kits. *Spermatogenesis* **2011**, *1*, 121-122.

50. Barclay, L. R. C.; Locke, S. J.; MacNeil, J. M.; VanKessel, J.; Burton, G. W.; Ingold, K. U., Autoxidation of Micelles and Model Membranes. Quantitative Kinetic Measurements can be Made by Using either Water-soluble or Lipid-soluble Initiators with Water-soluble or Lipid-soluble Chain-breaking Antioxidants. *J. Am. Chem. Soc.* **1984**, *106*, 2479-2481.

Dr. Juhye Kang, we really started working together on the flavonoid project, but I remember the trip we took to Jeonbuk University. We've had some good times. I hope we stay in touch and I want to thank you for all the help. I really think you played a big part in my ability to finish my Ph.D. Yonghwan Ji, starting with the flavonoid project, we've had some ups and downs, but we had some fun both in and out of the lab. I hope you're enjoying life and we'll catch the waves sometime. Eunju Nam, haven't spent a whole lot of time together, but I respect you for your dedication and work ethic. I hope you achieve your dreams and happiness in life. Jiyeon Han, we didn't get to hang out too much because we were both so busy, but I know you remember that one time we hung out in Ulsan. I hope your puppy stays healthy and you graduate soon! Mingeun Kim, stop worrying so much and learn to enjoy life sometimes. I know you'll work hard no matter what, but stop and smell the flowers. Let's hope Arsenal can bounce back soon! Jongmin Suh, apart from your scientific capabilities, I find your taste in music quite respectable. I look forward to seeing you make significant progress in cancer research in the future with your brains and willpower, I believe you can make some great strides. Gunhee Kim, I know you had a lot on your plate, while we were working on the repurposing project. Thank you for sticking it out. Yelim Yi, you work horse you. I'm still amazed by your ability to put your head down and work for hours on end. How do you do it? I do worry about you at times you know, but I think you might be wiser than I am in most aspects. I hope that I can instill some sense of the importance of balance. Mannkyu Hong, thanks for working through our collaboration projects. The computational studies seemed to add quite a bit of depth to our studies. I know getting adjusted to our lab was a bit of a challenge, but nothing you couldn't handle. I hope you achieve your goals after graduation, beers are on you then! Lab manager: Mi Sook Lim, thank you for your efforts in maintaining the lab. I know that we don't express our appreciation much, but we are grateful for your help.

Kimberly, for the last almost 6 years you have been by my side through thick and thin. I'm not quite sure how to express how grateful I am for you. You have been my light through my times of struggle without wavering. I really appreciate what you've done for me. I would not have made it this far without you. You moving to Sadang, Ulsan, then Daejeon just to stay with me despite your own plans. Deep down inside, I feel the gravity of such decisions at the same time I fail to acknowledge and express how much you have done for me. So here I am trying. You are by far the most wonderful human being I have been around. At times I am perplexed by how strong, considerate, and delicate you can be at the same time. I constantly strive for balance, but when it comes to one's character you truly demonstrate positive equilibrium. I respect you, I love you, and I look forward to our future together.

To my family, that has been dealing with a pretentious, complaining, selfish brother/son. Although we haven't spent a majority of the last 30 years together, nothing beats the familiarity of family, especially

when it comes to me being terrible. You guys have been with me from the beginning. We have some major differences and issues, but we can try to work on them so that we can connect better. I love you all.

To my friends that had to put up with my whining and complaining, thank you for sticking around and keeping me grounded. My friends in Daejeon (Jamal, Colt, Mike, Mik, John, Jenna), Ulsan (June, Patrick, Fanus, Mikey, Matt, Jenefer, Indi), Seoul (James, Jinwoo, Shinhee), and U.S. (Monica, Ann, Allen, Donbee, Sean, Katherine, Jacob, Tamir, Sam, Eric, Marc, Candice, Adam). Thank you for being there for me when I was down to talk me up and keep me going. I appreciate everything you guys have done for me. For those of you I haven't seen in a while, I miss you and look forward to spending time with you soon.

My collaborators [Professor Mu-Hyun Baik, Professor Young-Ho Lee, Dr. Yuxin Lin, Professor Jae-sung Bae, Professor Hee Kyung Jin], thank you all for your help. Thanks to your contributions towards our project, I was able to complete my Ph.D. program.

Geewoo Nam

Department of Chemistry
Ulsan National Institute of Science and Technology (UNIST)
UNIST-gil 50, Ulsan 44919, Republic of Korea.
Office Phone: +82-42-350-2866, Cell Phone: +82-10-4087-3902
Email: nameraser@unist.ac.kr

Education

Sep. 2016 – Present   **Ph.D. Candidate, Chemistry, Ulsan National Institute of Science and Technology (UNIST), Ulsan, Korea**
Thesis Title: Identification and Structural Analysis of Multifunctional Molecules with Modulative Reactivities against Pathogenic Elements of Alzheimer's Disease
Advisors: Professors Mi Hee Lim and Tae-Hyuk Kwon

Mar. 2014 – June 2016   **M.Sc., Fine Chemistry, Seoul National University of Science and Technology, Seoul, Korea**
Thesis Title: Investigating cell death mechanisms of photodynamic therapy against breast cancer cells utilizing liposomal delivery of porphyrin
Advisor: Professor Joon Myong Song

Mar. 2008 – May 2013   **B.S., Chemistry, Virginia Polytechnic Institute, Blacksburg, VA, USA**

Honors, Awards, and Scholarships

July 2019   Springer Nature Poster Award
The 15th International Symposium on Applied Bioinorganic Chemistry

Research Experience

Jan. 2010 – Feb.2011   Undergraduate Researcher
Virginia Polytechnic Institute, Blacksburg, VA, USA
Research Topic: Development of Supramolecular Ru(II)-Rh(III)-Ru(II) Complexes as Electron Reservoir Ligands for Hydrogen Evolution
Advisor: Professor Karen Brewer

Teaching Experience

Mar. 2019 – June 2019   Bioinorganic Chemistry, Teaching Assistant
Korea Advanced Institute of Science and Technology (KAIST), Korea

Mar. 2018 – June 2018   General Chemistry Laboratory, Teaching Assistant (Chief)

Ulsan National Institute of Science and Technology (UNIST), Korea

Mar. 2017 – June 2017	Inorganic Chemistry Laboratory, Teaching Assistant Ulsan National Institute of Science and Technology (UNIST), Korea
Sep. 2014 – Dec. 2014	Pharmaceutical Analysis Laboratory, Laboratory Teaching Assistant Seoul National University, Korea
Mar. 2014 – June 2014	Pharmaceutical Analysis Laboratory, Laboratory Teaching Assistant Seoul National University, Korea
Sep. 2013 – Dec. 2013	Pharmaceutical Analysis Laboratory, Laboratory Teaching Assistant Seoul National University, Korea

Publications

1. **Geewoo Nam**,[†] Mannkyu Hong,[†] Hyuck Jin Lee, Yonghwan Ji, Juri Lee, Juhye Kang, Mu-Hyun Baik*, and Mi Hee Lim* "Multiple Reactivities of Flavonoids towards Pathological Elements in Alzheimer's Disease: Structure-Activity Relationship" **2020**, *Submitted.* ([†]Co-first authorship).

2. **Geewoo Nam**,[†] Yuxin Lin,[†] Mi Hee Lim*, and Young-Ho Lee*, "Key Physicochemical and Biological Factors of the Phase Behavior of Tau" **2020**, *Submitted.* ([†]Co-first authorship).

3. **Geewoo Nam**,[†] Yelim Yi,[†] Hyuck Jin Lee, Juri Lee, Juhye Kang, and Mi Hee Lim*, "Chapter X: Metalloneurochemistry in Comprehensive Coordination Chemistry III (CCC III)" **2020**, *In Press*. ([†]Co-first authorship).

4. Mingeun Kim,[†] Juhye Kang,[†] Misun Lee,[†] Jiyeon Han, **Geewoo Nam**, Eunyoung Tak, Min Sun Kim, Doin Kim, Hyuck Jin Lee, Eunju Nam, Joo-Yong Lee, and Mi Hee Lim*, "Minimalistic Principles for Designing Small Molecules with Multiple Reactivities against Pathological Factors in Dementia" *J. Am. Chem. Soc.* **2020**, *142*, 8183. ([†]Co-first authorship).

5. Jiyeon Han, Hyuck Jin Lee, Kyu Yeon Kim, **Geewoo Nam**, Junghyun Chae, and Mi Hee Lim*, "Mechanistic Approaches for Chemically Modifying the Coordination Sphere of Copper–Amyloid-β Complexes" *Proc. Natl. Acad. Sci. U.S.A.* **2020**, *117*, 5160.

6. Eunju Nam, **Geewoo Nam**, and Mi Hee Lim*, "Synaptic Copper, Amyloid-β, and Neurotransmitters in Alzheimer's Disease" *Biochemistry* **2020**, *59*, 15.

7. Min Hee Park, Misun Lee, **Geewoo Nam**, Mingeun Kim, Juhye Kang, Byung Jo Choi, Min Seock Jeong, Kang Ho Park, Wan Hui Hana, Eunyoung Tak, Min Sun Kim, Juri Lee, Yuxi Lin, Young-Ho Lee, Im-Sook Song, Min-Koo Choi, Joo-Yong Lee, Hee Kyung Jin, Jae-sung Bae*, and Mi Hee Lim*, "N,N′-Diacetyl-p-phenylenediamine Restores Microglial Phagocytosis and Improves Cognitive Defects in Alzheimer's Disease Transgenic Mice" *Proc. Natl. Acad. Sci. U.S.A.* **2019**, *116*, 23426.

8. Juhye Kang,[†] Jung Seung Nam,[†] Hyuck Jin Lee, **Geewoo Nam**, Hyun-Woo Rhee, Tae-Hyuk Kwon, and Mi Hee Lim*, "Chemical Strategies to Modify Amyloidogenic Peptides by Iridium(III) Complexes: Coordination and Photo-induced Oxidation" *Chem. Sci.* **2019**, *10*, 6855. ([†]Co-first authorship).

9. **Geewoo Nam** and Mi Hee Lim*, "Intertwined Pathologies of Amyloid-β and Metal Ions in Alzheimer's Disease: Metal–Amyloid-β" *Chem. Lett.* **2019**, *48*, 951.

10. Masha G. Savelieff,[†] **Geewoo Nam**,[†] Juhye Kang,[†] Hyuck Jin Lee, Misun Lee, and Mi Hee Lim*. "Development of Multifunctional Molecules as Potential Therapeutic Candidates for Alzheimer's Disease, Parkinson's Disease, and Amyotrophic Lateral Sclerosis in the Last Decade" *Chem. Rev.* **2019**, *119*, 1221. ([†]Co-first authorship).

11. **Geewoo Nam**,[†] Yonghwan Ji,[†] Hyuck Jin Lee,[†] Juhye Kang, Yelim Yi, Mingeun Kim, and Mi Hee Lim*. "Orobol: An Isoflavone with Regulatory Multifunctionality against Four Pathological Factors of Alzheimer's Disease" *ACS Chem. Neurosci.* **2019**, *10*, 3386. ([†]Co-first authorship).

12. Yonghwan Ji, Hyuck Jin Lee, Minjeong Kim, **Geewoo Nam**, Shin Jung Lee, Jaeheung Cho, Cheol-Min Park*, and Mi Hee Lim* "Strategic Design of 2,2'-Bipyridine Derivatives to Modulate Metal-Amyloid-β Aggregation" *Inorg. Chem.* **2017**, *56*, 6695.

13. **Geewoo Nam**, Sabarinathan Rangasamy, Hee Ju, Annie Agnes Suganya Samson, and Joon Myong Song* "Cell Death Mechanistic Study of Photodynamic Therapy Against Breast Cancer Cells Utilizing Liposomal Delivery of 5,10,15,20-tetrakis(benzo[b]thiophene) porphyrin" *J. Photochem. Photobiol.* **2017**, *166*, 116.

14. **Geewoo Nam**, Baskaran Purushothaman, Sabarinathan Rangasamy, and Joon Myong Song* "Investigating the Versatility of Multifunctional Silver Nanoparticles: Preparation and Inspection of their Potential as Wound Treatment Agents" *Int. Nano. Lett.* **2016**, *6*, 51.

15. **Geewoo Nam**, Sabarinathan Rangasamy, Baskaran Purushothaman, and Joon Myong Song* "The Application of Bactericidal Silver Nanoparticles in Wound Treatment" *Nanomater. Nanotechno.* **2016**, *5*, 23.

16. Gerald F. Manbeck, Theodore Canterbury, Rongwei Zhou, Skye King, **Geewoo Nam**, and Karen Brewer* "Electrocatalytic H_2 Evolution by Supramolecular Ru^{II}-Rh^{III}-Ru^{II} Complexes: Importance of Ligands as Electron Reservoirs and Speciation upon Reduction" *Inorg. Chem.* **2015**, *54*, 8148.

Presentations

1. **Geewoo Nam**, Yonghwan Ji, Hyuck Jin Lee, Juhye Kang, Yelim Yi, Mingeun Kim, Yuxi Lin, Young-Ho Lee, and Mi Hee Lim, Poster Presentation. "Orobol: An Isoflavone Exhibiting Regulatory Multifunctionality against Four Pathological Features of Alzheimer's Disease" *Korea Dementia Association Fall Symposium*, **2019**.

2. **Geewoo Nam**, Yonghwan Ji, Hyuck Jin Lee, Juhye Kang, Yelim Yi, Mingeun Kim, Yuxi Lin, Young-Ho Lee, and Mi Hee Lim, Poster Presentation. "Orobol: An Isoflavone Exhibiting Regulatory Multifunctionality against Four Pathological Features of Alzheimer's Disease" *The International Conference on Bioinspired Small Molecule Activation*, **2019**.

3. **Geewoo Nam**, Yonghwan Ji, Hyuck Jin Lee, Juhye Kang, Yelim Yi, Mingeun Kim, Yuxi Lin, Young-Ho Lee, and Mi Hee Lim, <u>Poster Presentation.</u> "Orobol: An Isoflavone Exhibiting Regulatory Multifunctionality against Four Pathological Features of Alzheimer's Disease" *15th International Symposium on Applied Bioinorganic Chemistry*, **2019**.
   <u>*Awarded as a "Springer Nature Poster Award".</u>

4. **Geewoo Nam** and Joon Myong Song. <u>Poster Presentation.</u> "Cytotoxicity mechanism of non-viral carriers polyethylenimine and poly-L-lysine using real time high-content cellular assay" *China-Japan-Korea Symposium on Analytical Chemistry*, **2015**.

5. **Geewoo Nam** and Joon Myong Song. <u>Poster Presentation.</u> "Quantum dot-based hypermulticolor high-content screening of herbal medicines for the monitoring of hair growth promotion and loss inhibition" *KOFAS 2014 & Convention of The Korean Society of Analytical Sciences*, **2014**.

6. **Geewoo Nam** and Joon Myong Song. <u>Poster Presentation.</u> "Visible-to-Near IR Quantum Dot-Based Hypermulticolor High-Content Screening of Herbal Medicines for the Efficacy Monitoring of Hair Growth Promotion and Hair Loss Inhibition" *Proceedings of the Spring International Convention of The Pharmaceutical Society of Korea*, **2014**.